Combining DFT and many-body methods to understand correlated materials

2008 J. Phys.: Condens. Matter 20 293201

(http://iopscience.iop.org/0953-8984/20/29/293201)

IOP PUBLISHING JOURNAL OF PHYSICS: CONDENSED MATTER

J. Phys.: Condens. Matter **20** (2008) 293201 (33pp) doi:10.1088/0953-8984/20/29/293201

TOPICAL REVIEW

Combining DFT and many-body methods to understand correlated materials

I V Solovyev

Computational Materials Science Center, National Institute for Materials Science,
1-2-1 Sengen, Tsukuba, Ibaraki 305-0047, Japan

E-mail: solovyev.igor@nims.go.jp

Received 4 January 2008, in final form 18 April 2008
Published 26 June 2008
Online at stacks.iop.org/JPhysCM/20/293201

Abstract

The electronic and magnetic properties of many strongly correlated systems are controlled by a limited number of states, located near the Fermi level and well isolated from the rest of the spectrum. This opens a formal way for combining the methods of first-principles electronic structure calculations, based on the density-functional theory (DFT), with many-body models, formulated in the restricted Hilbert space of states close to the Fermi level. The core of this project is the so-called 'realistic modeling' or the construction of the many-body model Hamiltonian entirely from first principles. Such a construction should be able to go beyond the conventional local-density approximation (LDA), which typically supplements the density-functional theory, and incorporate the physics of Coulomb correlations. It should also provide a transparent physical picture for the low-energy properties of strongly correlated materials. In this review article, we will outline the basic ideas of such a realistic modeling, which consists of the following steps: (i) the construction of the complete Wannier basis set for the low-energy LDA band; (ii) the construction of the one-electron part of the model Hamiltonian in this Wannier basis; (iii) the calculation of the screened Coulomb interactions for the low-energy bands by means of the constrained DFT. The most difficult part of this project is the evaluation of the screening caused by outer bands, which may have the same (e.g., the transition-metal 3d) character as the low-energy bands. The latter part can be efficiently done by combining the constrained DFT with the random-phase approximation (RPA) for the screened Coulomb interaction. The entire procedure will be illustrated on a series of examples, including the distorted transition-metal perovskite oxides, compounds with the inversion-symmetry breaking caused by the defects, and the alkali hyperoxide KO_2, which can be regarded as an analog of strongly correlated systems where the localized electrons reside on the *molecular orbitals* of the O_2^- dimer. In order to illustrate the abilities of the realistic modeling, we will also consider solutions of the low-energy models obtained for a number of systems, and argue that it can be used as a powerful tool for the exploration and understanding of the properties of strongly correlated materials.

(Some figures in this article are in colour only in the electronic version)

Contents

1. Introduction

Many of the successes of modern condensed-matter physics and chemistry are connected with the development of the density-functional theory (DFT), which is designed for the exploration of the ground-state properties of various substances and based on the minimization of the total energy functional $E[\rho]$ with respect to the electron density ρ [1–3]. For practical applications, DFT resorts to an iterative solution of the one-electron Kohn–Sham equations

$$\left(-\frac{\hbar^2}{2m}\nabla^2 + V\right)\psi_i = \varepsilon_i\psi_i, \tag{1}$$

together with the equation for the electron density

$$\rho = \sum_i f_i|\psi_i|^2, \tag{2}$$

defined in terms of eigenfunctions (ψ_i), eigenvalues (ε_i), and occupation numbers (f_i) of the Kohn–Sham quasiparticles. The potential V can be divided into the Coulomb ($V_{\rm H}$), exchange–correlation ($V_{\rm XC}$), and the external parts ($V_{\rm ext}$), which are the functional derivatives of corresponding contributions to the total energy with respect to the electron density. Formally speaking, this procedure is fully *ab initio* and free of any adjustable parameters.

However, the form of the exchange–correlation potential is generally unknown. For practical purposes, it is typically treated in the local-density approximation (LDA), which employs an analytical expression borrowed from the theory of an homogeneous electron gas in which the density of the electron gas is replaced by the local density of the real system. LDA is far from being perfect and there are many examples of so-called strongly correlated materials where the conventional LDA fails in describing the excited as well as the ground-state properties [4].

In strongly correlated materials, the state of each electron strongly depends on the state of the other electrons of the system, which are coupled (or correlate with each other) via the Coulomb interaction. Thus, this is a real many-body problem, and the situation is very different from the behavior of a homogeneous electron gas. The canonical example of strongly correlated materials is the transition-metal oxides [4]. A typical example of the electronic structure of the transition-metal oxides in the local-density approximation is shown in figure 1 for a series of distorted perovskite compounds[1]. We would like to emphasize two points.

(i) The common feature of many strongly correlated systems is the existence of a limited group of states, located near the Fermi level and well isolated from the rest of the spectrum. In the following, these states will be called the 'low-energy states' or the 'low-energy bands' or, simply, the L-bands. In the case of the perovskite oxides depicted in figure 1 these are the narrow transition-metal t_{2g} bands. From this point of view, the theoretical description of strongly correlated systems is feasible, and this is certainly a good sign. For example, if we are interested in electronic or magnetic properties, that are mainly controlled by the states close to the Fermi level, we can concentrate on the behavior of this group of states and use some simplified description for other parts of the electronic structure. Since the number of such states is limited, the problem can be solved, at least numerically.

(ii) Unfortunately, however, in order to solve this problem we should inevitably go beyond the local-density approximation, which greatly oversimplifies the physics of Coulomb correlations. For example, the systems depicted in figure 1 are metals within LDA, while in practice all of them are Mott insulators [4].

The insulating behavior is frequently associated with the excited state properties, which are not supposed to be reproduced by the Kohn–Sham equations designed for the ground state. However, the problem is much more serious. Suppose that we are interested in the behavior of inter-atomic magnetic interactions, which are ground-state properties. For narrow-band compounds, the main contributions to the magnetic interactions can be typically identified as the double exchange and superexchange [6, 7]. Double exchange operates in metallic systems. It is always ferromagnetic and proportional to the kinetic-energy gain, t, caused by free electron hopping between neighboring sites of the lattice [8]. Superexchange dominates in insulating compounds, where double exchange vanishes [9]. Superexchange can be either antiferromagnetic or ferromagnetic, depending on the number of electrons and the orbital state of the system [10]. It is proportional to t^2 and inversely proportional to the parameter of the on-site Coulomb interaction $\mathcal{U}$ [11]. Now, suppose that because of the limitations of LDA, our system is metallic rather than insulating. Then, the ferromagnetic double exchange will

[1] The properties of the distorted perovskite oxides will be discussed in details in section 6.3.

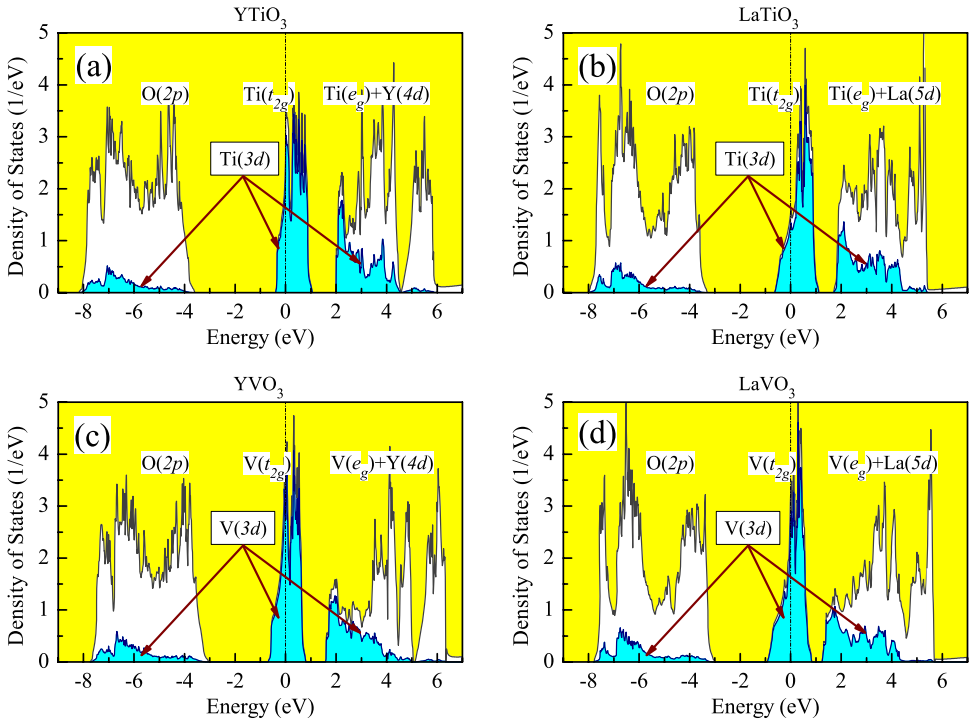

Figure 1. Total and partial densities of states of $YTiO_3$ (a), $LaTiO_3$ (b), YVO_3 ((c), orthorhombic phase), and $LaVO_3$ (d) in the local-density approximation [5]. The shaded area shows the contributions of transition-metal 3d states. Other symbols show the positions of the main bands. The Fermi level is at zero energy.

clearly dominate and we may have a totally wrong answer for the inter-atomic magnetic interactions as well as for the magnetic ground state. Therefore, if the system is insulating, an energy gap should already be present in the spectrum of Kohn–Sham eigenvalues. If it is not, the approximations underlying these Kohn–Sham equations must be corrected.

Because of these difficulties, for a long time strongly correlated compounds have been the almost exclusive prerogative of model condensed-matter physics, which has accumulated a great knowledge about the treatment and solution of this many-body problem, but only for model systems, described in terms of a limited number of model parameters. Model analysis has indeed provided useful and insightful information about many properties of strongly correlated systems. However, as the complexity of such systems rose, it inevitably presented a question about the correct choice of the model parameters, and in a number of cases—of the model itself. For example, the typical questions are how to incorporate the information about the chemical signature of elements composing the lattice into the model or how to treat lattice distortions? These questions gave rise to a new direction, which can be called 'realistic modeling'. The basic idea of realistic modeling is to construct the model Hamiltonian entirely from the first principles and make it free of any adjustable parameters, and then to solve this model Hamiltonian by using modern many-body methods. This was the main motivation in the area of model condensed-matter physics.

So, why do we need realistic modeling in the area of computational physics dealing with first-principles electronic structure calculations?

(i) Needless to say, the solution of the many-body problem for many realistic systems is a tremendous computational task. Therefore, one would always like to formulate it rigorously only in a *restricted* Hilbert space, which would pick up only those states that are primarily responsible for the physics of either of the considered phenomena, and include the effect of other states in the renormalization of the model parameters in the primary Hilbert space.

(ii) It is true that the methods of first-principles electronic structure calculations are currently on the rise. Standard computations within the density-functional theory have become routine and are frequently regarded as a useful tool for the numerical modeling or numerical experiments in materials science. However, we will always need some additional tools for the analysis and interpretation of the obtained data. Our final goal is not to obtain or reproduce the experimental trend for some complex compounds. Our goal is to provide some transparent physical interpretation for this trend on the microscopic level and come up with some useful suggestions about how this trend can be further improved. In this sense, realistic modeling will continue to play an important role as a tool for the analysis and interpretation of data obtained in standard electronic structure calculations.

Why should realistic modeling work? It is not an idle question, because eventually we would like to start with the electronic structure in the local-density approximation, construct the model by relying on this electronic structure, and apply this model for strongly correlated systems. In the other words, we start with something that was claimed to

be wrong for strongly correlated systems and try to refine it whilst staying within this disputable picture and relying on these disputable approximations. Nevertheless, there are several reasons to believe that such a construction is possible and propose a meaningful strategy for improving LDA whilst staying within LDA and, at the same time, bypassing its limitations and shortcomings.

(i) By its construction, the Kohn–Sham theory is a one-electron theory [2, 3]. Therefore, it should provide a good starting point for the one-electron part of the model, no matter whether it is supplemented with LDA or not. Moreover, all contributions to the Kohn–Sham Hamiltonian coming from the exchange and correlations are *local* in the local-density approximation. Therefore, they can be easily subtracted in the process of constructing the model Hamiltonian in order to avoid the double-counting problem.

(ii) The Coulomb correlations are certainly a weak point of LDA. However, LDA is an approximation in the density-functional theory, which is formulated for the ground state. Hence, it should be able to provide a good estimate for the total energy of the system [1–3]. Then, there is still a chance to derive the effective Coulomb interactions from the total energy difference (or any other quantity uniquely related to the total energy) by applying certain constraint conditions, which would simulate the redistribution of certain order parameters (typically, the electron density of the system).

The goal of this review article is to outline the main ideas, principles, and methods of realistic modeling as well as to illustrate abilities and perspectives of this direction for the solution of several practical questions related to the understanding of the real physical properties of transition-metal oxides and other strongly correlated systems. After specifying the model in section 2, in the next two sections we will discuss how the parameters of this model can be derived from the first-principles electronic structure calculations. Section 3 will be devoted to the construction of the one-electron Hamiltonian starting from the LDA band structure, while section 4 will deal with the problems of screening and the calculation of the effective Coulomb interaction. We will try not only to illustrate the method, but also to present a clear physical picture for the underlying ideas and approximation. Then, section 5 will briefly summarize the methods of solution of the model Hamiltonian. In section 6 we will give practical examples and show applications for realistic materials. We will derive the parameters of the model Hamiltonian and discuss what these parameters mean for understanding the electronic and magnetic properties of the considered compounds. Section 7 will contain a brief summary and concluding remarks.

2. Model Hamiltonian

First of all, we would like to specify our model for the low-energy bands. We will be mainly dealing with the effective multi-orbital Hubbard model,

$$\hat{\mathcal{H}} = \sum_{\mathbf{R}\mathbf{R}'} \sum_{\alpha\beta} h^{\alpha\beta}_{\mathbf{R}\mathbf{R}'} \hat{c}^{\dagger}_{\mathbf{R}\alpha} \hat{c}_{\mathbf{R}'\beta} + \frac{1}{2} \sum_{\mathbf{R}} \sum_{\alpha\beta\gamma\delta} U_{\alpha\beta\gamma\delta} \hat{c}^{\dagger}_{\mathbf{R}\alpha} \hat{c}^{\dagger}_{\mathbf{R}\gamma} \hat{c}_{\mathbf{R}\beta} \hat{c}_{\mathbf{R}\delta}, \tag{3}$$

where $\hat{c}^{\dagger}_{\mathbf{R}\alpha}$ ($\hat{c}_{\mathbf{R}\alpha}$) creates (annihilates) an electron in the Wannier orbital $\tilde{W}^{\alpha}_{\mathbf{R}}$ of (typically, the transition-metal) center $\mathbf{R}$, and α is a joint index, incorporating all remaining (spin and orbital) degrees of freedom, unless it is specified otherwise. The one-electron Hamiltonian $\hat{h}_{\mathbf{R}\mathbf{R}'} = \|h^{\alpha\beta}_{\mathbf{R}\mathbf{R}'}\|$ usually includes the following contributions: the site-diagonal part ($\mathbf{R} = \mathbf{R}'$) describes the local level splitting, caused by the crystal field and/or the relativistic spin–orbit interaction, whereas the off-diagonal part ($\mathbf{R} \neq \mathbf{R}'$) stands for transfer integrals, describing the kinetic energy of electrons.

$$U_{\alpha\beta\gamma\delta} = \int \mathrm{d}\mathbf{r} \int \mathrm{d}\mathbf{r}'\, \tilde{W}^{\alpha\dagger}_{\mathbf{R}}(\mathbf{r}) \tilde{W}^{\beta}_{\mathbf{R}}(\mathbf{r}) v_{\mathrm{scr}}(\mathbf{r}, \mathbf{r}') \tilde{W}^{\gamma\dagger}_{\mathbf{R}}(\mathbf{r}') \tilde{W}^{\delta}_{\mathbf{R}}(\mathbf{r}')$$
$$\equiv \langle \tilde{W}^{\alpha}_{\mathbf{R}} \tilde{W}^{\gamma}_{\mathbf{R}} | v_{\mathrm{scr}} | \tilde{W}^{\beta}_{\mathbf{R}} \tilde{W}^{\delta}_{\mathbf{R}} \rangle$$

are the matrix elements of the *screened* Coulomb interaction $v_{\mathrm{scr}}(\mathbf{r}, \mathbf{r}')$, which are supposed to be diagonal with respect to the site indices $\{\mathbf{R}\}$. In principle, $U_{\alpha\beta\gamma\delta}$ can also depend on the site-index $\mathbf{R}$. Nevertheless, to simplify the notation, here and throughout this paper we drop the index $\mathbf{R}$ in the notation of the Coulomb matrix elements. The inter-site matrix elements of $U_{\alpha\beta\gamma\delta}$ are typically small in comparison with the on-site ones.

3. One-electron Hamiltonian and Wannier functions

The one-electron part of the model Hamiltonian (3) is typically identified with the Kohn–Sham Hamiltonian in the basis of Wannier functions representing the low-energy part of the spectrum [12]. Therefore, the concept and definition of the Wannier functions is one of the key parts of the methods, and we would like to start our discussion by making several general comments about the relationship between Wannier functions and localized atomic orbitals, which represent the basis of many computational schemes.

Let us assume that there is a certain set of localized orbitals $\{\tilde{\chi}^{\alpha}_{\mathbf{R}}\}$ centered at the atomic sites $\{\mathbf{R}\}$ and specified by the orbital indices $\{\alpha\}$.[2] The corresponding Kohn–Sham Hamiltonian in the basis of $\{\tilde{\chi}^{\alpha}_{\mathbf{R}}\}$ will be denoted as $\hat{H}$. The orbitals are orthonormalized and form a complete basis in the valence part of the spectrum, so that each eigenvector ψ_i of $\hat{H}$ can be expressed as a linear combination of $\{\tilde{\chi}^{\alpha}_{\mathbf{R}}\}$. Concrete examples of such bases are the orthonormalized atomic orbitals or the muffin-tin orbitals [13–15].

Since the Wannier functions $\{\tilde{W}^{\alpha}_{\mathbf{R}}\}$ are also defined as certain set of localized orbitals representing $\{\psi_i\}$ [12, 16], we immediately recognize that for the full Hamiltonian $\hat{H}$, $\{\tilde{\chi}^{\alpha}_{\mathbf{R}}\}$ can be regarded as one of the possible (and fully legitimate) choices for $\{\tilde{W}^{\alpha}_{\mathbf{R}}\}$. This is a natural result and an advantage of the basis of localized atomic orbitals. In the plane-wave basis, the localized Wannier functions can be constructed from

[2] In the following, a set of nonorthonormalized atomic-like orbitals will be denoted as $\{\chi^{\alpha}_{\mathbf{R}}\}$. The orthonormalized orbitals, constructed from $\{\chi^{\alpha}_{\mathbf{R}}\}$, are denoted as $\{\tilde{\chi}^{\alpha}_{\mathbf{R}}\}$. Generally, such an orthonormalization can be performed numerically.

the eigenstates of $\hat{H}$ in the valence part of the spectrum, for example, by minimizing the square of the position operator $\langle \mathbf{r}^2 \rangle$ [16]. However, we would like emphasize that this is nothing other than an elegant way of constructing the compact atomic-like orbitals from the extended plane waves, a step which becomes unnecessary if one works from the start in the atomic basis.

However, what we typically need in the process of construction of the model Hamiltonians is different. For example, the solution of the many-body problem is practically impossible in the Hilbert space of states $\{\tilde{\chi}^{\alpha}_{\mathbf{R}}\}$ of the full Hamiltonian $\hat{H}$. Instead, one would like to concentrate on the behavior of a small number of L-bands, typically located near the Fermi level, and construct the Wannier basis only for this group of bands, which would be also orthogonal to the rest of the eigenstates of $\hat{H}$. This causes an additional complication because the basis functions $\{\tilde{\chi}^{\alpha}_{\mathbf{R}}\}$, though they can be regarded as the Wannier functions for the full Hamiltonian $\hat{H}$, are no longer those for any subspace of $\hat{H}$.

At present, there are two methods, which are typically used to circumvent this problem and construct the Wannier functions for the subspace of $\hat{H}$: the projector-operator method [16–19] and the downfolding method [5, 20–22].

3.1. The projector-operator method

In the projector-operator method, each (nonorthonormalized) Wannier function is generated by projecting a trial basis function $|\tilde{\chi}^{t}_{\mathbf{R}}\rangle$, centered at the site $\mathbf{R}$, onto the L-bands:

$$|W^{t}_{\mathbf{R}}\rangle = \hat{P}|\tilde{\chi}^{t}_{\mathbf{R}}\rangle, \tag{4}$$

where

$$\hat{P} = \sum_{i\in L} |\psi_i\rangle\langle\psi_i| \tag{5}$$

is the projector operator onto the L-bands, ψ_i is the eigenstate of $\hat{H}$, and i is a joint index combining the band index and the position of the momentum $\mathbf{k}$ in the first Brillouin zone. The functions $\{W^{t}_{\mathbf{R}}\}$ can be numerically orthonormalized,

$$|\tilde{W}^{t}_{\mathbf{R}}\rangle = \sum_{\mathbf{R}'t'} |W^{t'}_{\mathbf{R}'}\rangle [\hat{\mathcal{S}}^{-1/2}]^{t't}_{\mathbf{R}'\mathbf{R}}, \tag{6}$$

where $\hat{\mathcal{S}} = \|\mathcal{S}^{t't}_{\mathbf{R}'\mathbf{R}}\|$ is the overlap matrix,

$$\mathcal{S}^{t't}_{\mathbf{R}'\mathbf{R}} = \langle W^{t'}_{\mathbf{R}'}|W^{t}_{\mathbf{R}}\rangle \equiv \langle \tilde{\chi}^{t'}_{\mathbf{R}'}|\hat{P}|\tilde{\chi}^{t}_{\mathbf{R}}\rangle. \tag{7}$$

Then, the one-electron part of the model Hamiltonian (3) is defined by the matrix elements of $\hat{H}$ in the basis of these orthonormalized Wannier orbitals:

$$h^{tt'}_{\mathbf{R}\mathbf{R}'} = \langle \tilde{W}^{t}_{\mathbf{R}}|\hat{H}|\tilde{W}^{t'}_{\mathbf{R}'}\rangle. \tag{8}$$

3.2. The downfolding method

The conventional downfolding method also implies that the atomic basis can be divided into two parts: $\{\tilde{\chi}_{\mathbf{R}}\} = \{\tilde{\chi}^{t}_{\mathbf{R}}\} \oplus \{\tilde{\chi}^{r}_{\mathbf{R}}\}$, so that the low-energy part of the spectrum is mainly represented by the $\{\tilde{\chi}^{t}_{\mathbf{R}}\}$-states, while $\{\tilde{\chi}^{r}_{\mathbf{R}}\}$ is the rest of the basis states, which mainly contribute to the higher-energy part. Then, each eigenstate of $\hat{H}$ can be identically presented as the sum $|\psi_i\rangle = |\psi^{t}_{i}\rangle + |\psi^{r}_{i}\rangle$, where $|\psi^{t}_{i}\rangle$ and $|\psi^{r}_{i}\rangle$ are expanded over the basis states of the 't' and 'r' types, respectively. In this case, the Schrödinger equation for $|\psi_i\rangle$ takes the following form:

$$(\hat{H}^{tt} - \omega)|\psi^{t}_{i}\rangle + \hat{H}^{tr}|\psi^{r}_{i}\rangle = 0 \tag{9}$$

$$\hat{H}^{rt}|\psi^{t}_{i}\rangle + (\hat{H}^{rr} - \omega)|\psi^{r}_{i}\rangle = 0, \tag{10}$$

where $\hat{H}^{t(r)t(r)}$ are the blocks of matrix elements of $\hat{H}$ in the basis of 't' ('r')-states. The effective ω-dependent Hamiltonian $\hat{H}_{\mathrm{eff}}$ is obtained by expressing $|\psi^{r}_{i}\rangle$ from (10),

$$|\psi^{r}_{i}\rangle = -(\hat{H}^{rr} - \omega)^{-1}\hat{H}^{rt}|\psi^{t}_{i}\rangle, \tag{11}$$

and substituting into (9). This yields

$$\hat{H}_{\mathrm{eff}}(\omega) = (\hat{H}^{tt} - \omega) - \hat{H}^{tr}(\hat{H}^{rr} - \omega)^{-1}\hat{H}^{rt}, \tag{12}$$

which formally acts only on $|\psi^{t}_{i}\rangle$. However, $|\psi^{t}_{i}\rangle$ is only a part of the eigenvector, which is not orthonormalized. Therefore, $\hat{H}_{\mathrm{eff}}(\omega)$ should additionally be transformed to an orthonormal representation:

$$\hat{h}(\omega) = \hat{S}^{-1/2}(\omega)\hat{H}_{\mathrm{eff}}(\omega)\hat{S}^{-1/2}(\omega) + \omega, \tag{13}$$

which is specified by the overlap matrix,

$$\hat{S}(\omega) = 1 + \hat{H}^{tr}(\hat{H}^{rr} - \omega)^{-2}\hat{H}^{rt}. \tag{14}$$

The latter is obtained after the substitution of (11) into the normalization condition: $\langle\psi^{t}_{i}|\psi^{t}_{i}\rangle + \langle\psi^{r}_{i}|\psi^{r}_{i}\rangle = 1$.

In the conventional downfolding method, $\hat{h}$ is typically evaluated at the center of gravity of the L-bands, ω_0. Although the downfolding method does not explicitly require the construction of the Wannier functions, they can be formally reconstructed from $\hat{h}(\omega_0)$ [22].

3.3. Downfolding as the projector-operator method

The conventional downfolding method is exact. However, this property is guaranteed by the ω-dependence of $\hat{h}$, which is hardly useful from the practical point of view. Formally, for each ψ_i, ω in (13) should coincide with the eigenvalue of $\hat{H}$ corresponding to this ψ_i. Moreover, $\hat{h}(\omega)$ retains excessive information about $\hat{H}$, so that the full spectrum of $\hat{H}$ can be formally derived from $\hat{h}(\omega)$. However, typically, we do not need such a redundant information and would like to use $\hat{h}$ only for a small group of electronic states located near the Fermi level, and do it in the most exact form.

For these purposes, the downfolding method can be reformulated as a projector-operator method and reduced to it [23]. The trick is to replace the original Hamiltonian $\hat{H}$ in the downfolding method by a modified Hamiltonian $\hat{H}'$, which has the same set of eigenvalues $\{\varepsilon_i\}$ and eigenfunctions $\{\psi_i\}$ in the region of the L-bands[3]. The rest of the eigenstates are not important for the construction of the one-electron part of the

[3] This procedure was already used in [5, 20–22]. However, the details have been explained only in [23].

model Hamiltonian and can be placed in the region of infinite energies. Hence, we define $\hat{H}'$ in the following form:

$$\hat{H}' = \sum_{i\in L} |\psi_i\rangle\varepsilon_i\langle\psi_i| + \epsilon\hat{P}_\perp \equiv \hat{P}\hat{H}\hat{P} + \epsilon\hat{P}_\perp, \qquad (15)$$

where $\hat{P}_\perp = \hat{1} - \hat{P}$ is the projector operator to the subspace orthogonal to the L-bands and $\epsilon \to \infty$. According to the choice of the basis functions $\{\tilde{\chi}^t_{\mathbf{R}}\}$ and $\{\tilde{\chi}^r_{\mathbf{R}}\}$ in the downfolding method, the latter mainly contribute to the high-energy part of the spectrum. Therefore, the overlap between ψ_i in the low-energy part and any of $\{\tilde{\chi}^r_{\mathbf{R}}\}$ should be small, so that all eigenvalues of $(\hat{H}')^{rr}$ are of the order of ϵ. Then, it is intuitively clear that in the limit $\epsilon \to \infty$, the ω-dependence in (11) will disappear and the method will be exact. This statement can be proven rigorously, and such a proof can be found in [23].

Thus, by introducing a modified Hamiltonian of the form (15), the downfolding method can be naturally reformulated as the projector-operator method. The advantage of this procedure is that it allows us to go directly to the construction of the one-electron Hamiltonian $\hat{h}$, and formally skip the step of constructing the Wannier functions.

Finally, we would like to note that (15) is nothing but a scissor-operator-like transformation of the original Hamiltonian $\hat{H}$ and this strategy is different from the order-N muffin-tin orbital method, which was also used for the construction of the Wannier functions and where the basic idea was to make some *approximations* for the ω-dependence of the downfolded Hamiltonian [24].

3.4. Choice of trial orbitals and localization of the Wannier functions

At the beginning of this section we have argued that the basis functions $\{\tilde{\chi}^\alpha_{\mathbf{R}}\}$ can be regarded as the Wannier functions of the full Hamiltonian $\hat{H}$. Now, let us assume that each basis function is localized around the central atomic site and satisfies certain criteria of the 'maximal localization', such that any linear combination of $\{\tilde{\chi}^\alpha_{\mathbf{R}}\}$ will be "less localized" in comparison with the basis function $\tilde{\chi}^\alpha_{\mathbf{R}}$ from the original basis set, or at least has the same degree of the localization, if we are dealing with a linear combination of orbitals centered at the same atomic site[4]. However, this is not necessarily true if one wants to construct the Wannier functions only for some part of the electronic structure, which is specified by the subspace L of the full Hamiltonian $\hat{H}$. Due to the additional condition of orthogonality to other bands, such a Wannier function will inevitably be a linear combination of $\{\tilde{\chi}^\alpha_{\mathbf{R}}\}$. Therefore, it will inevitably be less localized in comparison with the trial function $\tilde{\chi}^t_{\mathbf{R}}$.

Nevertheless, one can try to 'minimize' the deviation from the original formulation for the full Hamiltonian $\hat{H}$ and ask which single atomic orbital centered at the site $\mathbf{R}$ will be the best representation for the Wannier orbital. Therefore, we search a new set of trial functions in the form:

$$|\tilde{\phi}^t_{\mathbf{R}}\rangle = \sum_\alpha c^\alpha_{\mathbf{R}}|\tilde{\chi}^\alpha_{\mathbf{R}}\rangle, \qquad (16)$$

and find the coefficients $\{c^\alpha_{\mathbf{R}}\}$, which maximize the projection $\langle\tilde{\phi}^t_{\mathbf{R}}|W^t_{\mathbf{R}}[\tilde{\phi}^t_{\mathbf{R}}]\rangle$ of $\tilde{\phi}^t_{\mathbf{R}}$ onto the nonorthonormalized Wannier function constructed from $\tilde{\phi}^t_{\mathbf{R}}$ using the projector-operator technique, $|W^t_{\mathbf{R}}[\tilde{\phi}^t_{\mathbf{R}}]\rangle = \hat{P}|\tilde{\phi}^t_{\mathbf{R}}\rangle$. It will automatically guarantee that $\tilde{\phi}^t_{\mathbf{R}}$ is the best single-orbital representation for $W^t_{\mathbf{R}}$ in the projector-operator method among the trial orbitals of the form (16). By substituting $W^t_{\mathbf{R}}[\tilde{\phi}^t_{\mathbf{R}}]$ into the projection $\langle\tilde{\phi}^t_{\mathbf{R}}|W^t_{\mathbf{R}}[\tilde{\phi}^t_{\mathbf{R}}]\rangle$, problem is reduced to the maximization of

$$D = \max_{\{c^\alpha_{\mathbf{R}}\}}\left\{\langle\tilde{\phi}^t_{\mathbf{R}}|\hat{P}|\tilde{\phi}^t_{\mathbf{R}}\rangle - \lambda(\langle\tilde{\phi}^t_{\mathbf{R}}|\tilde{\phi}^t_{\mathbf{R}}\rangle - 1)\right\}$$

with respect to $\{c^\alpha_{\mathbf{R}}\}$, where the Lagrange multipliers $\{\lambda\}$ enforce the orthonormality condition for $\{\tilde{\phi}^t_{\mathbf{R}}\}$. Then, the maximization of D is equivalent to the diagonalization of $\hat{P}_{\mathbf{RR}} = \|\langle\tilde{\chi}^\alpha_{\mathbf{R}}|\hat{P}|\tilde{\chi}^{\alpha'}_{\mathbf{R}}\rangle\|$, which is nothing but the site-diagonal part of the density matrix constructed from the L-bands in the basis of atomic orbitals $\{\tilde{\chi}^\alpha_{\mathbf{R}}\}$. After the diagonalization, we should simply pick up n eigenstates $\{\tilde{\phi}^t_{\mathbf{R}}\}$, corresponding to maximal eigenvalues $\{\lambda\}$, where n is the number of Wannier functions centered at the atomic site $\mathbf{R}$.[5] These $\{\tilde{\phi}^t_{\mathbf{R}}\}$ will maximize D. This procedure was proposed in [20] without any proof. Later, some intuitive arguments were given in [22]. The rigorous proof was given in [23].

3.5. Other parameters of model Hamiltonian

Electronic structure calculations are typically supplemented by some additional approximations, like the atomic-sphere-approximation (ASA), where the LDA potential is spherically averaged inside certain atomic spheres [13]. If ASA is used in the process of construction of the model Hamiltonian, the parameters $\{h^{\alpha\beta}_{\mathbf{RR}'}\}$ will include all effects of the covalent mixing between atomic orbitals. However, there will be other effects, which are not accounted by $\{h^{\alpha\beta}_{\mathbf{RR}'}\}$. The most important one comes from the nonsphericity (n-s) of the Madelung potential for the electron–ion interactions, which contributes to the crystal-field splitting [25][6]. The proper correction to

[4] The precise criterion of the maximal localization is not really important at this stage, because this is merely a mathematical construction and depending on the considered physical property one can introduce different criteria for 'maximal localization'.

[5] This can be paraphrased in a different way [5]. Of course, any set of the Wannier functions should be able to reproduce the total density at the site $\mathbf{R}$. Each Wannier function consists of the central part (or 'head'), located at the site $\mathbf{R}$, and the tail, spreading over the other sites. By identifying $\{\tilde{\phi}^t_{\mathbf{R}}\}$ with eigenstates corresponding to the maximal eigenvalues of the density matrix $\{\lambda\}$, we guarantee that the main part of the density at the site $\mathbf{R}$ is described by the 'heads' of the Wannier functions. Then, the remaining part of the density, corresponding to other (small) $\{\lambda\}$, is described by the tails of the Wannier functions coming from other sites. This implies that the weights of these tails should be also small.

[6] In fact, the contribution of Coulomb interactions to the crystal-field splitting is a tricky issue. Despite the apparent simplicity of the problem, one should clearly distinguish different contributions and not include them twice, for example, in the one-electron and Coulomb interaction parts of the model Hamiltonian (3). In this sense, the use of full-potential techniques does not automatically guarantee the right answer. Note that the nonsphericity of *on-site* interactions is explicitly included in the second part of the model Hamiltonian (3). Therefore, in order not to include it twice, one should subtract the corresponding contributions of the one-electron part originating from the Coulomb and exchange–correlation potentials in LDA.

$\|h^{\alpha\beta}_{\mathbf{RR}'}\|$ can be computed in the Wannier basis as:

$$\Delta^{\mathrm{n-s}} h^{\alpha\beta}_{\mathbf{RR}} = \sum_{\mathbf{R}'\neq\mathbf{R}} \langle \tilde{W}^{\alpha}_{\mathbf{R}} | \frac{-Z^{*}_{\mathbf{R}'} e^2}{|\mathbf{R}+\mathbf{r}-\mathbf{R}'|} | \tilde{W}^{\beta}_{\mathbf{R}} \rangle, \qquad (17)$$

where $Z^{*}_{\mathbf{R}'}$ is the total charge associated with the site $\mathbf{R}'$ (namely, the nuclear charge minus the screening electronic charge encircled by the atomic sphere), and $\mathbf{r}$ is the position of electron in the sphere $\mathbf{R}$.

The main idea behind this treatment is based on a certain hierarchy of interactions in solids. It implies that the strongest interaction, which leads to the energetic separation of the L-band from other bands (figure 1), is due to covalent mixing. For example, in many transition-metal oxides this interaction is responsible for the famous splitting between transition-metal t_{2g} and e_g bands [26]. The nonsphericity of the Madelung potential is considerably weaker than this splitting. However, it can be comparable to covalent mixing in the narrow L-band. Therefore, the basic idea is to treat this nonsphericity as a pseudo-perturbation [13], and calculate the matrix elements of the Madelung potential in the basis of Wannier functions constructed for a spherically averaged ASA potential.

The same strategy can be applied to the spin–orbit (s–o) interaction, which yields the following correction to $\|h^{\alpha\beta}_{\mathbf{RR}}\|$:

$$\Delta^{\mathrm{s-o}} h^{\alpha\beta}_{\mathbf{RR}} = \langle \tilde{W}^{\alpha}_{\mathbf{R}} | \frac{\hbar}{4m^2c^2} (\nabla V \times \mathbf{p}) \cdot \boldsymbol{\sigma} | \tilde{W}^{\beta}_{\mathbf{R}} \rangle.$$

Here, V is the self-consistent LDA potential and $\boldsymbol{\sigma}$ is the vector of Pauli matrices.

4. Effective Coulomb interactions

Generally, the matrix elements of the effective Coulomb interaction in the L-band are defined as the energy cost for moving an electron from one Wannier orbital, say $\tilde{W}^{\beta}_{\mathbf{R}'}$, populated by $n_{\mathbf{R}'\beta}$ electrons, to another orbital, say $\tilde{W}^{\alpha}_{\mathbf{R}}$, which was initially populated by $n_{\mathbf{R}\alpha}$ electrons [27]:

$$U_{\alpha\alpha\beta\beta} = E\left[n_{\mathbf{R}\alpha}+1, n_{\mathbf{R}'\beta}-1\right] - E\left[n_{\mathbf{R}\alpha}, n_{\mathbf{R}'\beta}\right]. \qquad (18)$$

For $\mathbf{R} \neq \mathbf{R}'$, the above matrix elements define the on-site Coulomb interactions, which are screened by inter-site interactions. In principle, by considering different combinations of $\mathbf{R}$ and $\mathbf{R}'$, one can extract individual parameters of on-site and inter-site interactions [22]. However, in practice, the inter-site interactions are substantially smaller than the on-site ones, and can be neglected in many cases[7]. The total energy difference (18) corresponding to $\mathbf{R} = \mathbf{R}'$, but with different orbital indices α and β, define the nonspherical part of on-site interactions, which is responsible for Hund's rules. More generally, one can consider an unitary transformation of α and β at each site of the system to a new basis, and repeat the same arguments. In the original basis, this would correspond to the transfer of an electron from a linear combination of Wannier orbitals at the site $\mathbf{R}'$ to a linear combination of Wannier orbitals at the site $\mathbf{R}$. This procedure will define the full matrix of screened Coulomb interactions $\hat{U} = \|U_{\alpha\beta\gamma\delta}\|$.

4.1. Constrained density-functional theory

The dependence of the total energy $E[\{n_{\mathbf{R}\alpha}\}]$ on the individual occupation numbers $\{n_{\mathbf{R}\alpha}\}$ can be obtained by applying constrained density-functional theory [29–32]:

$$E\left[\{n_{\mathbf{R}\alpha}\}\right] = E[\rho] + \sum_{\mathbf{R}\alpha} V_{\mathbf{R}\alpha} \left(\langle \tilde{W}^{\alpha}_{\mathbf{R}} | \hat{\rho} | \tilde{W}^{\alpha}_{\mathbf{R}} \rangle - n_{\mathbf{R}\alpha} \right), \qquad (19)$$

where $\hat{\rho}(\mathbf{r},\mathbf{r}') = \sum_i f_i \psi^{\dagger}_i(\mathbf{r}) \psi_i(\mathbf{r}')$ is the density operator constructed from the Kohn–Sham orbitals, $\rho(\mathbf{r}) = \hat{\rho}(\mathbf{r},\mathbf{r})$ is the electron density, and $\{V_{\mathbf{R}\alpha}\}$ are the external potentials, which play the role of Lagrange multipliers and enforce the occupations of the Wannier orbitals to be equal to $\{n_{\mathbf{R}\alpha}\}$. As it was already pointed out in the Introduction, in spite of many limitations for strongly correlated systems, LDA is formulated as an approximation to the theory of the ground state. Therefore, there is always a hope that it will provide a good estimate for $U_{\alpha\alpha\beta\beta}$ as long as the latter is expressed in terms of the total energy difference (18) or any other quantity, which is uniquely related to this total energy difference.

The total energy difference (18) is typically replaced by the difference of Kohn–Sham eigenvalues $\{\varepsilon_{\mathbf{R}\alpha}\}$ calculated for an intermediate configuration, by using Slater's transition state arguments[8]:

$$U_{\alpha\alpha\beta\beta} \approx \varepsilon_{\mathbf{R}\alpha}[n_{\mathbf{R}\alpha}+\tfrac{1}{2}, n_{\mathbf{R}'\beta}-\tfrac{1}{2}] - \varepsilon_{\mathbf{R}\alpha}[n_{\mathbf{R}\alpha}-\tfrac{1}{2}, n_{\mathbf{R}'\beta}+\tfrac{1}{2}]. \qquad (20)$$

It implies the validity of Janak's theorem [33]

$$\varepsilon_{\mathbf{R}\alpha} = \partial E / n_{\mathbf{R}\alpha}. \qquad (21)$$

However, in order to use this theorem, $\{\tilde{W}^{\alpha}_{\mathbf{R}}\}$ must be the eigenvectors of Kohn–Sham equations (1). Otherwise, Janak's theorem is not applicable, and the eigenvalues $\{\varepsilon_{\mathbf{R}\alpha}\}$ are ill-defined[9]. Of course, this assumption does not work for the regular Wannier functions $\{\tilde{W}^{\alpha}_{\mathbf{R}}\}$ constructed for the LDA Hamiltonian $\hat{H}$.[10]

Nevertheless, there is a transparent and physical solution of this problem, which rehabilitates the use of Janak's theorem. Indeed, since the kinetic-energy term is explicitly included in the Hubbard model (3), it *should not* contribute to the total energy difference (18). Otherwise, it would be included twice,

[7] Yet, one exception are the parameters derived for the single-orbital model. In this case, the number of variables available for the localization of the Wannier functions is limited so that the latter can be rather extended in the real space [22]. Therefore, the *bare* inter-site Coulomb and exchange integrals, calculated in the basis of these Wannier functions, are no longer negligible [17, 28]. Nevertheless, at present it is not entirely clear to what extent these interactions in the L-band will be screened by other bands of the system.

[8] Here, we also use the reciprocity condition $\varepsilon_{\mathbf{R}'\beta}[n_{\mathbf{R}\alpha}+\frac{1}{2}, n_{\mathbf{R}'\beta}-\frac{1}{2}] = \varepsilon_{\mathbf{R}\alpha}[n_{\mathbf{R}\alpha}-\frac{1}{2}, n_{\mathbf{R}'\beta}+\frac{1}{2}]$ for two fluctuations around the uniform state with $n_{\mathbf{R}\alpha} = n_{\mathbf{R}'\beta}$.

[9] For example, by defining $\varepsilon_{\mathbf{R}\alpha}$ as the diagonal matrix element of the Kohn–Sham Hamiltonian $\hat{H}$ in the basis of Wannier functions, $\varepsilon_{\mathbf{R}\alpha} = \langle \tilde{W}^{\alpha}_{\mathbf{R}} | \hat{H} | \tilde{W}^{\alpha}_{\mathbf{R}} \rangle$, there is no guarantee that this $\varepsilon_{\mathbf{R}\alpha}$ is equal to $\partial E / n_{\mathbf{R}\alpha}$, and (20) is consistent with the more general definition (18).

[10] Note that if $\{\tilde{W}^{\alpha}_{\mathbf{R}}\}$ were the eigenvectors of $\hat{H}$, all transfer integrals, which are defined as off-diagonal matrix elements of $\hat{H}$ with respect to $\tilde{W}^{\alpha}_{\mathbf{R}}$ and $\tilde{W}^{\beta}_{\mathbf{R}'}$ would vanish (see section 3.1).

and we would face the problem of double counting [30, 31]. This can be done by artificially switching off all matrix elements of $\hat{H}$ between $\tilde{W}^{\alpha}_{\mathbf{R}}$ and $\tilde{W}^{\beta}_{\mathbf{R}'}$, which is equivalent to switching off the kinetic energy. Another solution is to modify the Wannier functions $\{\tilde{W}^{\alpha}_{\mathbf{R}}\} \to \{\bar{W}^{\alpha}_{\mathbf{R}}\}$ (apparently by considering other boundary conditions) in order to enforce the property $\langle \bar{W}^{\alpha}_{\mathbf{R}}|\hat{H}|\bar{W}^{\beta}_{\mathbf{R}'}\rangle = 0$ for the given LDA Hamiltonian $\hat{H}$ [22][11]. These $\{\bar{W}^{\alpha}_{\mathbf{R}}\}$ can be regarded as the eigenfunctions of $\hat{H}$, that justify the use of Janak's theorem.

Finally, in the first order of $\pm\frac{1}{2}$, (20) can be transformed to

$$U_{\alpha\alpha\beta\beta} = \mathrm{d}\varepsilon_{\mathbf{R}\alpha}/\mathrm{d}n_{\mathbf{R}\alpha}, \tag{22}$$

where the derivative is calculated under the condition that the total number of electrons is conserved: $n_{\mathbf{R}\alpha} + n_{\mathbf{R}'\beta} = \text{const}$.

It is important that in the process of solution of the Kohn–Sham equations, the Wannier orbitals (and all remaining electronic structures) are allowed to relax in order to adjust the change of the occupation numbers $\{n_{\mathbf{R}\alpha}\}$. This relaxation is an important channel of screening. As we shall see below, the values of the screened Coulomb interactions in the L-band are defined not only by the extension of the Wannier functions in the ground state, but mainly by the change of these functions during the reaction $(n_{\mathbf{R}\alpha}, n_{\mathbf{R}'\beta}) \rightleftharpoons (n_{\mathbf{R}\alpha} + 1, n_{\mathbf{R}'\beta} - 1)$. Thus, in order to calculate $\hat{U}$, it is not sufficient to know the Wannier functions in the ground state. An even more important question is how these Wannier functions will be modified in the process of transfer of an electron from one site of the system to another.

4.2. Random-phase approximation

Another way of calculating the screened Coulomb interaction is to use the random-phase approximation (RPA), which constitutes the basis of the GW method [34–36]. In this case, the effective Coulomb interaction is calculated in terms of the response to an external perturbation of the electron density, $\delta\rho_{\text{ext}}(\mathbf{r})$, which is introduced as a probe of the electron system. RPA has many similarities with the constrained DFT. It consists of the following steps.

(i) $\delta\rho_{\text{ext}}(\mathbf{r})$ creates the Coulomb potential $\delta V_{\text{ext}}(\mathbf{r}) = e^2 \int \mathrm{d}\mathbf{r}' \, |\mathbf{r} - \mathbf{r}'|^{-1} \delta\rho_{\text{ext}}(\mathbf{r}')$, which is similar to $\{V_{\mathbf{R}\alpha}\}$ in the constrained DFT, and $\delta\rho_{\text{ext}}(\mathbf{r})$ itself has a meaning of the electron density, which is controlled by the orbital occupations $\{n_{\mathbf{R}\alpha}\}$.[12] In principle, the perturbation of the electron density can also depend on time [37, 38]. Nevertheless, we will continue to consider only the static (or time-independent) limit, strictly following the definition (18).

(ii) $\delta V_{\text{ext}}(\mathbf{r})$ is treated as a perturbation. Then, the updates for the Kohn–Sham orbitals, $\{\delta\psi_i\}$, are calculated in the first order of $\delta V_{\text{ext}}(\mathbf{r})$, by using regular perturbation theory. In this sense, the screening of the Coulomb interaction in RPA is entirely related with the change of $\{\psi_i\}$ or with the relaxation of the Kohn–Sham orbitals.

(iii) The change of the electron density is calculated from $\{\delta\psi_i\}$ in the first order of $\delta V_{\text{ext}}(\mathbf{r})$, namely, $\delta\rho(\mathbf{r}) = \sum_i [\delta\psi_i^{\dagger}(\mathbf{r})\psi_i(\mathbf{r}) + \psi_i^{\dagger}(\mathbf{r})\delta\psi_i(\mathbf{r})]$.

(iv) $\delta\rho(\mathbf{r})$ results in an additional change of the Coulomb potential, also in the first order of $\delta V_{\text{ext}}(\mathbf{r})$: $\delta V_{\text{H}}(\mathbf{r}) = e^2 \int \mathrm{d}\mathbf{r}' \, |\mathbf{r} - \mathbf{r}'|^{-1} \delta\rho(\mathbf{r}')$.

(v) Steps (ii)–(iv) are repeated for the new potential, $\delta V_{\text{ext}}(\mathbf{r}) + \delta V_{\text{H}}(\mathbf{r})$. Then, the potential is updated again, and so on. This is equivalent to the iterative solution of the Kohn–Sham equations within DFT. The constrained DFT also takes into account the change of the exchange–correlation potential, $V_{\text{XC}}(\mathbf{r})$. However, this change is typically treated in LDA, where the effect is small.

(vi) After summing up an infinite number of updates for $\delta V_{\text{H}}(\mathbf{r})$, the screened Coulomb interaction in RPA is defined as $U(\mathbf{r}, \mathbf{r}') = \delta V_{\text{ext}}(\mathbf{r})/\delta\rho_{\text{ext}}(\mathbf{r}') + \delta V_{\text{H}}(\mathbf{r})/\delta\rho_{\text{ext}}(\mathbf{r}')$.

Then, one can easily to show that $U(\mathbf{r}, \mathbf{r}')$ satisfies the Dyson equation [34, 35]:

$$U(\mathbf{r}, \mathbf{r}') = e^2|\mathbf{r} - \mathbf{r}'|^{-1} + \int \mathrm{d}\mathbf{r}'' \int \mathrm{d}\mathbf{r}''' \, e^2|\mathbf{r} - \mathbf{r}''|^{-1} \mathcal{P}(\mathbf{r}'', \mathbf{r}''') U(\mathbf{r}''', \mathbf{r}'), \tag{23}$$

where $\mathcal{P}(\mathbf{r}, \mathbf{r}')$ is the polarization function, which is obtained from the first-order perturbation theory expansion for $\{\delta\psi_i\}$:

$$\mathcal{P}(\mathbf{r}, \mathbf{r}', \omega) = 2 \sum_{ij} \frac{(f_i - f_j)\psi_i^{\dagger}(\mathbf{r})\psi_j(\mathbf{r})\psi_j^{\dagger}(\mathbf{r}')\psi_i(\mathbf{r}')}{\omega - \varepsilon_j + \varepsilon_i + \mathrm{i}\delta(f_i - f_j)}. \tag{24}$$

The ω-dependence of $\mathcal{P}(\mathbf{r}, \mathbf{r}', \omega)$ corresponds to the time-dependent perturbation $\delta V_{\text{ext}}(\mathbf{r}) \exp(-\mathrm{i}\omega t)$. The static limit corresponds to $\mathcal{P}(\mathbf{r}, \mathbf{r}', 0) \equiv \mathcal{P}(\mathbf{r}, \mathbf{r}')$. The prefactor '2' stands for two spin channels in the case of non-spin-polarized LDA.

4.3. Combining constrained DFT and RPA

The screened Coulomb interactions in RPA satisfies one very important property [39], which directly follows from the Dyson equation (23). Suppose that one can identify two different channels of screening, by dividing the full polarization function (24) into two parts: $\mathcal{P} = \mathcal{P}_1 + \mathcal{P}_2$. Then, the screened Coulomb interaction U can be computed in two steps.

(i) By replacing total $\mathcal{P}$ by $\mathcal{P}_1$ in (23), one can compute the effective interaction U_1, which takes into account only the first channel of screening.

[11] This can be naturally done by reconstructing the Wannier functions from the matrix elements $h^{\alpha\beta}_{\mathbf{R}\mathbf{R}'}$ derived from the downfolded method [22]. Nevertheless, it seems that for many strongly correlated systems, $\{\bar{W}^{\alpha}_{\mathbf{R}}\}$ do not substantially differ from $\{\tilde{W}^{\alpha}_{\mathbf{R}}\}$. The intuitive reason for that is that the transfer integrals in the narrow L-band are typically much smaller in comparison to other effects of covalent mixing, which leads to the separation of the L-band from other bands and mainly determines the shape of the Wannier functions. Another reason is that for strongly correlated systems, the transfer integrals are typically much smaller than the on-site Coulomb interactions. Therefore, to a certain extent it is unimportant whether or not the small transfer integrals are included in the definition of the large Coulomb interactions, as they cause only small changes of these interactions.

[12] Yet, there is also a difference: $\delta V_{\text{ext}}(\mathbf{r})$ is the local potential, whereas $\{V_{\mathbf{R}\alpha}\}$ act on the individual Wannier functions $\{\tilde{W}^{\alpha}_{\mathbf{R}}\}$. This corresponds to the external potential $\delta V_{\text{ext}}(\mathbf{r}, \mathbf{r}') = \sum_{\mathbf{R}\alpha} V_{\mathbf{R}\alpha} |\tilde{W}^{\alpha}_{\mathbf{R}}\rangle\langle\tilde{W}^{\alpha}_{\mathbf{R}}|$ in the form of the projector operators, which are essentially *nonlocal*. This is the one of the basic differences between constrained DFT and RPA. The role of this nonlocality is not fully understood [37].

(ii) Then, the final interaction U, corresponding to $\mathcal{P}_1 + \mathcal{P}_2$, can be obtained from U_1 again by using the Dyson equation (23), but where the full polarization function is replaced by $\mathcal{P}_2$:

$$U(\mathbf{r}, \mathbf{r}') = U_1(\mathbf{r}, \mathbf{r}') + \int d\mathbf{r}'' \int d\mathbf{r}''' \, U_1(\mathbf{r}, \mathbf{r}'')\mathcal{P}_2(\mathbf{r}'', \mathbf{r}''')U(\mathbf{r}''', \mathbf{r}').$$

This property has two important consequences.

(i) In order to calculate U, we would like to start with the LDA band structure. However, for Mott insulators, LDA yields an incorrect metallic behavior in the region of the L-bands. Therefore, we should remove the unphysical metallic screening, which will always appear in RPA if one starts from LDA. More generally, RPA may not be a good approximation for treating the electron correlations in the narrow L-bands. Therefore, the general strategy is to get rid of the RPA self-screening associated with all kinds of transition between L-bands in the polarization function (24), and to replace it by a more rigorous model of screening in the process of the solution of the Hubbard model (3) [21, 39]. The suppression of the transitions between L-bands in RPA is similar to switching off all transfer integrals between Wannier functions in the constrained DFT [22][13].

(ii) Our goal is to evaluate the screening of the Coulomb interactions associated with the relaxation of the Wannier functions $\{\tilde{W}^{\alpha}_{\mathbf{R}}\}$ in the region of L-bands as well as of all other Kohn–Sham orbitals $\{\psi_i\}$ in the remaining part of the spectrum. Suppose that we are working in a (flexible) basis of atomic orbitals $\{\tilde{\chi}^{\alpha}_{\mathbf{R}}\}$, and both $\{\tilde{W}^{\alpha}_{\mathbf{R}}\}$ and $\{\psi_i\}$ are expanded over this basis:

$$\left\{ \begin{matrix} \tilde{W}^{\alpha}_{\mathbf{R}} \\ \psi_i \end{matrix} \right\} = \sum_{\mathbf{R}'\beta} c^{\beta}_{\mathbf{R}'} \tilde{\chi}^{\beta}_{\mathbf{R}'}. \tag{25}$$

Then, within linear response theory, the relaxation of $\{\tilde{W}^{\alpha}_{\mathbf{R}}\}$ and $\{\psi_i\}$ will consist of two parts: the relaxation of the basis functions $\{\tilde{\chi}^{\alpha}_{\mathbf{R}}\}$ and the relaxation of the coefficients $\{c^{\alpha}_{\mathbf{R}}\}$ of the expansion over these basis functions, which corresponds to a change of the hybridization in the process of screening. Therefore, it has been proposed (though somewhat heuristically) that the screened Coulomb interactions in the L-band can be computed in two steps [22, 37]. For the sake of clarity, let us assume the main contribution to the L-bands comes from the 3d orbitals of the transition-metal sites.

(a) The first step takes into account the screening caused by the relaxation of the basis functions $\{\tilde{\chi}^{\alpha}_{\mathbf{R}}\}$. It can be easily evaluated in the framework of constrained DFT. In this case, the Kohn–Sham equations are solved numerically on a finite grid of points in the real space, and $\{n_{\mathbf{R}\alpha}\}$ are the constrained 3d occupation numbers inside certain atomic spheres [29]. On the other hand, since RPA is based on the perturbation theory expansion, similar calculations in terms of the polarization function (24) would require an enormous number of states $\{\psi_i\}$, both in the occupied and unoccupied parts of the spectrum. Probably, this is one of the reasons why the conventional RPA calculations converge very slowly with the increase of the number of bands in the unoccupied part of the spectrum [40], and are extremely sensitive to the treatment of the core states [35]. The screening caused by the relaxation of the Kohn–Sham orbitals $\{\psi_i\}$ in the subspace orthogonal to L (for example, the screening of localized 3d electrons by outer electrons in the transition-metal compounds) can be also easily taken into account in the conventional constrained DFT calculations [30–32].

(b) However, what the constrained DFT cannot do is to treat the screening of Coulomb interactions amongst 3d electrons by *the same* 3d electrons [37, 41][14]. Since the atomic 3d occupation numbers are rigidly fixed by the constraint conditions, the 3d electrons from other sites of the system cannot compensate the change of the number of the 3d electrons at the central site, and vice versa. However, such a channel of screening may exist. Suppose that our L-band is mainly constructed from the transition-metal 3d orbitals (the concrete example is the t_{2g} band in the transition-metal oxides), and there is another, say oxygen 2p band, which has an appreciable weight of the atomic 3d orbitals (of both t_{2g} and e_g symmetry) coming from the hybridization between oxygen and transition-metal sites (figure 2). Furthermore, the redistribution of the electron density in the t_{2g} band, associated with the reaction $(n_{\mathbf{R}\alpha}, n_{\mathbf{R}'\beta}) \rightleftharpoons (n_{\mathbf{R}\alpha} + 1, n_{\mathbf{R}'\beta} - 1)$, will change the Coulomb potential around each transition-metal site. If the number of t_{2g} electrons is increased by the constraint conditions, the Coulomb potential becomes more repulsive and vice versa. The more repulsive Coulomb potential will additionally push the 3d states from the oxygen 2p band to the higher-energy part of the spectrum. Therefore, around certain transition-metal sites, the change of the number of 3d electrons in the t_{2g} band will be partly compensated by the change of the 3d-electron density in the region of oxygen 2p band. This channel of screening can be easily evaluated in RPA, by rewriting (23) in the matrix form

$$\hat{U} = \left[1 - \hat{u}\hat{\mathcal{P}}\right]^{-1} \hat{u}, \tag{26}$$

and assuming that all other channels of screening are already included in the definition of the 'bare Coulomb interaction' $\hat{u}$, derived from the constrained

[13] Indeed, suppose that we have replaced $\{\psi_i\}$ for the L-bands in (24) by the Wannier functions $\{\tilde{W}^{\alpha}_{\mathbf{R}}\}$, and switched off all transfer integrals. In the ground state of such an auxiliary system, all occupation numbers are equal, $f_i = f_j$. Therefore, the polarization function (24) will vanish.

[14] The procedure implies that the atomic 3d charges can be divided into two parts, where the first part is subject to the constraint conditions, while the second part is allowed to participate in the screening. Although, it can be formally done within constrained DFT [42], the actual computational scheme is rather laborious, and in many cases the procedure of dividing the atomic charges into the 'screened' and 'screening' parts is not well defined.

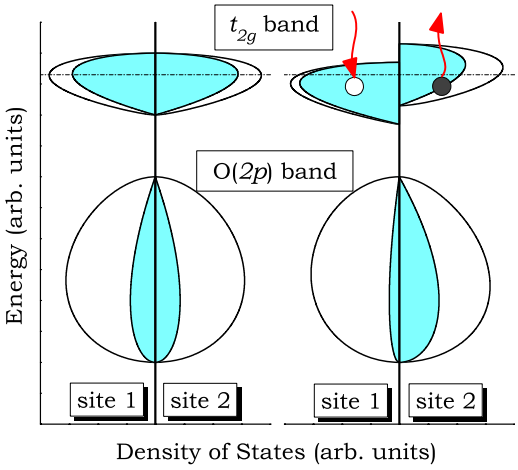

Figure 2. A schematic view of the change of the p–d hybridization in the oxygen 2p and t_{2g} bands of the transition-metal oxides associated with the repopulation of the Wannier orbitals at the neighboring transition-metal sites on both sides of the reaction $2(d^n) \rightleftharpoons d^{n+1} + d^{n-1}$. The left panel corresponds to the ground-state configuration, $2d^n$. In the right panel, the removal (addition) of an electron from (to) the Wannier orbital in the t_{2g} part of the spectrum is simulated by the shift of these orbitals relative to the Fermi level (shown by the dot–dashed line). Around each transition-metal site, it changes the Coulomb potential, which controls the distribution of the 3d states as well as the hybridization between transition-metal 3d and oxygen 2p states. Generally, the removal of an electron from (or the addition of an electron to) the Wannier orbital is partially compensated by the change of the amount of the 3d states (shown by the shaded area), which is admixed into the oxygen 2p band. This transfer of the spectral weight works as an efficient channel for screening of the local Coulomb interactions in the transition-metal oxides [22].

DFT [22]. Since the polarization matrix $\hat{\mathcal{P}}$ in (26) is aimed at describing the self-screening of the 3d electrons, it should consist of the matrix elements of (24) in the basis of atomic 3d orbitals, after the subtraction of the unphysical metallic screening associated with RPA transitions between t_{2g} band.

5. Solution of model Hamiltonian

It is virtually impossible to provide a comprehensive analysis of all possible methods for the solution of the low-energy model (3), and this is definitely beyond the scope of this review article.

One option is the dynamical mean-field theory (DMFT) [43], which has become one of the popular low-energy solvers today. The idea of DMFT is to map the many-body lattice problem to a single-site impurity problem with effective parameters. The vast majority of DMFT applications for realistic compounds have been focusing on the analysis of spectroscopic properties, especially in the context of the metal–insulator transition, although some extensions for the ground-state properties, such as calculations of the total energies and phonons, are also available today. Many examples of recent applications of DMFT can be found in the review articles [44–46]. The conventional DMFT becomes exact in the limit of infinite coordination numbers or, equivalently, infinite dimensions, when all nonlocal correlations vanish. In order to treat these nonlocal correlations, it is essential to go beyond the single-site approximation. This is one of the challenging problems in DMFT, and the recent progress along this line can be found in [47]. Another limitation of DMFT is that, in order to be exact, it is typically used in combination with the quantum Monte Carlo (QMC) method, which provides an exact solution for the impurity model. However, current applications of the QMC method are typically restricted by rather high temperatures, which are substantially higher than, for example, the magnetic transition temperatures in many strongly correlated compounds. From this point of view, the method does not appear to be sufficiently useful for studying the phenomena of spin and orbital ordering. Probably, some of these difficulties may be overcome by applying the projective QMC method [48].

Unlike DMFT, the path-integral renormalization group (PIRG) method is mainly oriented towards the description of the ground-state properties of strongly correlated systems. The entire procedure includes the following steps [49–51]:

(i) The numerical construction of truncated basis of $\mathcal{L}$ Slater determinants, which provides the best representation for the ground-state wavefunction;
(ii) Calculation of the total energy and its variance in the obtained basis;
(iii) Extrapolation of the obtained results to the full Hilbert space, which is achieved by a systematic increase of $\mathcal{L}$.

The PIRG method has been recently applied as a low-energy solver for studying the correlation effects in the t_{2g} bands of Sr_2VO_4 [21] and YVO_3 [52].

In the rest of this section we will discuss some details of the solution of the model Hamiltonian (3), which will be directly used for applications considered in section 6. We start with the simplest Hartree–Fock method, which totally neglects the correlation effects. Then, we consider simple corrections to the Hartree–Fock approximation, which include some of these effects. One is the perturbation theory for the total energy, and the other one is the variational superexchange theory.

All model calculations are performed in the basis of Wannier functions $\{\tilde{W}^{\alpha}_{\mathbf{R}}\}$, which have a finite weight at the central transition-metal site as well as the oxygen and other atomic sites located in its neighborhood. In order to calculate the local quantities, associated with the transition-metal atoms, such as spin and orbital magnetic moments or the distribution of the electron density, the Wannier functions are expanded over the original basis $\{\tilde{\chi}^{\alpha}_{\mathbf{R}}\}$. Then, all aforementioned quantities are calculated by integrating over appropriate regions of the real space surrounding the transition-metal sites, like the atomic spheres in the linear-muffin-tin-orbital (LMTO) method [13–15].

5.1. Hartree–Fock approximation

The Hartree–Fock method provides the simplest approximation to the many-body problem (3). In this case, the trial many-electron wavefunction is searched for in the form of a single

Slater determinant $|S\{\varphi_k\}\rangle$, constructed from the one-electron orbitals $\{\varphi_k\}$. In this notation, k is a collective index combining the momentum $\mathbf{k}$ of the first Brillouin zone, the band number, and the spin ($s = \uparrow$ or $\downarrow$) of the particle. The one-electron orbitals are subjected to the variational principle and required to minimize the total energy

$$E_{\mathrm{HF}} = \min_{\{\varphi_k\}} \langle S\{\varphi_k\}|\hat{\mathcal{H}}|S\{\varphi_k\}\rangle$$

for a given number of particles $\mathcal{N}$. This minimization is equivalent to the solution of the Hartree–Fock equations for $\{\varphi_k\}$:

$$\left(\hat{h}_{\mathbf{k}} + \hat{\mathcal{V}}\right)|\varphi_k\rangle = \varepsilon_k|\varphi_k\rangle, \tag{27}$$

where $\hat{h}_{\mathbf{k}} \equiv \|h_{\mathbf{k}}^{\alpha\beta}\|$ is the one-electron part of the model Hamiltonian (3) in the reciprocal space, $h_{\mathbf{k}}^{\alpha\beta} = \sum_{\mathbf{R}'} h_{\mathbf{R}\mathbf{R}'}^{\alpha\beta} \mathrm{e}^{-\mathrm{i}\mathbf{k}\cdot(\mathbf{R}-\mathbf{R}')}$, and $\hat{\mathcal{V}} \equiv \|\mathcal{V}_{\alpha\beta}\|$ is the Hartree–Fock potential[15],

$$\mathcal{V}_{\alpha\beta} = \sum_{\gamma\delta} \left(U_{\alpha\beta\gamma\delta} - U_{\alpha\delta\gamma\beta}\right) n_{\gamma\delta}. \tag{28}$$

Equation (27) is solved self-consistently together with the equation

$$\hat{n} = \sum_{k}^{occ} |\varphi_k\rangle\langle\varphi_k|$$

for the density matrix $\hat{n} \equiv \|n_{\alpha\beta}\|$ in the basis of Wannier functions. After iterative solution of the Hartree–Fock equations, the total energy can be computed as

$$E_{\mathrm{HF}} = \sum_{k}^{occ} \varepsilon_k - \tfrac{1}{2} \sum_{\alpha\beta} \mathcal{V}_{\beta\alpha} n_{\alpha\beta}.$$

By knowing $\{\varepsilon_k\}$ and $\{\varphi_k\}$, one can construct the one-electron (retarded) Green function,

$$\hat{\mathcal{G}}_{\mathbf{R}\mathbf{R}'}(\omega) = \sum_{k} \frac{|\varphi_k\rangle\langle\varphi_k|}{\omega - \varepsilon_k + \mathrm{i}\delta} \mathrm{e}^{\mathrm{i}\mathbf{k}\cdot(\mathbf{R}-\mathbf{R}')},$$

which can be used for many applications. For example, the inter-atomic magnetic interactions corresponding to infinitesimal rotations of spin magnetic moments near equilibrium can be computed as [53, 54]:

$$J_{\mathbf{R}\mathbf{R}'} = \frac{1}{2\pi} \mathrm{Im} \int_{-\infty}^{\varepsilon_{\mathrm{F}}} \mathrm{d}\omega \, \mathrm{Tr}_L \left\{\hat{\mathcal{G}}_{\mathbf{R}\mathbf{R}'}^{\uparrow}(\omega) \Delta\hat{\mathcal{V}} \hat{\mathcal{G}}_{\mathbf{R}'\mathbf{R}}^{\downarrow}(\omega) \Delta\hat{\mathcal{V}}\right\}, \tag{29}$$

where $\hat{\mathcal{G}}_{\mathbf{R}\mathbf{R}'}^{\uparrow,\downarrow} = \frac{1}{2}\mathrm{Tr}_S\{(\hat{1} \pm \hat{\sigma}_z)\hat{\mathcal{G}}_{\mathbf{R}\mathbf{R}'}\}$ is the projection of the Green function onto the majority ($\uparrow$) and minority ($\downarrow$) spin states, $\Delta\hat{\mathcal{V}} = \mathrm{Tr}_S\{\hat{\sigma}_z\hat{\mathcal{V}}\}$ is the magnetic (spin) part of the Hartree–Fock potential, Tr_S (Tr_L) denotes the trace over the spin (orbital) indices, $\hat{1}$ and $\hat{\sigma}_z$ are the unity and Pauli matrix, respectively, and ε_{F} is the Fermi energy[16].

[15] For the sake of simplicity, we drop the atomic index $\mathbf{R}$ in the notation of $\mathcal{V}_{\alpha\beta}$, although such a dependence can take place (for example, in the case of inequivalent transition-metal sites in the distorted perovskite structure), and was actually taken into account in realistic calculations considered in section 6.

[16] According to the definition (29), $J_{\mathbf{R}\mathbf{R}'} > 0$ (<0) means that for a given magnetic state, the spin arrangement in the bond $\langle\mathbf{R}\mathbf{R}'\rangle$ corresponds to the local minimum (maximum) of the total energy. However, in the following we will use the universal notation, according to which $J_{\mathbf{R}\mathbf{R}'} > 0$ and <0 will stand for the ferromagnetic and antiferromagnetic coupling, respectively.

The parameters $\{J_{\mathbf{R}\mathbf{R}'}\}$ are not universal, and depend on the magnetic state in which they are calculated, for example, through the change of the orbital ordering [5] or the change of the electronic structure by the magnetic ordering [7, 55].

5.2. Second-order perturbation theory for the correlation energy

The simplest way of going beyond the Hartree–Fock approximation is to include the correlation interactions in the second order perturbation theory for the total energy [56–58]. It shares common problems with the regular (nondegenerate) perturbation theory. Nevertheless, by using this technique one can calculate, relatively easily, the corrections to the total energy, starting from the Hartree–Fock wavefunctions. This method is expected to work well for systems where the orbital degeneracy is lifted (for example, by crystal-field splitting) and the ground state is described reasonably well by a single Slater determinant, so that other corrections can be treated as a perturbation.

The correlation interaction (or the interaction of fluctuations) is defined as the difference between the true many-body Hamiltonian (3), and its one-electron counterpart, obtained at the level of the Hartree–Fock approximation:

$$\hat{\mathcal{H}}_C = \sum_{\mathbf{R}} \left(\tfrac{1}{2} \sum_{\alpha\beta\gamma\delta} U_{\alpha\beta\gamma\delta} \hat{c}_{\mathbf{R}\alpha}^{\dagger} \hat{c}_{\mathbf{R}\gamma}^{\dagger} \hat{c}_{\mathbf{R}\beta} \hat{c}_{\mathbf{R}\delta} - \sum_{\alpha\beta} \mathcal{V}_{\alpha\beta} \hat{c}_{\mathbf{R}\alpha}^{\dagger} \hat{c}_{\mathbf{R}\beta} \right). \tag{30}$$

It is important to note that although some of the matrix elements $U_{\alpha\beta\gamma\delta}$ can be large, they also contribute to the Hartree–Fock potentials $\mathcal{V}_{\alpha\beta}$. Therefore, generally, one can expect some cancelation of contributions in the first and second parts of (30), which formally extends the applicability of the perturbation theory even for relatively large $U_{\alpha\beta\gamma\delta}$. For example, in a number of cases such a strategy can be applied even for the bare Coulomb interactions in isolated atoms [59].

By treating $\hat{\mathcal{H}}_C$ as a perturbation, the correlation energy can be easily estimated as [56–59]:

$$E_C^{(2)} = -\sum_{S} \frac{\langle G|\hat{\mathcal{H}}_C|S\rangle\langle S|\hat{\mathcal{H}}_C|G\rangle}{E_{\mathrm{HF}}(S) - E_{\mathrm{HF}}(G)}, \tag{31}$$

where $|G\rangle$ and $|S\rangle$ are the Slater determinants corresponding to the low-energy ground state (in the Hartree–Fock approximation), and the excited state, respectively. Due to the variational properties of the Hartree–Fock method, the only processes that may contribute to $E_C^{(2)}$ are the two-particle excitations, for which each of $|S\rangle$ is obtained from $|G\rangle$ by replacing two one-electron orbitals, say φ_{k_1} and φ_{k_2}, from the occupied part of the spectrum by two unoccupied orbitals, say φ_{k_3} and φ_{k_4} [59]. Hence, using the notation of section 2, the matrix elements take the following form:

$$\langle S|\hat{\mathcal{H}}_C|G\rangle = \langle k_3k_4|v_{\mathrm{scr}}|k_1k_2\rangle - \langle k_3k_4|v_{\mathrm{scr}}|k_2k_1\rangle. \tag{32}$$

By further employing the approximation of noninteracting quasiparticles, the denominator in (31) can be replaced by the linear combination of Hartree–Fock eigenvalues: $E_{\mathrm{HF}}(S) - E_{\mathrm{HF}}(G) \approx \varepsilon_{k_3} + \varepsilon_{k_4} - \varepsilon_{k_1} - \varepsilon_{k_2}$ [56–59]. The matrix

elements (32) satisfy the following condition: $\langle S|\hat{\mathcal{H}}_C|G\rangle \sim \frac{1}{N}\sum_{\mathbf{R}} e^{i(\mathbf{k}_3+\mathbf{k}_4-\mathbf{k}_1-\mathbf{k}_2)\cdot\mathbf{R}}$ (N being the number of sites), provided that the effective Coulomb interactions are diagonal with respect to the site indices. In the second-order perturbation theory one can estimate relatively easily both on-site ($\mathbf{R}=0$) and inter-site ($\mathbf{R}\neq 0$) contributions to $E_C^{(2)}$. The $\mathbf{R}=0$ term corresponds to the commonly used single-site approximation for the correlation interactions, which becomes exact in the limit of infinite spacial dimensions [43].

In principle, one can go beyond the second-order perturbation theory and consider, for example, the single-site approximation for the T-matrix [60]. In this case, the expression for the energy of electron–electron interactions has the same form as in the Hartree–Fock method, but with $\hat{U}$ being replaced by the effective T-matrix, which takes into account the correlation effects. The method has been employed for the series of distorted transition-metal perovskite oxides [61], where the degeneracy of the Hartree–Fock ground state is lifted by the crystal field. It that case, the application of the T-matrix theory changed only some quantitative conclusions, whereas the main trends for the correlation energy were captured already by the second-order perturbation theory.

5.3. Atomic multiplet structure and superexchange interactions

The variational superexchange theory takes into account the multiplet structure of the excited atomic states. By using this technique one can study the effect of the electron correlations on the spin and orbital ordering. However, it is limited by typical approximations made in the theory of superexchange interactions, which treat all transfer integrals as a perturbation.

The superexchange interaction in the bond $\langle\mathbf{R}\mathbf{R}'\rangle$ is basically the gain of the kinetic energy, which is acquired by an electron at the center $\mathbf{R}$ in the process of virtual hopping into the subspace of unoccupied orbitals at the center $\mathbf{R}'$, and vice versa [10, 11]. Therefore, the energy gain caused by virtual hopping in the bond $\langle\mathbf{R}\mathbf{R}'\rangle$ can be found as [5, 10, 62]:

$$\mathcal{T}_{\mathbf{R}\mathbf{R}'} = -\langle G|\hat{h}_{\mathbf{R}\mathbf{R}'}\left(\sum_M \frac{\hat{\mathscr{P}}_{\mathbf{R}'}|\mathbf{R}'M\rangle\langle\mathbf{R}'M|\hat{\mathscr{P}}_{\mathbf{R}'}}{E_{\mathbf{R}'M}}\right)\hat{h}_{\mathbf{R}'\mathbf{R}} + (\mathbf{R}\leftrightarrow\mathbf{R}')|G\rangle, \quad (33)$$

where G is the ground-state wavefunction of the lattice of isolated centers[17], each of which accommodates n electrons, $E_{\mathbf{R}'M}$ and $|\mathbf{R}'M\rangle$ stand for the eigenvalues and eigenvectors of the excited ($n+1$ electron) configurations of the center $\mathbf{R}'$, and $\hat{\mathscr{P}}_{\mathbf{R}'}$ is a projector operator, which enforces the Pauli principle and suppresses any hopping into the subspace of occupied orbitals at the center $\mathbf{R}'$ [5].

The formulation is extremely simple for the $n=1$ compounds, like $YTiO_3$ and $LaTiO_3$. In this case, there is only one electron residing at each transition-metal site. This is essentially an one-electron problem, where each atomic state is described by certain one-electron orbital $\varphi_{\mathbf{R}}$ and G is the single Slater determinant constructed from $\{\varphi_{\mathbf{R}}\}$ belonging to different transition-metal sites [5]. A similar formulation can be performed for the hole spin–orbitals $\{\alpha_{\mathbf{R}}\}$ of compounds where at each lattice center there is only one unbalanced hole. Such a situation holds for the alkali hyperoxides, which will be considered in section 6.4.

The total energy of the system in the superexchange approximation is obtained after summation over all bonds, which should be combined with the site-diagonal elements, incorporating the effects of the crystal-field splitting and the relativistic spin–orbit interaction:

$$E_{\mathrm{SE}} = \sum_{\mathbf{R}}\langle\varphi_{\mathbf{R}}|\hat{h}_{\mathbf{R}\mathbf{R}}|\varphi_{\mathbf{R}}\rangle + \sum_{\langle\mathbf{R}\mathbf{R}'\rangle}\mathcal{T}_{\mathbf{R}\mathbf{R}'}.$$

Finally, the set of occupied orbitals $\{\varphi_{\mathbf{R}}\}$ is obtained by minimizing E_{SE}. This can be done by using, for instance, the steepest descent method.

6. Examples and applications for realistic compounds

6.1. Cubic perovskites: $SrVO_3$

$SrVO_3$ is a rare example of a perovskite compound, which crystallizes in the ideal cubic structure. It has attracted considerable attention in connection with the bandwidth control of the metal–insulator transition [4, 63]. The region of interest is the t_{2g} band, which is located near the Fermi level (figure 3).

6.1.1. Transfer integrals and Wannier functions. For cubic compounds, the separation of the basis functions into $\{\tilde{\chi}^t_{\mathbf{R}}\}$ and $\{\tilde{\chi}^r_{\mathbf{R}}\}$, which is required in the downfolding method, is rather straightforward: three t_{2g} orbitals centered at each vanadium site of $SrVO_3$ are taken as the $\{\tilde{\chi}^t_{\mathbf{R}}\}$ orbitals, and the rest of the basis functions is associated with the $\{\tilde{\chi}^r_{\mathbf{R}}\}$ orbitals.

The downfolding procedure is nearly perfect and reproduces well the behavior of three t_{2g} bands (figure 4). As expected for cubic compounds, the nearest-neighbor ddπ-interactions mediated by the oxygen 2p orbitals are the strongest (table 1). For the xy-orbitals, it operates in the x

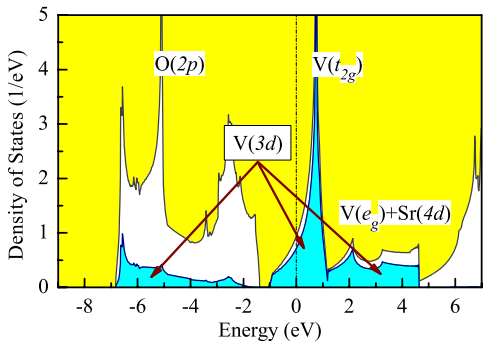

Figure 3. Total and partial densities of states of $SrVO_3$ in the local-density approximation. The shaded area shows the contributions of the vanadium 3d states. Other symbols show positions of the main bands. The Fermi level is at zero energy.

[17] In the present context, the 'lattice center' means either isolated atomic site or a molecule. An example of the molecular solid will be considered in section 6.4.

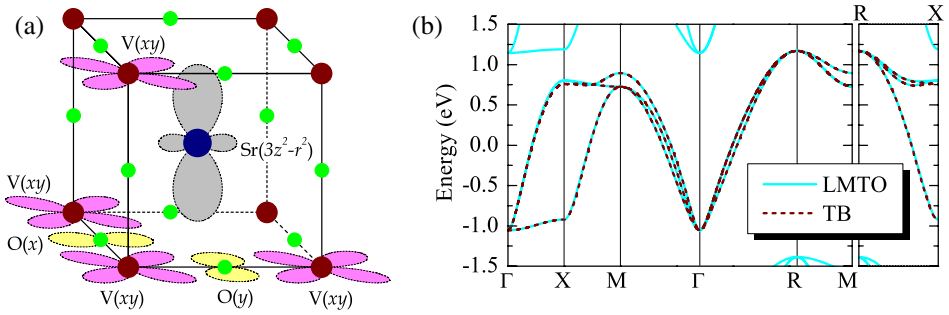

Figure 4. Left panel: crystal structure of cubic perovskites and atomic wavefunctions mediating transfer interactions between vanadium t_{2g} orbitals. The standard V(xy)–O(y)–V(xy) and V(xy)–O(x)–V(xy) interactions operate in the x- and y-directions, respectively. The V(xy)–Sr($3z^2 - r^2$)–V(xy) interaction operate in the 'forbidden' z-direction. Right panel: LDA energy bands of $SrVO_3$ obtained in the original electronic structure calculations using the LMTO method and after the 'tight-binding' (TB) parametrization using the downfolding method. Notations of the high-symmetry points of the Brillouin zone are taken from [65].

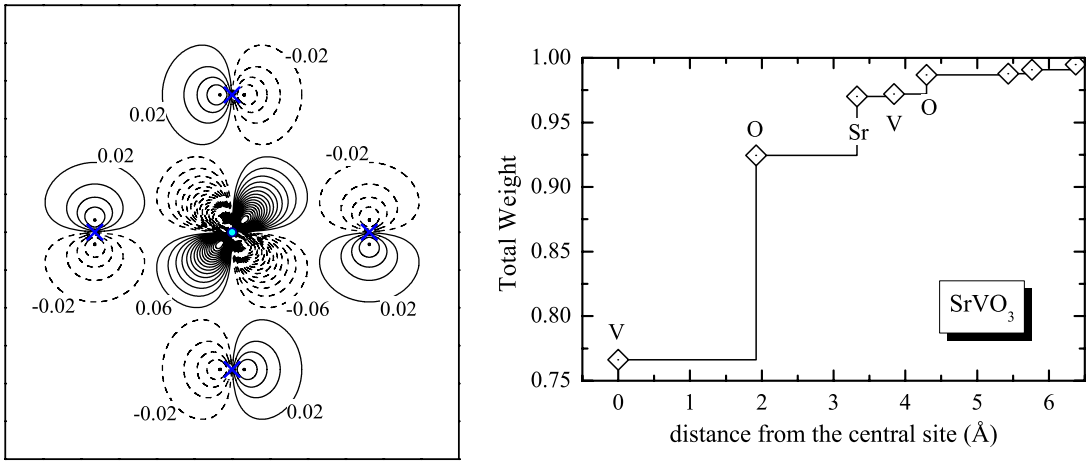

Figure 5. Wannier function for the t_{2g} band of $SrVO_3$ [22]. The left panel shows the contour plot of the xy-orbital in the (001) plane. The solid and dashed lines correspond to the positive and negative values of the Wannier function. The vanadium atom is located in the center of the plot, and other sites are four oxygen atoms located in its nearest neighborhood. Around each site, the Wannier function increases/decreases with a step 0.04 from the values indicated on the graph. The right panel shows the total weight of the Wannier function accumulated around the central vanadium site after adding every new sphere of the neighboring sites.

and y directions[18]. However, there is also an appreciable ddδ interaction operating in the 'forbidden' direction (for example, the direction z in the case of the xy orbitals). These interactions are mediated by the strontium 4d orbitals and strongly depend on the proximity of the latter to the Fermi level. The transfer integrals connecting different t_{2g} orbitals are small and contribute only to the longer-range interactions separated by the vectors $(a, a, 0)$ and (a, a, a), where a is the cubic lattice parameter [64]. Other interactions are considerably smaller.

The shape of the Wannier functions is explained in figure 5.[19] Since the t_{2g} band is an *antibonding* combination of the atomic vanadium 3d-t_{2g} and oxygen 2p orbitals, the Wannier function has nodes between vanadium and oxygen sites. The right panel of figure 5 illustrates the spacial extension of the Wannier functions. It shows the weight of the Wannier function accumulated around the central vanadium site after adding every new sphere of the neighboring sites. Since Wannier functions are normalized, their total weight is equal to one. In the case of $SrVO_3$, 77% of this weight belongs to the central vanadium site, 16% is distributed over four neighboring oxygen sites, about 5% belongs to the next eight strontium sites, and 1%—to the eight oxygen sites located in the fourth coordination sphere. Other contributions are small. Another quantity, characterizing the spread of the Wannier

Table 1. Transfer integrals (in meV) between first, second, and third nearest neighbors in $SrVO_3$, separated by the vectors $(a, 0, 0)$, $(a, a, 0)$, and (a, a, a), respectively (a being the cubic lattice parameter).

	$(a, 0, 0)$			$(a, a, 0)$			(a, a, a)		
	xy	yz	zx	xy	yz	zx	xy	yz	zx
xy	−210	0	0	−84	0	0	−6	3	3
yz	0	−23	0	0	11	11	3	−6	3
zx	0	0	−210	0	11	11	3	5	−6

[18] Similar dependencies for the yz and zx orbitals are obtained by the cyclic permutation of the indices x, y, and z.

[19] These Wannier functions have been reconstructed from the one-electron part of the downfolded Hamiltonian using the ideas of the LMTO method [13–15]. The procedure has been explained in [22].

functions, is the expectation value of square of the position operator, $\langle \mathbf{r}^2 \rangle = \langle \tilde{W}_{\mathbf{R}} | (\mathbf{r} - \mathbf{R})^2 | \tilde{W}_{\mathbf{R}} \rangle$ [16], which in the case of $SrVO_3$ is about 2.37 Å^2 [22].[20]

For cubic perovskites, the transfer integrals can be extracted from first-principles electronic structure calculations in several different ways. For example, one can simply fit the LDA band structure in terms of the Slater–Koster parameters [64]. However, the situation becomes increasingly complicated in materials with lower crystal symmetry, like the distorted perovskite oxides, which will be considered below. First, the number of the Slater–Koster parameters, permitted by the symmetry, increases dramatically. Second, the form of these transfer integrals becomes more complicated and differs substantially from cubic compounds[21]. Therefore, it seems that for complex systems the only way to proceed is to use straightforward numerical algorithms, like the formal downfolding method.

6.1.2. Effective interactions. Applications of constrained DFT to the transition-metal oxides have been widely discussed in the literature [30, 67–70]. For example, the effective Coulomb interaction between 3d electrons in $SrVO_3$ can be computed in the following way [22]:

(i) In the supercell geometry, one can introduce the 'charge-density wave', describing the modulation of the atomic 3d occupations around the 'ground-state' configuration with $n = 1$: $n^{\mathbf{q}}_{\mathbf{R}} = n + \delta n \cos(\mathbf{qR})$, where $\mathbf{q}$ is the propagation vector of the charge-density wave.
(ii) Then, from the constrained DFT calculations, one can derive the Kohn–Sham eigenvalues $\{\varepsilon^{\mathbf{q}}_{\mathbf{R}}\}$, corresponding to this charge-density wave, and find the Fourier image of the effective Coulomb interaction as $u_{\mathbf{q}} = \mathrm{d}\varepsilon^{\mathbf{q}}_{\mathbf{R}}/\mathrm{d}n^{\mathbf{q}}_{\mathbf{R}}$.
(iii) Finally, the parameters of Coulomb interaction in the real space are obtained after the Fourier transformation of $u_{\mathbf{q}}$.[22]

For $SrVO_3$, this procedure yields the following parameters of the on-site Coulomb interaction $u = 10.1$ eV and the nearest-neighbor Coulomb interaction $v = 1.2$ eV. The intra-atomic exchange interaction (j) can be derived by constraining the 3d magnetization density [29, 67][23]. This yields $j = 1.0$ eV. By knowing only u and j, in the atomic limit, one can reconstruct the full $5 \times 5 \times 5 \times 5$ matrix $\hat{u}$ of interactions between the 3d electrons, as it is typically done in the LDA + U method [71]. Some details of this procedure are explained in appendix A.

In order to appreciate the magnitude of screening of different interaction parameters obtained in the constrained DFT, it is instructive to compare them with *bare* interactions. For example, the values of bare Coulomb and exchange integrals, calculated from 3d wavefunctions of the vanadium atoms, are 21.7 and 1.2 eV, respectively. The bare Coulomb interaction between neighboring vanadium sites, e^2/a, is about 3.7 eV. Thus, in the constrained DFT, the on-site Coulomb interaction is reduced by a factor two, the inter-site Coulomb interaction is reduced by almost 70%, and the intra-atomic exchange interaction is reduced by 20%. All these interactions are further reduced by relaxation effects, related to the change of the hybridization.

As was already pointed out in section 4.3, because of the hybridization, the transition-metal 3d states may have a significant weight in other bands. For example, in $SrVO_3$ besides the vanadium t_{2g} band, the 3d states contribute to the vanadium e_g as well as to the oxygen 2p bands (figure 6). If the number of t_{2g} electrons changes, it causes some change of the Coulomb potential, which affects the distribution of the vanadium 3d states in other parts of the spectrum. For example, if at certain vanadium site, the number of t_{2g} electrons increases, the Coulomb potential becomes more repulsive. Therefore, the 3d states of this vanadium site will be pushed from the oxygen 2p band to a higher-energy region. This causes some change of the coefficients $\{c^{\beta}_{\mathbf{R}}\}$ of the expansion of the Kohn–Sham orbitals over the basis functions (25) or a change of the hybridization. This mechanism is responsible for an additional channel of screening of Coulomb interactions, which can be evaluated within RPA. In these calculations, the matrix $\hat{u}$, obtained in the constrained DFT method is used as the starting point, while the RPA itself is employed in order to evaluate the screening of 3d interactions in the vanadium t_{2g} band by the same 3d states, which contribute to other bands. Thus, the problem is reduced to evaluation of the 3d matrix elements of the polarization function (24).

According to the electronic structure of $SrVO_3$, one can identify three main contributions to the polarization function, associated with the following interband transitions: oxygen 2p $\rightarrow$ vanadium e_g, oxygen 2p $\rightarrow$ vanadium t_{2g}, and vanadium $t_{2g} \rightarrow$ vanadium e_g.

The details of RPA screening are explained in figure 6. For this purpose, it is convenient to introduce three Kanamori parameters [60]: the intraorbital Coulomb interaction

$$\mathcal{U} = \int \mathrm{d}\mathbf{r} \int \mathrm{d}\mathbf{r}'\, \tilde{W}^{\dagger}_{xy}(\mathbf{r}) \tilde{W}_{xy}(\mathbf{r}) v_{\mathrm{scr}}(\mathbf{r}, \mathbf{r}') \tilde{W}^{\dagger}_{xy}(\mathbf{r}') \tilde{W}_{xy}(\mathbf{r}'),$$

the interorbital Coulomb interaction

$$\mathcal{U}' = \int \mathrm{d}\mathbf{r} \int \mathrm{d}\mathbf{r}'\, \tilde{W}^{\dagger}_{xy}(\mathbf{r}) \tilde{W}_{xy}(\mathbf{r}) v_{\mathrm{scr}}(\mathbf{r}, \mathbf{r}') \tilde{W}^{\dagger}_{yz}(\mathbf{r}') \tilde{W}_{yz}(\mathbf{r}'),$$

and the exchange interaction

$$\mathcal{J} = \int \mathrm{d}\mathbf{r} \int \mathrm{d}\mathbf{r}'\, \tilde{W}^{\dagger}_{xy}(\mathbf{r}) \tilde{W}_{yz}(\mathbf{r}) v_{\mathrm{scr}}(\mathbf{r}, \mathbf{r}') \tilde{W}^{\dagger}_{xy}(\mathbf{r}') \tilde{W}_{yz}(\mathbf{r}').$$

[20] A somewhat smaller value (1.91 Å^2) has been reported in [66]. Some overestimation of $\langle \mathbf{r}^2 \rangle$ is caused by additional approximations used in the process of reconstructing the Wannier functions from the downfolded one-electron Hamiltonian, which has been employed in [22]. Presumably, the direct application of the projector-operator method can do a better job. Nevertheless, as it was already pointed out in section 3.3, after the transformation (15) of the Kohn–Sham Hamiltonian, the transfer integrals derived from the downfolding method are totally equivalent to the ones obtained in the projector-operator method. Thus, although the Wannier functions reported in [22] may suffer from some additional approximations, the transfer integrals are essentially correct.

[21] One example is the mixing of the t_{2g} and e_g orbitals by the orthorhombic distortion, which does not occur in the cubic compounds.

[22] For example, by considering only on-site (u) and nearest-neighbor inter-site (v) interactions, we would have $u_{\mathbf{q}} = u - v \sum_{\mathbf{R}} \cos(\mathbf{qR})$, etc.

[23] For example, if $m_{\mathbf{R}}$ is the 3d magnetization, $m_{\mathbf{R}} = n^{\uparrow}_{\mathbf{R}} - n^{\downarrow}_{\mathbf{R}}$, and $\varepsilon^{\uparrow}_{\mathbf{R}}$ and $\varepsilon^{\downarrow}_{\mathbf{R}}$ are the Kohn–Sham eigenvalues for the majority- and minority-spin states, respectively, the intra-atomic exchange interaction is given by $j = 2\mathrm{d}(\varepsilon^{\downarrow}_{\mathbf{R}} - \varepsilon^{\uparrow}_{\mathbf{R}})/\mathrm{d}m_{\mathbf{R}}$.

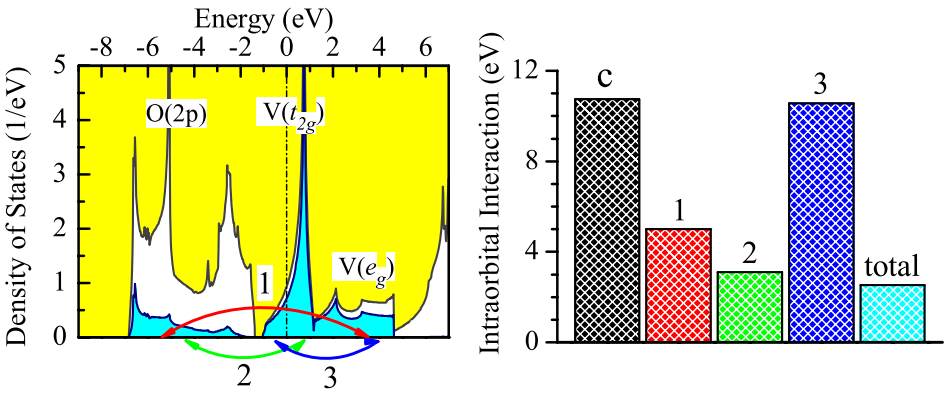

Figure 6. The left panel shows the local density of states of $SrVO_3$ with the notation of the main interband transitions, which contribute to the polarization function in RPA: O(2p) → V(e_g) (1), O(2p) → V (t_{2g}) (2), and V (t_{2g}) → V (e_g) (3). The right panel shows the intraorbital Coulomb interaction $\mathcal{U}$ as obtained in the constrained DFT (denoted as 'c') and after including the screening caused by different interband transitions in RPA. The RPA results show the screening corresponding to each type of transition in the polarization function as well as the final value of $\mathcal{U}$, which incorporates the effect of all three transitions [22].

In the atomic limit, all interactions between t_{2g} electrons are reduced to either $\mathcal{U}$, $\mathcal{U}'$, or $\mathcal{J}$, and there are no other types of interaction connecting the t_{2g} orbitals (see appendix A). Below we will argue that a similar property holds even after the RPA screening.

In addition to the final value of $\mathcal{U}$, figure 6 shows the screened interactions corresponding to each type of transition in the polarization function. The screening caused by the change of the hybridization is very efficient. For example, in comparison with the constrained DFT, the intraorbital interaction $\mathcal{U}$ is reduced from 11.2 to 2.5 eV (i.e., by more than a factor of four). The main contribution to this screening comes from the oxygen 2p → vanadium e_g and oxygen 2p → vanadium t_{2g} interband transitions in the polarization functions. Since the hybridization between vanadium t_{2g} and e_g orbitals is small in perovskite compounds with the simple cubic structure, the screening associated with the transitions between vanadium t_{2g} and e_g bands is also small.

The dependence of the screened Coulomb interactions on the number of electrons, $n_{t_{2g}}$, accommodated in the t_{2g} band is shown in figure 7 [22]. The calculations have been performed in the rigid-band approximation and using the electronic structure of $SrVO_3$. Such an analysis may be useful for understanding the doping dependence of the effective Coulomb interactions.

The Coulomb interactions reveal a monotonic behavior as the function of doping. The screening is most efficient when the whole t_{2g} band is empty ($n_{t_{2g}} = 0$). The situation corresponds to $SrTiO_3$, where all transitions from the oxygen 2p to the transition-metal t_{2g} band can contribute to the screening (see figure 6). This channel of screening is closed when the t_{2g} band is filled ($n_{t_{2g}} = 6$). In the latter case, only the oxygen 2p → transition-metal e_g interband transitions may contribute to the screening. Hence, the effective Coulomb interaction becomes large.

The screening of the exchange integral $\mathcal{J}$ is practically independent of the doping. The Kanamori rule, $\mathcal{U} = \mathcal{U}' + 2\mathcal{J}$, which was originally established for the spherical environment in isolated atoms, works well also for the t_{2g} manifold in cubic

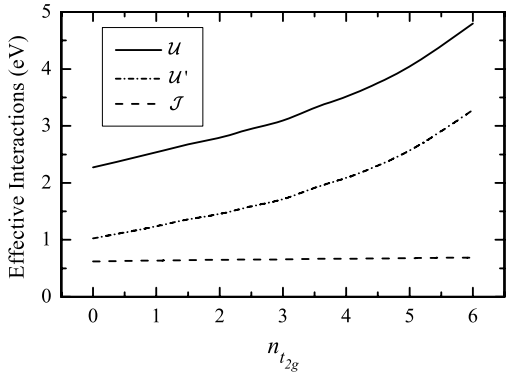

Figure 7. Doping dependence of Kanamori parameters in $SrVO_3$ [22]: the intraorbital Coulomb interaction $\mathcal{U}$, the interorbital Coulomb interaction $\mathcal{U}'$, and the exchange interaction $\mathcal{J}$ versus the number of electrons in the t_{2g} band, $n_{t_{2g}}$.

compounds, even after the screening of t_{2g} interactions by other electrons.

This result supports an old empirical rule suggesting that only the Coulomb integral $\mathcal{U}$ is sensitive to the crystal environment in solids. The nonspherical interactions, which are also responsible for Hund's first and second rules, appear to be much closer to their atomic values and practically insensitive to the screening [72–74].

It is important to note that the values obtained for effective Coulomb interactions are substantially smaller than the experimental parameters derived from the analysis of photoemission spectra [75, 76]. However, this is to be expected. Note that the photoemission spectra are typically interpreted in the cluster model, which treats *explicitly* all transition-metal 3d as well as the oxygen 2p states. However, in the model (3) we would like to keep only the transition-metal t_{2g} bands and include the effect of other bands *implicitly*, i.e. through the renormalization of interaction parameters in the t_{2g} band. Therefore, our parameters should be generally smaller in comparison with the ones derived from the cluster model. As was discussed above, the transfer of an electron,

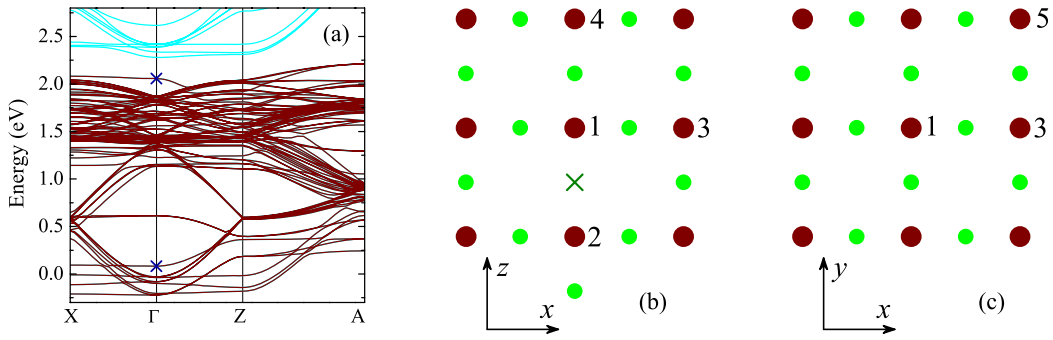

Figure 8. Left panel: LDA band structure of supercell $Sr_{27}Ti_{27}O_{80}$ corresponding to the oxygen-deficient $SrTiO_{2.963}$. The (dark) brown curves show 83 bands located near the Fermi level and formed by $3 \times 27 = 81$ t_{2g} Wannier orbitals of all 27 Ti atoms as well as the z^2 orbitals of two Ti atoms located near the oxygen vacancy (denoted as '1' and '2' in the right panel). The position of these z^2 bands in the Γ-point are marked by the crosses. Right panel: the atomic positions around the oxygen vacancy, namely, in the yz plane, which contains the vacancy (b), and in the xy plane, which is located just above the vacancy (c). The Ti atoms are indicated by the big dark (brown) spheres, the oxygen atoms are indicated by the small light gray (green) spheres, and the oxygen vacancy is indicated the symbol ×.

associated with the reaction $(n_{\mathbf{R}\alpha}, n_{\mathbf{R}'\beta}) \rightleftharpoons (n_{\mathbf{R}\alpha}+1, n_{\mathbf{R}'\beta}-1)$ will cause some change of the electronic structure in the region of oxygen 2p and transition-metal e_g bands, which tends to compensate the change of the number of the 3d electrons in the t_{2g} band. Since the oxygen 2p and transition-metal e_g bands are eliminated in our t_{2g} model, this change of the electronic structure is effectively included in the screening of Coulomb interactions in the t_{2g} band, which naturally explains smaller values of the parameter $\mathcal{U}$.

Finally, the value obtained in [22] for the intraorbital Coulomb interaction $\mathcal{U} = 2.53$ eV is substantially smaller than $\mathcal{U} \approx 5.55$ eV, which is typically used in DMFT calculations to reproduce the experimental photoemission spectra [77]. Recent full-potential RPA calculations based on the maximally localized Wannier functions yielded $\mathcal{U} = 3.0$ eV [78], which basically supports the result of [22], but is too small to explain the photoemission spectra in terms of conventional DMFT for the t_{2g} band. This maybe a serious problem indicating that something is missing in the current interpretation of the photoemission data. Some of the missing ingredients may be the spacial correlations, the explicit contribution of the oxygen states, or the frequency dependence of the effective Coulomb interaction in RPA [39]. On the other hand, the value obtained for the exchange interaction $\mathcal{J} = 0.64$ eV is very close to $\mathcal{J} = 0.68$ eV, which is typically used in the analysis of the photoemission spectra [76].

6.2. *Inversion-symmetry breaking and 'forbidden' hoppings*

In this small section we would like to consider two examples of deviation from the ideal bulk structure of perovskites, which are related to violation of the inversion symmetry around transition-metal sites. One is the oxygen vacancy, and the other one is the (001) surface of $SrTiO_3$. Particularly, we will argue that such an inversion-symmetry breaking may lead to a number of new effects, and qualitatively change the character of transfer integrals between Wannier functions.

6.2.1. Oxygen vacancy in $SrTiO_3$. In cubic perovskites, such as $SrTiO_3$, the oxygen vacancy creates a dimer of Ti atoms located in its first coordination sphere. It also donates two electrons to the t_{2g} band[24].

In order to study the effect of the oxygen vacancy on the electronic structure of $SrTiO_3$ we have used a $3 \times 3 \times 3$ supercell, in which one of the oxygen atoms has been replaced by an empty sphere. Such a composition corresponds to the chemical formula $SrTiO_{2.963}$. No lattice relaxation has been considered at this stage. According to LDA calculations, the electronic structure of such a supercell near the Fermi level is formed by 83 bands, which are well isolated from the rest of the spectrum (figure 8). Among them, $3 \times 27 = 81$ bands are the regular t_{2g} bands, whereas two additional bands are formed predominantly by z^2 orbitals of two Ti atoms located near the oxygen vacancy. The t_{2g} and z^2 bands are strongly mixed.

Therefore, it is clear that the minimal model near the Fermi level should be constructed in the basis of four Wannier orbitals (nominally, z^2, xy, yz, and zx) of two Ti atoms located near the vacancy, and three Wannier orbitals (nominally, xy, yz, and zx) of all remaining Ti atoms located in the next coordination spheres. The atomic wavefunctions of these types can be used as the trial functions in the downfolding method. The behavior of transfer integrals and the crystal-field splitting obtained after the downfolding is explained in table 2. There are a number of interesting effects related to the presence of the oxygen vacancy.

(i) The oxygen vacancy breaks the cubic symmetry and splits the t_{2g} levels of two Ti atoms located next to it. The splitting is about 270 meV. However, already in the next coordination sphere, the t_{2g}-level splitting is greatly reduced[25], and the situation becomes close to the perfect cubic environment. On the other hand, the position of the impurity z^2 level is lowered due to the missing Ti–O bond. As a result, the z^2 levels become close to the t_{2g} ones[26].

[24] Under certain conditions, such a situation may lead to the formation of the spin-singlet bipolaronic state [79].

[25] For example, for the titanium atoms 3 and 4 depicted in figure 8, the t_{2g}-level splitting is only 37 and 40 meV, respectively.

[26] Note that the impurity z^2 level is an antibonding combination of the atomic oxygen 2p and titanium $3z^2$ orbitals. Therefore, the lack of one of the Ti–O bond formed by the Ti atom near the vacancy will shift the z^2 level to the low-energy region.

Table 2. Crystal-field splitting (1–1) and transfer integrals in the bonds 1–2, 1–3, 1–4, and 1–5 around the oxygen vacancy in $SrTiO_3$. All energies are measured in meV. The atomic positions are explained in figure 8.

	1–1				1–2			
	z^2	xy	yz	zx	z^2	xy	yz	zx
z^2	164	0	0	0	−709	0	0	0
xy	0	124	0	0	0	−25	0	0
yz	0	0	−144	0	0	0	37	0
zx	0	0	0	−144	0	0	0	37

	1–3			1–4			1–5		
	xy	yz	zx	xy	yz	zx	xy	yz	zx
z^2	0	0	−145	0	0	0	−24	7	7
xy	−224	0	0	−28	0	0	−82	0	0
yz	−9	−22	0	0	−219	0	5	−1	7
zx	0	0	−269	0	0	−219	5	7	−1

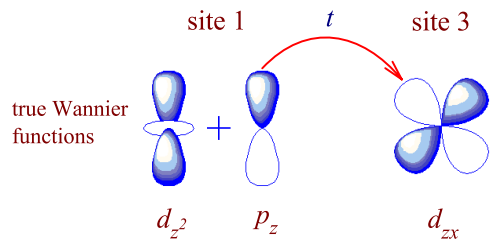

Figure 9. Cartoon picture explaining the appearance of the 'forbidden hoppings' near the points of the inversion-symmetry breaking. The notation of the atomic sites are explained in figure 8. Due to the local inversion-symmetry breaking (or the parity violation), the atomic orbital d_{z^2} at the site 1 is allowed to mix with the atomic orbital p_z, belonging to the same site. The combination of these orbitals will form a true Wannier function, centered at the site 1. Then, the electron can transfer from the p_z orbital of the site 1 to the d_{zx} orbital of the site 3 (and vice versa).

For example, the crystal-field splitting between the z^2 and xy levels is only 40 meV.[27]

(ii) The behavior of transfer integrals across the vacancy (the bond 1–2) is fundamentally different from the conventional case, when they are mediated by the oxygen 2p states (for example, in the bond 1–4): the transfer integrals between all three t_{2g} orbitals are negligibly small, while the main interaction occurs between z^2 orbitals.

(iii) The lack of inversion symmetry leads to the mixing of the atomic 3d and 4p orbitals at the same Ti site. For example, the Wannier function, which is nominally denoted as z^2, besides the conventional $3d_{z^2}$ atomic orbitals will have some weight of the $4p_z$ orbitals. Since the 4p orbitals are rather extended in the real space, such a mixing may change the form of the transfer integrals and even lead to the appearance of new interactions. The most striking example is the large transfer integral occurring between neighboring z^2 and zx Wanner orbitals in the bond 1–3 near the vacancy (figure 9). Such an interaction would vanish in the perfect cubic environment.

[27] For comparison, the t_{2g}–e_g splitting in the perfect perovskites is about 3 eV (figures 1 and 3).

Table 3. Intraorbital Coulomb interactions associated with different Ti sites around the oxygen vacancy in $SrTiO_3$. All energies are measured in eV. The atomic positions are explained in figure 8.

Orbital	Site 1	Site 3	Site 4	Site 5
xy	2.61	2.72	2.71	2.70
yz	2.57	2.71	2.77	2.70
zx	2.57	2.75	2.77	2.70
z^2	2.67	—	—	—

The distortion of the perfect cubic environment by the oxygen vacancy will affect not only the one-electron part of the model Hamiltonian (3), but also the Coulomb interactions (table 3). For example, around the vacancy, the Coulomb interactions associated with different t_{2g} orbitals are clearly different. This effect is captured by the RPA screening. The cubic symmetry of Coulomb interactions is practically restored in the fourth coordination sphere (site 5 in figure 8).

6.2.2. Surface states in $SrTiO_3$. Another example of the inversion-symmetry breaking is the TiO_2 terminated surface of $SrTiO_3$. The surface states have been studied in the slab geometry. Each slab contained nine TiO_2 layers, which were separated by the SrO layers. Hence, the chemical formula of the slab was $(TiO_2)_9(SrO)_8$.[28] According to the adopted notation, the first TiO_2 layer corresponds to the surface, while the fifth TiO_2 layer corresponds to the bulk of $SrTiO_3$ (figure 10). No lattice relaxation has been considered at this stage.

The electronic structure of $(TiO_2)_9(SrO)_8$ near the Fermi level consists of the $3 \times 9 = 27$ t_{2g} bands and two z^2 bands, which are mainly formed by the surface TiO_2 layers. Therefore, the minimal model can be constructed in the Wannier basis of (nominally) z^2, xy, yz, and zx orbitals centered at the surface Ti sites and the xy, yz, and zx orbitals representing the remaining ('bulk') sites. Thus, there is a direct analogy with the case of the oxygen vacancy in $SrTiO_3$. In both cases, the Ti atoms located next to the 'defect' (the surface, in the present case) acquire an additional z^2 orbital, whereas other Ti sites are described in the standard t_{2g} basis.

The one-electron part of the model Hamiltonian is explained in table 4. At the surface, there is a huge crystal-field splitting, which even exceeds the one near the single oxygen vacancy. Due to the inversion-symmetry breaking, there is an appreciable 'forbidden' hopping between the z^2 and zx Wannier orbitals operating in the surface bond 1–1′. The transfer integrals operating between t_{2g} orbitals near the surface (the bonds 1–1′ and 1–2) are also different from the ones in the bulk (the bond 5–5′). Thus, the effect of the surface on the electronic structure of the transition-metal perovskite oxides is not only in the narrowing of the yz and zx bands, caused by

[28] The considered geometry can been obtained from the bulk $SrTiO_3$ by cutting the slab $(TiO_2)_9(SrO)_8$ and replacing the next $(TiO_2)_2(SrO)_3$ layers by empty spheres. The considered region of empty spheres was sufficient to make the interaction between different slabs negligibly small.

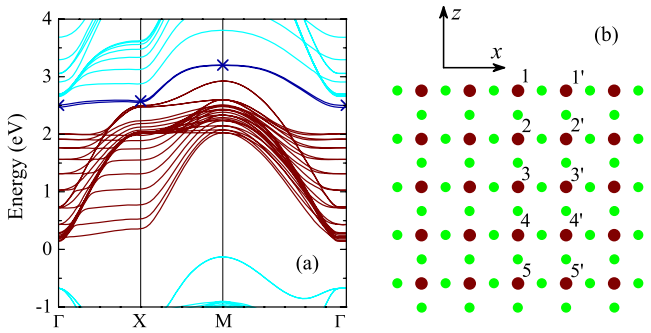

Figure 10. Left panel: LDA band structure of the slab $(TiO_2)_9(SrO)_8$. The (dark) brown curves are the t_{2g} bands. The 'surface' z^2 bands are depicted by the symbols $\times$. Right panel: the atomic positions near the (TiO_2)-terminated surface of $SrTiO_3$. The Ti atoms are indicated by the big dark (brown) spheres, and the oxygen atoms are indicated by the small light gray (green) spheres.

Table 4. Crystal-field splitting (1–1) and transfer integrals at the surface and in the bulk of $SrTiO_3$. All energies are measured in meV. The atomic positions are explained in figure 10.

	1–1				1–1′			
	z^2	xy	yz	zx	z^2	xy	yz	zx
z^2	617	0	0	0	−97	0	0	−80
xy	0	18	0	0	0	−234	−10	0
yz	0	0	−317	0	0	10	−19	0
zx	0	0	0	−317	80	0	0	−325

	1–2			5–5′		
	xy	yz	zx	xy	yz	zx
xy	−29	0	0	−234	0	0
yz	0	−207	0	0	−30	0
zx	0	0	−207	0	0	−234

the reduced number of bonds available for the hoppings [63][29]. Even more serious consequences can be caused by the crystal-field splitting and the 'forbidden hoppings'[30].

The Coulomb interactions at the surface of $SrTiO_3$ are also considerably distorted in comparison with the bulk (table 5). However, the bulk-like behavior is practically restored in the second TiO_2 layer. Similar to the single oxygen vacancy, the surface breaks the cubic symmetry of the Coulomb interactions. Moreover, the Coulomb interactions between t_{2g} orbitals are somewhat smaller at the surface of $SrTiO_3$ than in the bulk. As in the case of the single oxygen vacancy, this dependence of the effective Coulomb interactions on the local environment of the transition-metal sites is captured by the RPA screening.

[29] Note that the orbital zx is perpendicular to the surface. Therefore, it can be involved in the hoppings in the directions $\pm x$ and $-z$ (in the geometry shown in figure 10). Similar situation holds for the yz orbitals. On the contrary, the xy orbital is involved in the hoppings in all four directions $\pm x$ and $\pm y$.

[30] Note that in addition to the hopping, the z^2 and zx orbitals are coupled at the same transition-metal site by the spin–orbit interactions. If the surface were magnetic, this type of coupling would lead to the Dzyaloshinsky–Moriya interactions between the spins [80, 81]. Thus, the 'forbidden hoppings' provide a microscopic basis for the appearance of these interactions.

Table 5. Intraorbital Coulomb interactions associated with different Ti sites in the slab $(TiO_2)_9(SrO)_8$. All energies are measured in eV. The atomic positions are explained in figure 10.

Orbital	Site 1	Site 2	Site 3	Site 4	Site 5
xy	2.43	2.65	2.66	2.65	2.65
yz	2.52	2.64	2.65	2.65	2.65
z^2	2.69	—	—	—	—

6.3. Distorted perovskite oxides

The transition-metal perovskite oxides ABO_3 (where A = Y or La, and B = Ti or V) are regarded as some of the key materials for understanding the strong coupling among spin, orbital, and lattice degrees of freedom in correlated electron systems [4, 82].

All the compounds have a distorted perovskite structure. The distortion can be either orthorhombic ($LaTiO_3$, $YTiO_3$, and YVO_3 below 77 K) or monoclinic ($LaVO_3$ and YVO_3 above 77 K). The space group of the orthorhombic phase is D_{2h}^{16} (in Schönflies notations or *Pbnm* in the Hermann-Maguin notations, No. 62 in the International Tables). The space group of the monoclinic phase is C_{2h}^5 ($P2_1/a$, No. 14 in the International Tables)[31]. The magnitude of the distortion is controlled by the size of the A^{3+} ions. Typically, the smaller the size of the A^{3+} ions, the larger the distortion. For example, the YBO_3 oxides are always more distorted than the $LaBO_3$ oxides[32].

According to electronic structure calculations in the local-density approximation, all compounds have a common transition-metal t_{2g} band, located near the Fermi level and well isolated from the rest of the spectrum (figure 1). The number of electrons donated by each transition-metal site to the t_{2g} band is one and two for $ATiO_3$ and AVO_3, respectively. These electrons are subjected to strong Coulomb correlations, beyond the local-density approximation, and the systems are classified as Mott insulators [4].

Furthermore, the Coulomb correlations interplay with the lattice distortions, leading to a peculiar phase diagram, where each compound has a distinct magnetic structure (figure 11). For example, $YTiO_3$ is a ferromagnet [85–88]. $LaTiO_3$ is a three-dimensional (G-type) antiferromagnet [84, 89]. At low temperature, YVO_3 has G-type antiferromagnetic structure, which transforms to a chain-like (C-type) antiferromagnetic structure at around 77 K [83, 90–92]. The magnetic transition coincides with the structural orthorhombic-to-monoclinic transition. On the other hand, $LaVO_3$ is a C-type antiferromagnet in the whole temperature range below the magnetic transition point [93, 94]. The understanding of these magnetic properties will be the main goal of this section.

It is worth noticing that on the theoretical side the magnetic behavior of these 't_{2g}' compounds has been and continues to be the subject of numerous controversies. So far, the theoretical interpretation of the unusual magnetic properties has been based on two different standpoints, which

[31] There are certain indications that the actual symmetry can be even lower than $P2_1/a$ [83].

[32] For example, the Ti–O–Ti angle is 157°–158° in $LaTiO_3$ [84], and only 140°–144° in $YTiO_3$ [85].

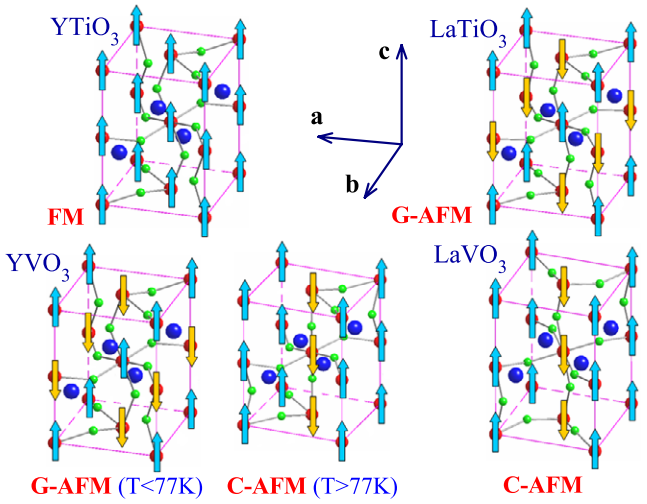

Figure 11. Crystal and magnetic structure of distorted perovskite oxides. The La and Y atoms are indicated by the big (blue) dark spheres, the Ti and V atoms are indicated by the medium (red) dark gray spheres, and the oxygen atoms are indicated by the small (green) light gray spheres. The vectors **a**, **b**, and **c** show the directions of orthorhombic translations. The directions of the magnetic moments are shown by arrows.

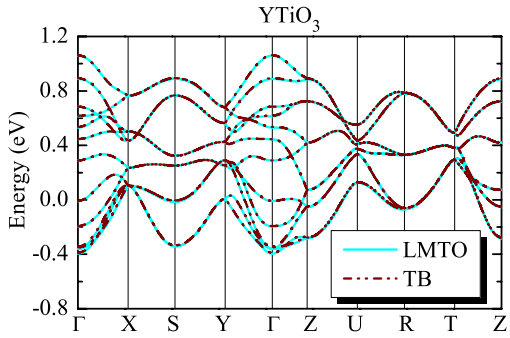

Figure 12. LDA bands for $YTiO_3$ as obtained in the original electronic structure calculations using the LMTO method and after the tight-binding (TB) parametrization using the downfolding method [22]. Notation of the high-symmetry points of the Brillouin zone is taken from [65].

practically exclude each other. One is the picture of an orbital liquid, which implies that the effect of the crystal distortion on the electronic structure is small and the (quasi-) degeneracy of the atomic t_{2g} levels is preserved even in the real crystal environment [95, 96]. Another one is the theory of crystal field, which lifts the orbital degeneracy and stabilizes certain orbital structures compatible with the observed magnetic ground state [25, 97, 98].

6.3.1. Results of downfolding for the one-electron part and Wannier functions. An example of the electronic structure in the region of the t_{2g} bands for $YTiO_3$ is shown in figure 12. It reveals an excellent agreement between the results of the original LMTO calculations and their tight-binding parametrization obtained in the downfolding method. Since cubic t_{2g} and e_g orbitals are mixed by the crystal distortion, the trial functions $\{\tilde{\chi}^t_{\mathbf{R}}\}$ of the downfolding method can no longer be chosen from geometrical considerations. Generally, such a choice is not unique. Nevertheless, for these purposes one can use the eigenvectors obtained from the diagonalization of the density matrix. As was already pointed out in section 3.3, such a procedure should guarantee a good degree of localization of the Wannier functions as well as of the parameters of the model Hamiltonian in the real space.

The spacial extension of the Wannier functions constructed for $YTiO_3$ and $LaTiO_3$ is illustrated in figure 13. In $LaTiO_3$, about 80–85% of the total weight of the Wannier function is accumulated at the central Ti site, 5–9% belongs to six oxygen sites surrounding the central Ti atom, and about 10% is distributed over La, Ti, and O sites located in next coordination spheres. In $YTiO_3$, the same distribution parameters are 82–87%, 6–10%, and 5%, correspondingly for the central Ti site, its neighboring oxygen sites, and Y, Ti, and O sites located in the next coordination spheres. Another measure of localization is the expectation value of the square of the position operator: $\langle \mathbf{r}^2 \rangle_\alpha = \langle \tilde{W}^\alpha_{\mathbf{R}} | (\mathbf{r} - \mathbf{R})^2 | \tilde{W}^\alpha_{\mathbf{R}} \rangle$ [16], which yields $\langle \mathbf{r}^2 \rangle_\alpha = 2.68$, 2.36, and 2.37 Å^2 for $LaTiO_3$, and $\langle \mathbf{r}^2 \rangle_\alpha = 2.28$, 1.90, and 2.05 Å^2 for $YTiO_3$. Thus, the Wannier functions for $LaTiO_3$ and $SrVO_3$ are less localized in comparison with the more distorted $YTiO_3$. However, this is to be expected. One reason is the lattice distortion, which increases in the direction $SrVO_3 \rightarrow LaTiO_3 \rightarrow YTiO_3$. Another reason is the proximity of transition-metal t_{2g} and oxygen 2p bands[33]. The degree of the localization in $SrVO_3$ and $LaTiO_3$ is very similar, despite the distortion which takes place in $LaTiO_3$. One reason may be the proximity of the lanthanum 5d states to the Fermi level, which leads to stronger hybridization with the transition-metal t_{2g} states [5, 99].

6.3.2. Transfer integrals and crystal-field splitting. The behavior of the parameters of the one-electron part of the model Hamiltonian is explained in figure 14. Because of the lattice distortion, there is an appreciable crystal-field splitting, which is larger for the more distorted $YTiO_3$ and YVO_3, and substantially smaller for the least distorted $LaTiO_3$. Furthermore, there is a clear correlation between the number of t_{2g} electrons and the form of the crystal-field splitting. As the rule, the crystal-field splitting tends to quench the orbital degrees of freedom. For example, in $YTiO_3$, it splits off one t_{2g} level to the low-energy part of the spectrum, that is just enough to accommodate one t_{2g} electron. The gap separating the lowest t_{2g} level from the middle one is about 109 meV. On the contrary, the crystal-field splitting in YVO_3 simultaneously lowers the energies of two t_{2g} levels; this is again consistent with the number of t_{2g} electrons per vanadium site. The distance between the middle and highest t_{2g} levels in the orthorhombic phase of YVO_3 is about 111 meV.

The monoclinic distortion in YVO_3 and $LaVO_3$ creates two inequivalent types of vanadium atoms, which lie in

[33] For example, the distance between the transition-metal t_{2g} and oxygen 2p bands is 3.2 eV in $YTiO_3$, 2.7 eV in $LaTiO_3$, and only 0.3 eV in $SrVO_3$. Therefore in $SrVO_3$, the mixing between the t_{2g} and 2p states is stronger, and the Wannier functions have a larger weight at the oxygen sites. To smaller extent the same is true for $LaTiO_3$ (in comparison with $YTiO_3$).

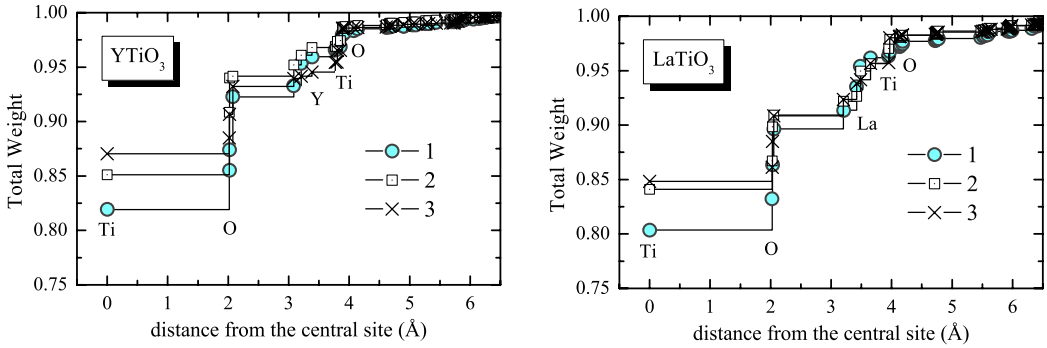

Figure 13. Spacial extension of Wannier functions for $YTiO_3$ (left) and $LaTiO_3$ (right). The figure shows the total weight of the Wannier function accumulated around the central Ti site after adding every new sphere of neighboring atomic sites. The symbols '1', '2', and '3' denote the Wannier functions obtained after projection onto the eigenvectors of the density matrix, where '1', '2', and '3' correspond to the largest, second largest, and third largest eigenvalues, respectively.

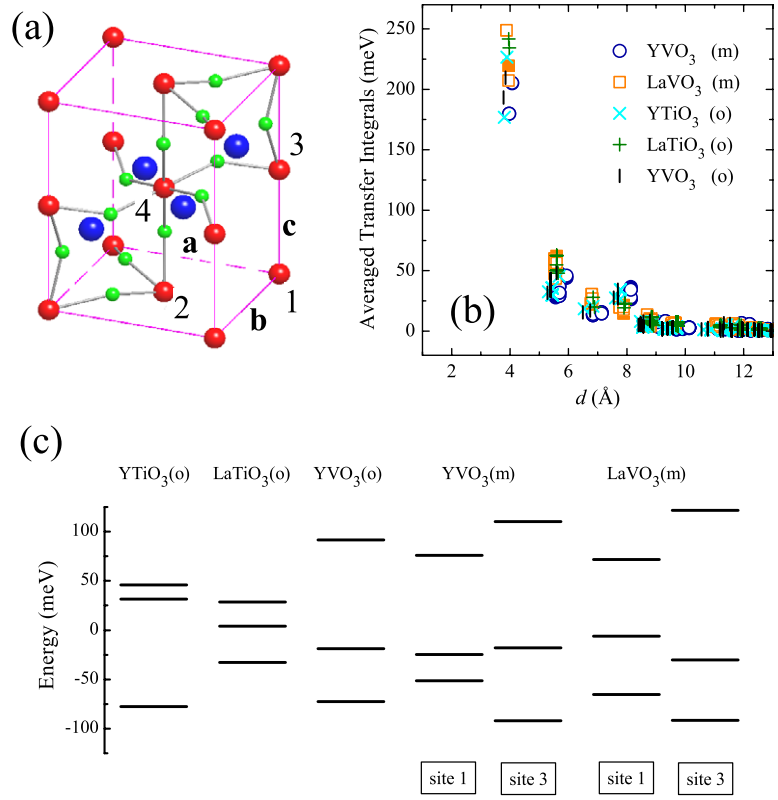

Figure 14. (a) Crystal structure of the distorted perovskite oxides with the notation of the positions of four transition-metal sites in the unit cell. In orthorhombic compounds all sites are equivalent and can be transformed to each other by the symmetry operations of the D_{2h}^{16} group. In monoclinic compounds, there are two inequivalent pairs of transition-metal sites: (1, 2) and (3, 4). (b) Distance dependence of averaged transfer integrals. In the orthorhombic (o) structure, all sublattices are equivalent and shown by a single symbol. In the monoclinic (m) structure, the transfer integrals around two inequivalent transition-metal sites are shown by closed and open symbols. (c) t_{2g}-level splitting. The notations 'site 1' and 'site 3' stand for two nonequivalent transition-metal sites in the monoclinic structure [5].

different **ab**-planes and are denoted as (1, 2) and (3, 4) in figure 14. Typically, the less distorted planes (1, 2) are alternated with the more distorted planes (3, 4). The magnitude of the crystal-field splitting depends on the compound. For example, in YVO_3, the energy splitting between middle and highest t_{2g} levels in the planes (1, 2) and (3, 4) is fairly similar: 101 meV and 128 meV, respectively. However, in $LaVO_3$, the plane (1, 2) appears to be much less distorted in comparison with the plane (3, 4), resulting in different crystal-field splittings: 78 meV and 152 meV, respectively. Not only the energies, but also the directions of the crystal-field splitting are different in the orthorhombic and monoclinic phases which immediately follows from the symmetry considerations[34].

[34] For example, in the orthorhombic phase, the sites 1 and 3 (figure 14) can be transformed to each other by 180° rotations around the **c** axis associated with the translation by **c**/2. In the monoclinic phase, such a symmetry operation is no longer available.

In section 6.3.4, we will argue that such a difference is directly related to the type of the orbital ordering, which is reflected in the magnetic properties of the distorted perovskite oxides. It is important to note that nonsphericity of the Madelung potential (17) is crucial for reproducing the correct magnetic ground state of YVO_3 and $LaVO_3$, contrary to the conventional atomic-spheres approximation [5].

Because of the complexity of transfer integrals in the distorted perovskite structure, it is practically impossible to discuss the behavior of individual matrix elements of $\|h^{\alpha\beta}_{\mathbf{RR}'}\|$. Nevertheless, some useful information can be obtained from the analysis of *averaged* parameters

$$\bar{h}_{\mathbf{RR}'}(d) = \left(\sum_{\alpha\beta} h^{\alpha\beta}_{\mathbf{RR}'} h^{\beta\alpha}_{\mathbf{R}'\mathbf{R}} \right)^{1/2},$$

where d is the distance between transition-metal sites $\mathbf{R}$ and $\mathbf{R}'$. All transfer integrals are well localized and practically restricted by the nearest neighbors, located at around 4 Å (figure 14(b)). As expected, the transfer integrals between the nearest neighbors are generally larger for the less distorted $LaTiO_3$ and $LaVO_3$, and smaller for the more distorted $YTiO_3$ and YVO_3.

6.3.3. Effective interactions. Matrix elements of the effective Coulomb interaction in the t_{2g} band can be computed by applying the combined constrained DFT plus RPA approach, which has been explained in detail in section 4. At each transition-metal site, it yields the $3 \times 3 \times 3 \times 3$ $\hat{U}$-matrix of screened Coulomb interactions in the basis of Wannier orbitals. The inter-site interactions are considerably smaller and can be neglected [22]. For explanatory purposes, the $\hat{U}$-matrix can be fit in terms of two Kanamori parameters: the intraorbital Coulomb interaction $\mathcal{U}$ and the intra-atomic exchange interaction $\mathcal{J}$ [60]. The results of such fitting are shown in table 6. There is a certain dependence of the parameter $\mathcal{U}$ on the local environment in solid, which is captured by RPA calculations [22]. For example, the value of $\mathcal{U}$ appears to be larger for the more distorted YBO_3 compounds. There is also a clear correlation between the value of $\mathcal{U}$ and the magnitude of the local distortion around two inequivalent transition-metal sites in the monoclinic structure: the sites

Table 6. Results of fitting the effective Coulomb interactions for the distorted perovskite oxides in terms of two Kanamori parameters: the intraorbital Coulomb interaction $\mathcal{U}$ and the exchange interaction $\mathcal{J}$ [5]. All energies are measured in eV. The symbols 'o' and 'm' stand for the orthorhombic and monoclinic phase, respectively. The positions of the transition-metal sites are explained in figure 14. Generally, the site '1' is located in a less distorted environment while the site '3' is located in more distorted environment.

Compound	Phase	Site	$\mathcal{U}$	$\mathcal{J}$
$YTiO_3$	o	1	3.45	0.62
$LaTiO_3$	o	1	3.20	0.61
YVO_3	o	1	3.27	0.63
YVO_3	m	1	3.19	0.63
		3	3.26	0.63
$LaVO_3$	m	1	3.11	0.62
		3	3.12	0.62

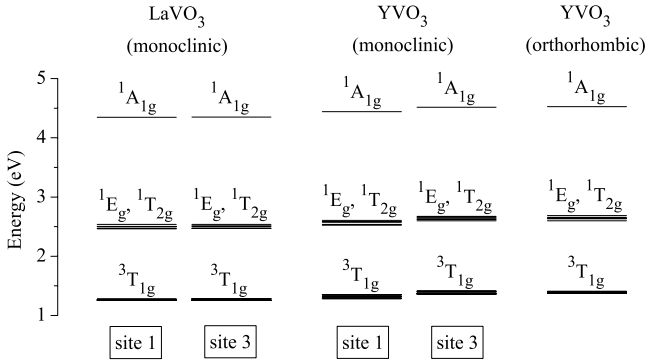

Figure 15. Atomic multiplet structure of two interacting t_{2g} electrons in the 'ground state' of vanadates. The positions of the transition-metal sites in the monoclinic structure are explained in figure 14. Generally, the sites '1' are located in a less distorted environment, while the sites '3' are located in a more distorted environment.

experiencing larger distortion (according to the magnitude of the crystal-field splitting in figure 14(c)) have larger $\mathcal{U}$, and vice versa. On the other hand, the exchange interaction $\mathcal{J}$ is less sensitive to the local environment in solids.

Some of these trends can be rationalized by considering some additional approximations for the screening of Coulomb interactions in the t_{2g} band by the oxygen 2p band (appendix B). Nevertheless, we would like to emphasize that it is quite possible that these arguments are applicable only for this particular class of compounds. In other systems, other channels of screening may prevail and the situation can be generally different.

Thus, even the effective Coulomb interaction in the t_{2g} band can be affected by the crystal distortion, and this effect is clearly captured by realistic calculations of the model parameters. Besides two Kanamori parameters, $\mathcal{U}$ and $\mathcal{J}$, the crystal distortion affects the fine structure of the entire $\hat{U}$-matrix and may even change its symmetry. Generally, such a symmetry is no longer cubic. This effect is clearly seen in the atomic multiplet structure, corresponding to two interacting t_{2g} electrons in the case of vanadates: because of the crystal distortions the levels $^3T_{1g}$, ^1E_g, and $^1T_{2g}$ are slightly split (figure 15). The effect is not particularly strong. However, it can probably contribute to some delicate magnetic properties of the distorted perovskite oxides, such as the orbital magnetization, magnetocrystalline anisotropy, Dzyaloshinsky–Moriya interactions, etc.

Finally, it is important to note that the obtained parameters of on-site interactions are substantially smaller than the value of the Coulomb integral $\mathcal{U} \sim 5$ eV derived from the photoemission data [76], which is typically used in calculations based on the dynamical mean-field theory [99–101]. As was already pointed out in section 6.1.2, the reason for such a difference is rather transparent and related to the additional screening coming from the oxygen 2p as well as the transition-metal e_g bands, which are not explicitly included in the low-energy model (3). The application of the dynamical mean-field theory with the parameters reported in table 6 would apparently lead to a metallic behavior for all the considered

compounds [99], being in stark contrast with the experimental data. Apparently, this contradiction can be resolved by going beyond the single-site approximation and considering the spacial correlations [52].

6.3.4. Orbital ordering and magnetic properties. It is convenient to start the discussion with the low-temperature orthorhombic phase of YVO_3, which is one of the most distorted systems among the ones considered. The distribution of the t_{2g} electron density around the vanadium sites (the so-called orbital ordering) obtained in the Hartree–Fock calculations is shown in figure 16. The type of the orbital ordering can be identified as 'C', meaning that the orientation of the orbital clouds relative to each other is nearly orthogonal in the **ab** plane, and nearly parallel along the **c** axis, i.e. in close analogy with the C-type antiferromagnetic spin ordering (figure 11).

The orbital ordering is very robust, and practically independent of the type of the magnetic arrangement. This means that the orbital degrees of freedom are quenched by the crystal-field splitting and the superexchange processes, which may adjust the orbital ordering in order to minimize the total energy of the system [10], are considerably weaker.

Generally, the orbital ordering of the C-type is compatible with the G-type antiferromagnetic spin ordering [76, 102, 103]. Therefore, it is not surprising that the experimentally observed G-type antiferromagnetic ground state of orthorhombic YVO_3 is already reproduced at the level of mean-field Hartree–Fock calculations (table 7). The conclusion is totally consistent with

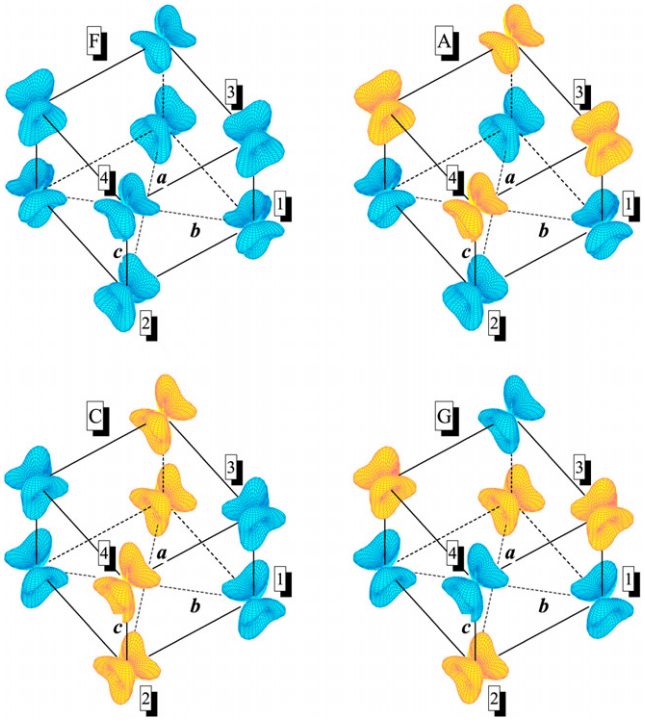

Figure 16. Distribution of the electron density around vanadium sites as obtained in the Hartree–Fock calculations for the ferromagnetic (F) and A-, C-, and G-type antiferromagnetic alignment in the orthorhombic phase of YVO_3 ($T < 77$ K) [5]. Different magnetic sublattices are shown by different colors.

Table 7. Total energies of ABO_3 compounds in the ferromagnetic (F) and A-, C-, and G-type antiferromagnetic states measured in meV per one formula unit relative to the most stable state (marked by the symbol ×) as obtained in the Hartree–Fock calculations and after taking into account the correlation energy in the second-order perturbation theory (shown in the parenthesis). The correlation energy includes both on-site and inter-site contributions. The symbols 'o' and 'm' stand for the orthorhombic and monoclinic phases, respectively.

Compound	Phase	F-state	A-state	C-state	G-state
YVO_3	o	21.7 (26.8)	14.6 (17.2)	10.1 (11.7)	×
YVO_3	m	11.7 (17.3)	14.0 (17.0)	×	6.6 (7.2)
$LaVO_3$	m	21.0 (30.7)	20.6 (24.3)	×	7.6 (11.5)
$YTiO_3$	o	×	2.1 (0.9)	14.4 (11.3)	16.2 (12.9)
$LaTiO_3$	o	5.0 (16.9)	×	19.6 (26.5)	11.5 (11.3)

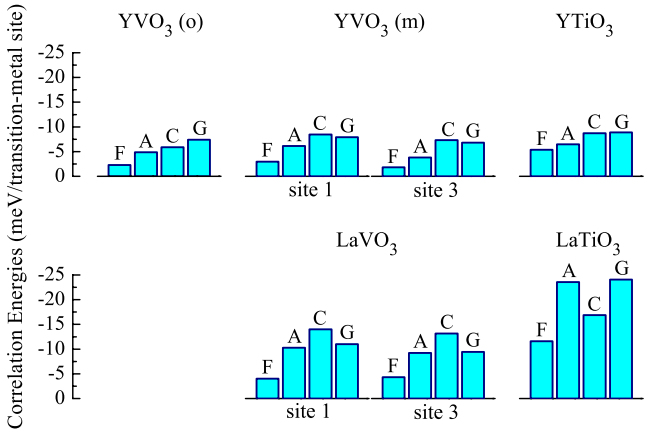

Figure 17. Correlation energies in the distorted perovskite oxides as obtained in the second-order perturbation theory starting from the Hartree–Fock ground state for the ferromagnetic (F) and A-, C-, and G-type antiferromagnetic alignment. Only on-site contributions are shown. The symbols 'o' and 'm' stand for the orthorhombic and monoclinic phases, respectively. The positions of the transition-metal sites in the monoclinic structure are explained in figure 14. Generally, the sites '1' are located in a less distorted environment, while the sites '3' are located in a more distorted environment.

results of all-electron LDA + U calculations [103, 104], and provides a transparent physical explanation for them.

The correlation effects beyond the mean-field Hartree–Fock approximation play a very important role and additionally stabilize the G-type antiferromagnetic ground state (table 7). The values of correlation energy obtained in the second-order perturbation theory are summarized in figure 17. One can clearly see that for the orthorhombic phase of YVO_3, the correlation energy is clearly the largest in the G-type antiferromagnetic state among all the magnetic structures considered.

The behavior of inter-atomic magnetic interactions has been discussed in [5]. In the case of orthorhombic YVO_3, there is a good agreement with experimental data concerning both the form (nearly isotropic three-dimensional antiferromagnetic network) and the absolute values of these interactions [88].

The transition to the higher-temperature monoclinic phase of YVO_3 is associated with an abrupt change of the orbital ordering patterns, which can be identified as the 'G-type'

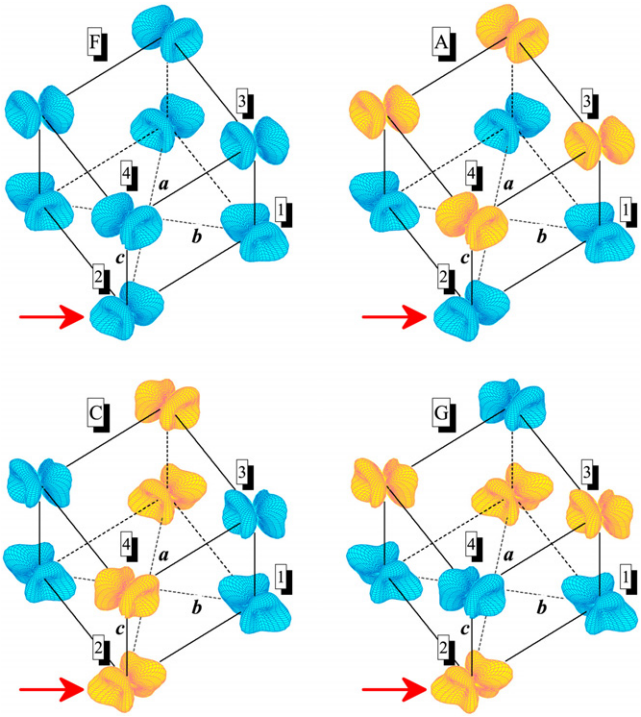

Figure 18. Distribution of the electron density around vanadium sites as obtained in the Hartree–Fock calculations for the ferromagnetic (F) and A-, C-, and G-type antiferromagnetic alignment in the monoclinic phase of YVO_3 ($T > 77$ K) [5]. Different magnetic sublattices are shown by different colors. The arrows point at the orbital clouds in the (1, 2) planes, which slightly change their shape depending on the magnetic ordering. On the contrary, the orbitals in the (3, 4) planes are well quenched by the crystal distortion.

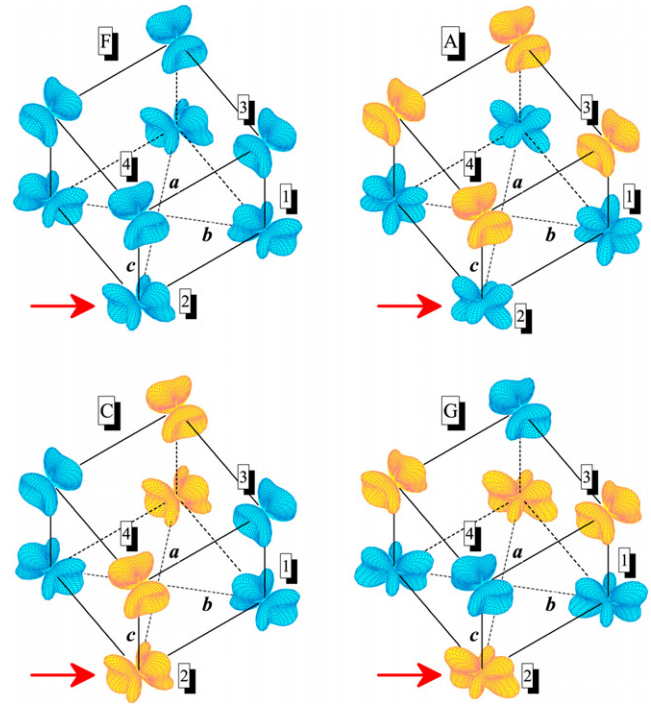

Figure 19. Distribution of the electron density around vanadium sites as obtained in the Hartree–Fock calculations for the ferromagnetic (F) and A-, C-, and G-type antiferromagnetic alignment in $LaVO_3$ [5]. Different magnetic sublattices are shown by different colors. The arrows point at the orbital clouds in the (1, 2) planes, which change their shape depending on the magnetic ordering. On the contrary, the orbitals in the (3, 4) planes are well quenched by the crystal distortion.

and corresponds to a nearly orthogonal orientation of the orbital clouds both in the **ab**-plane and along the **c** axis (figure 18). Therefore, it is reasonable to expect the emergence of the C-type antiferromagnetic structure, which is generally compatible with the orbital ordering of the G-type [102]. In this sense, there is a close analogy with the low-temperature orthorhombic phase, where the type of the magnetic ordering is strictly determined by the type of the orbital ordering. However, there is also a difference. In the monoclinic phase, there are two types of vanadium atoms, which are located in the planes (1, 2) and (3, 4), respectively. The orbital degrees of freedom in the (3, 4) plane are almost rigidly quenched by the large crystal-field splitting, similar to the orthorhombic phase. However, in the (1, 2) plane this quenching is not complete, leaving some room for the orbital fluctuations. This effect can even be seen visually in figure 18, where the shape of the orbital clouds in the (1, 2) plane slightly change depending on the magnetic state in order to additionally minimize the energy of the superexchange interactions [10].

Nevertheless, the mean-field Hartree–Fock approach appears to be a good starting point also for the monoclinic phase of YVO_3. It correctly reproduces the C-type antiferromagnetic ground state (table 7), in agreement with all-electron LDA + U calculations [104]. The correlation energy additionally stabilizes the C-type antiferromagnetic phase relative to other magnetic structures. It is also important that the orthorhombic-to-monoclinic transition in YVO_3 is well reflected in the behavior of the correlation energy, which was the largest for the G-type antiferromagnetic state in the orthorhombic phase and becomes the largest for the C-type antiferromagnetic state in the monoclinic phase (figure 17). In the monoclinic phase, there is certain dependence of the correlation energy on the local environment of the vanadium sites: generally, the site '1' with less distorted environment has larger correlation energy (and vice versa), though the effect is not particularly strong.

Similar to the monoclinic phase of YVO_3, the orbital ordering in $LaVO_3$ tends to stabilize the C-type antiferromagnetic ground state. The orbital degrees of freedom are quenched in the (3, 4) plane and retain enough flexibility in the (1, 2) plane. For example, each change of the magnetic state is accompanied by a substantial reconstruction of the orbital ordering pattern in the (1, 2) plane, which is shown by arrows in figure 19. Thus, the importance of the orbital fluctuations should rise in the direction orthorhombic YVO_3 → monoclinic YVO_3 → (monoclinic) $LaVO_3$. Apparently, the application of the mean-field Hartree–Fock theory to the latter compound is already rather critical. Nevertheless, it still provides a consistent explanation for a number of properties of $LaVO_3$. For example, the C-type antiferromagnetic ground state is successfully reproduced by the Hartree–Fock calculations and additionally stabilized by correlation effects treated in the

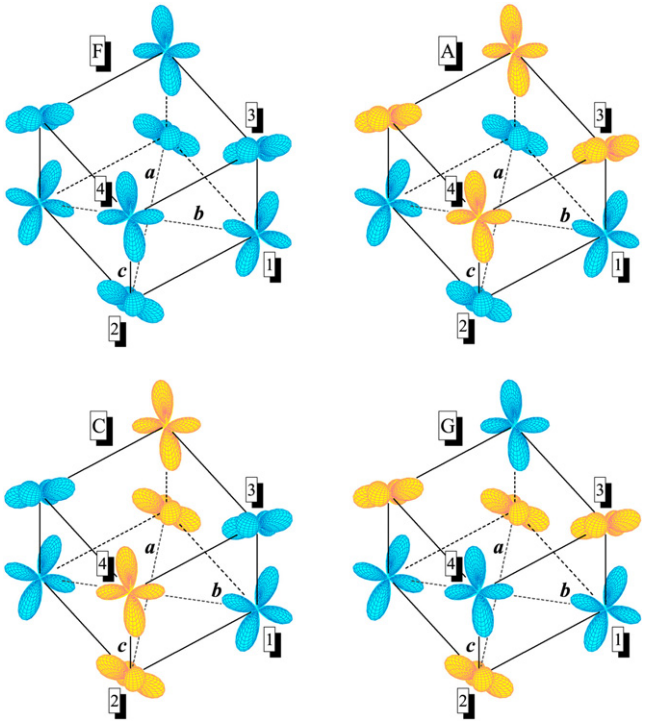

Figure 20. Distribution of the electron density around titanium sites as obtained in the Hartree–Fock calculations for the ferromagnetic (F) and A-, C-, and G-type antiferromagnetic alignment in $YTiO_3$ [5]. Different magnetic sublattices are shown by different colors.

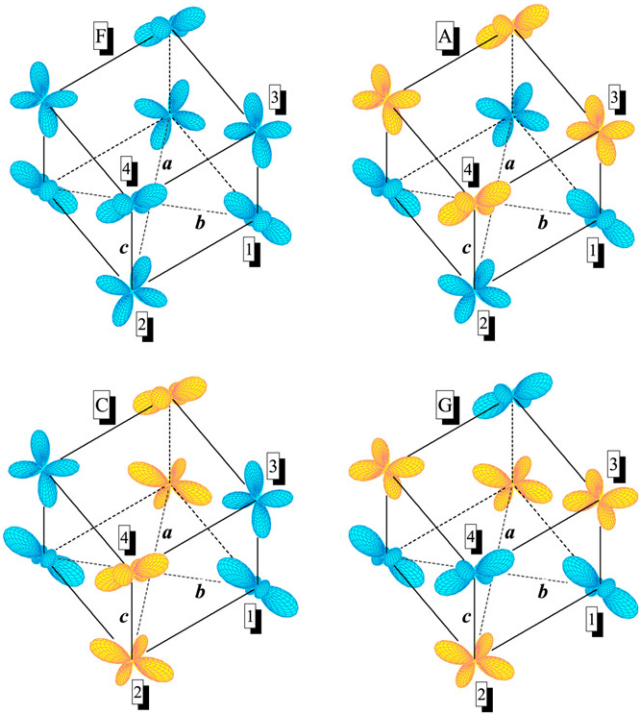

Figure 21. Distribution of the electron density around titanium sites as obtained in the Hartree–Fock calculations for the ferromagnetic (F) and A-, C-, and G-type antiferromagnetic alignment in the orthorhombic phase of $LaTiO_3$ [5]. Different magnetic sublattices are shown by different colors.

second-order perturbation theory (table 7). The absolute values of correlation energy are larger than in YVO_3 (figure 17), but still substantially smaller than the crystal-field splitting. Apparently, this is one of the reasons why the Hartree–Fock theory is still applicable.

The situation with $YTiO_3$ is similar to the orthorhombic YVO_3. The orbital degrees of freedom are frozen in some particular configuration by the crystal-field splitting. This orbital configuration practically independent of the magnetic state (figure 20). The type of the orbital ordering is compatible with the ferromagnetic ground state, which can be reproduced at the Hartree–Fock level. The same conclusion has been drawn in all-electron LDA + U calculations [103, 105]. The correlation effects tend to destabilize the ferromagnetic ground state (table 7 and figure 17). Although the ferromagnetic state has the lowest energy even after taking into account the correlation effects, the energy separation from the next A-type antiferromagnetic state is very fragile[35]. However, this seems to be consistent with the relatively low Curie temperature ($T_C \approx 30$ K [87]) observed in $YTiO_3$ [5].

$LaTiO_3$ is clearly an exception. The orbital degrees of freedom are rather flexible and not completely quenched by the crystal distortion (figure 21). The mean-field Hartree–Fock theory yields an incorrect magnetic ground state (antiferromagnetic A-type, instead of the G-type, table 7). The correlation interactions treated as a perturbation to the Hartree–Fock solution do not change the overall picture, and the G-type antiferromagnetic state remain unstable relative to the A-state[36].

Thus, the origin of the G-type antiferromagnetic ground state in $LaTiO_3$ remains a challenging problem for future theories. Apparently, one of the basic assumptions about the nondegeneracy of the Hartree–Fock ground state breaks down in the case of $LaTiO_3$, and the true magnetic ground state cannot be continuously approached through a series of corrections applied to the Hartree–Fock ground state. One intuitive reason can already be seen in figure 17: the correlation energies, derived as perturbations to the Hartree–Fock solutions, are exceptionally large in the case of $LaTiO_3$, so that some of them become comparable with the crystal-field splitting (figure 14). This means that there is a certain inconsistency in our theoretical treatment: the perturbation becomes comparable with the basic energy splitting, that was used in order to justify this perturbation theory expansion.

In summary, the crystal-field theory can indeed explain many properties of the distorted perovskite oxides, but apparently not all. Particularly, the decrease of the crystal distortion in the case of lanthanides leaves some room for the orbital fluctuations. $LaTiO_3$ is definitely the most difficult case,

[35] More precisely, the on-site correlations tends to destabilize the ferromagnetic ground state, as it is clearly seen from figure 17. Small inter-site correlations partially compensate this trend, again in the favor of the ferromagnetic alignment [61].

[36] Effects of the higher-order perturbation theory expansion have been considered in [61], in the framework of the T-matrix theory. Despite some quantitative differences from the second-order perturbation theory, the main conclusion was the same and the G-type antiferromagnetic state was always higher in energy than the A-type antiferromagnetic state.

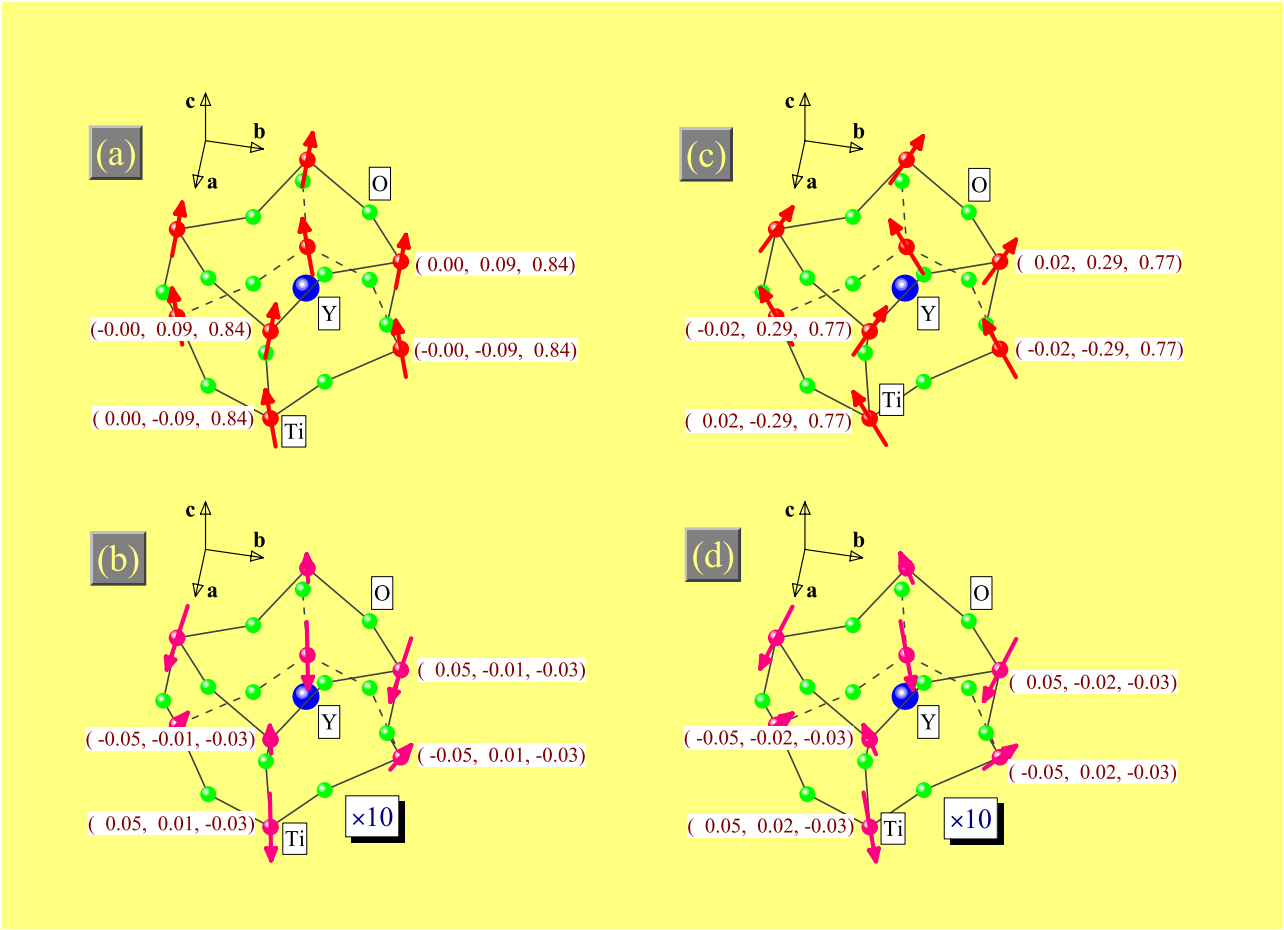

Figure 22. Spin ((a) and (c)) and orbital ((b) and (d)) magnetic structures of $YTiO_3$ in the Hartree–Fock approximation ((a) and (b)) and after taking into account the correlation effects in the frameworks of variational superexchange theory ((c) and (d)). The directions of the magnetic moments at different titanium sites are shown by arrows. The size of each arrow is proportional to the size of the magnetic moment. For the clarity, the arrows for the orbital magnetic moments have been additionally scaled by the factor ten. Corresponding values of spin and orbital magnetic moments, measured in Bohr magnetons, are given in parentheses.

where the crystal-field theory, if supplemented with realistic values of the model parameters, fails to reproduce the correct magnetic ground state.

The main conclusions of this section are based on the second-order perturbation theory for the correlation interactions, which may be questionable because the values of the Coulomb repulsion $\mathcal{U}$ (table 6) are not particularly small and it is reasonable to expect that higher-order effects may modify some of these conclusions. The role of higher-orders of the perturbation theory expansion for the correlation energy was investigated in [61], in the framework of the T-matrix theory. Generally, the higher-order effects tend to reduce the correlation energy. However, the amount of this reduction strongly depends on the magnetic state. For example, the correlation energy in the ferromagnetic state is overestimated in the second-order perturbation theory by less than 15% in comparison with the T-matrix method. For the antiferromagnetic configurations, the effect is more pronounced and the correlation energy can be overestimated by about 50%. Nevertheless, the main trends in the behavior of the correlation energy are already well captured by the second-order perturbation theory. For example, if the absolute value of the correlation energy was the largest for a certain magnetic configuration in the second-order perturbation theory, the same tendency is clearly seen in the T-matrix theory, etc. In this sense we believe that the main conclusions of the present section are valid. Nevertheless, the correlation interactions in the distorted perovskite oxides is certainly one of the most important and interesting problems, which deserves a thorough investigation. The analysis based on the second-order perturbation theory, considered in this section, can be regarded as only the first step in this direction.

6.3.5. Effects of spin–orbit interaction. The spin–orbit interaction in distorted perovskite structures generally leads to a noncollinear magnetic alignment, which obeys certain symmetry rules [106–109]. The spin magnetic moments aligned along one of the orthorhombic axes are subjected to certain rotational forces originating from anisotropic and Dzyaloshinsky–Moriya interactions [80, 81], which lead to the reorientation (or canting) of these magnetic moments. Hence, in the equilibrium magnetic structure we will generally have all three projections of the magnetic moments onto the orthorhombic axes. Furthermore, the type of the magnetic

ordering for these three projections will be generally different. Thus, each magnetic structure can be generally abbreviated as X–Y–Z, where X, Y, and Z is the type of the magnetic ordering (F, A, C, or G) formed by the projections of the spin magnetic moments onto the orthorhombic axes **a**, **b**, and **c**, respectively. The orbital magnetic structure has the same symmetry, although it may have a different origin for the canting, which arises mainly from the minimization of the single-ion anisotropy energy at each transition-metal site. Generally, the spin and orbital magnetic moments are not collinear to each other [109, 110].

For example, the true magnetic ground state of $YTiO_3$ is G–A–F (figure 22), where in addition to the main ferromagnetic components along the **c** axis, there will be two antiferromagnetic components parallel to the **a** and **b** axes. In this case, one can expect rather interesting consequences of the correlation effects on the noncollinear magnetic alignment [5]. As was pointed out in section 6.3.4, without spin–orbit interaction, the correlation effects in $YTiO_3$ favor the antiferromagnetic inter-atomic coupling and systematically lower the energies of all antiferromagnetic structures relative to the ferromagnetic one. Then, it is reasonable to expect that after taking into consideration the spin–orbit interaction, the correlation effects will systematically increase the weight of the antiferromagnetic components in the ground-state configuration and result in an additional spin canting away from the collinear ferromagnetic state. Such an effect is clearly seen in figure 22: after taking into account the correlation effects in the framework of variational superexchange theory, about 8% of the spin magnetization density is transferred from the ferromagnetic part parallel to the **c** axis to the antiferromagnetic part lying in the **ab** plane. The distribution of the orbital magnetization density is less sensitive to the correlation effects. We also note that the correlation effects readily explain the experimental values reported for the F and G components of the magnetic moments [88].

Another interesting phenomenon, which is directly related to the spin–orbit interaction, is the temperature-induced magnetization reversal behavior observed in YVO_3 (figure 23) [90]. Briefly, upon cooling, the magnetization parallel to the **a** axis (in the notation of the *Pbnm* group) changes sign two times: first continuously, in the monoclinic regions, and then discontinuously, at the point of the monoclinic-to-orthorhombic transition. Although the discontinuity of the magnetization is certainly expected for the first-order monoclinic-to-orthorhombic transition, its behavior in the monoclinic phase is somewhat surprising. Nevertheless, it is important to note that a similar effect is known to occur in some ferrimagnetic materials, such as Co_2VO_4, consisting of two or more types of antiferromagnetically ordered magnetic ions [111]. Although there are several additional complications in comparison with Co_2VO_4, this may be a clue to understanding the unusual behavior of YVO_3 [5].

(i) As was pointed out in section 6.3.4, although all vanadium atoms are *chemically* equivalent, in the monoclinic phase they are located in *different crystallographic environments* and one can clearly distinguish two types of vanadium atoms lying in the planes (1, 2) and (3, 4) (figure 18). The magnetic interactions in these two planes are also different: while J_{34} is strongly antiferromagnetic, similar to the orthorhombic phase, J_{12} is considerably weaker (table 8)[37]. Thus, there is a clear analogy with two magnetic sublattices of Co and V existing in Co_2VO_4. However, in the monoclinic phase of YVO_3, this difference is entirely related with the local crystal distortions, which create two inequivalent types of vanadium sites.

(ii) An additional complication comes from the fact that YVO_3 is an antiferromagnet, and no net magnetic moment is expected for the either C- or G-type antiferromagnetic

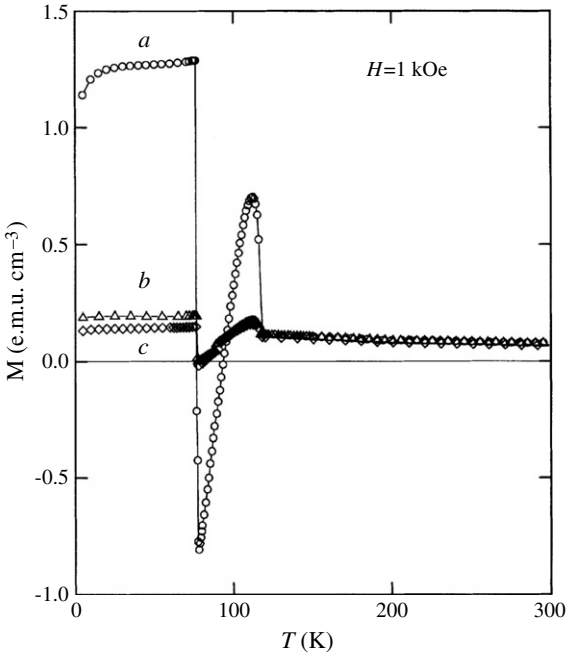

Figure 23. Temperature dependence of the magnetization in YVO_3 (from [90]). The magnetic field of 1 kOe is applied along the **a**, **b**, and **c** axes, respectively. In the monoclinic phase, realized between 116 and 77 K, the magnetization after first increasing starts decreasing and crosses zero at around 95 K to a large negative value. With further cooling, it jumps to a large positive value at the point of monoclinic-to-orthorhombic transition. The orientation of the **a**, **b**, and **c** axes corresponds to the *Pbnm* group, both in orthorhombic and monoclinic phases.

Table 8. Inter-atomic magnetic interactions (in meV) in the orthorhombic and monoclinic phases of YVO_3, as obtained in the Hartree–Fock calculations without spin–orbit interaction [5]. The orthorhombic phase is stabilized below 77 K, while the monoclinic phase is stabilized above 77 K. The atomic positions are explained in figure 14. The magnetic interactions were computed using formula (29) for infinitesimal magnetic rotations near the antiferromagnetic ground state of the G-type in the case of the orthorhombic phase and the C-type in the case of the monoclinic phase.

Phase	J_{12}	J_{13}	J_{24}	J_{34}
Orthorhombic	−4.4	−4.8	−4.8	−4.4
Monoclinic	−0.9	2.2	2.2	−4.5

[37] Note that the existence of two magnetic sublattices also leads to a splitting of the magnon spectrum into acoustic and optical branches [5, 104], which was clearly seen in the experiment [92].

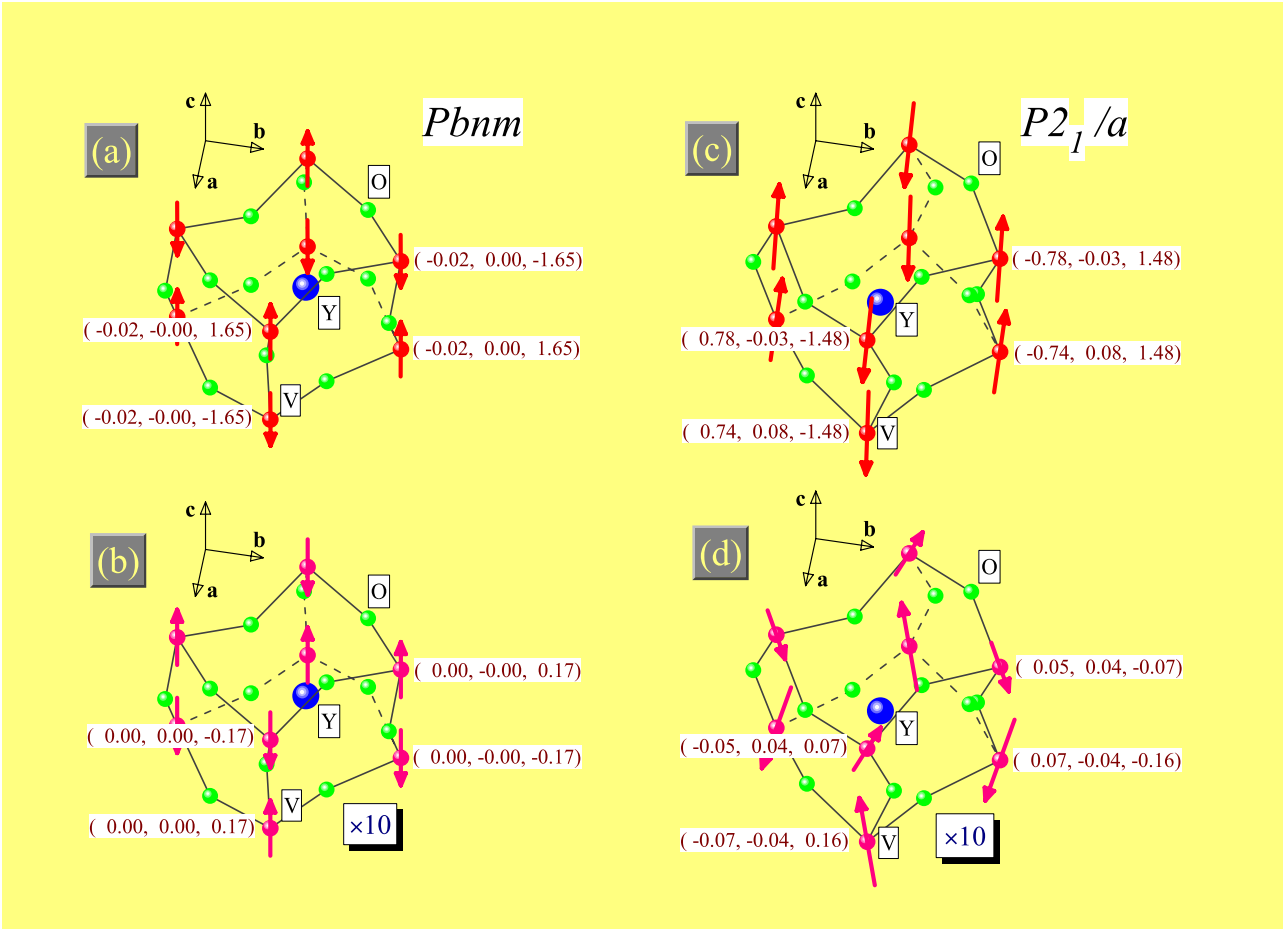

Figure 24. Spin ((a) and (c)) and orbital ((b) and (d)) magnetic structures realized in the orthorhombic ((a) and (b)) and monoclinic ((c) and (d)) phases of YVO_3 in the Hartree–Fock approximation. The directions of the magnetic moments at different vanadium sites are shown by arrows. The size of each arrow is proportional to the size of the magnetic moment. For clarity, the arrows for the orbital magnetic moments have been additionally scaled by a factor ten. Corresponding values of spin and orbital magnetic moments, which are measured in Bohr magnetons, are given in parentheses. The orientation of the **a**, **b**, and **c** axes corresponds to the *Pbnm* group in the orthorhombic phase and the $P2_1/a$ group in the monoclinic phases. The $P2_1/a$ notation can be transformed to the *Pbnm* notation by interchanging the axes **a** and **b** [91].

ordering, realized in the monoclinic and orthorhombic phases, respectively. Nevertheless, it is reasonable to expect a weak ferromagnetism arising from the spin–orbit interaction in the distorted perovskite structure. In the orthorhombic phase, the weak ferromagnetic moment is indeed aligned along the **a** axis (in the notations of the *Pbmn* group), which follows directly from the symmetry considerations (figure 24). In the monoclinic phase, the situation is more complicated because there is a large cancelation for all three projections of the magnetic moments. However, since the planes (1, 2) and (3, 4) are inequivalent, this cancelation is not complete and a net magnetic moment can be expected along the **b** direction in the notation of the $P2_1/a$ group, which corresponds to the **a** direction in the notation of the *Pbmn* group.

Thus, there is at least a qualitative consistency with the experimental data [90]. A quantitative theory of the magnetization reversal behavior in YVO_3 is still missing, and would be an interesting step to do.

6.4. Hyperoxide KO_2

As a final example, we would like to consider a molecular analog of a 'strongly correlated' system without any transition-metal or rare-earth elements.

The simplest molecule, whose ground state is different from the conventional spin singlet is O_2.[38] If these molecules form a crystal (by either cooling or pressurizing), it may become magnetic. Such a situation is indeed realized in solid oxygen [112, 113]. Since O_2 is a good oxidizer and can easily take an additional electron when it brought in contact with alkali elements, there is another way of making crystalline arrays of oxygen molecules, in the form of ionic crystals. Such materials do exist. One typical example is KO_2, which is used as the chemical oxygen generator in rebreathers, spacecrafts, and life support systems. The magnetic properties of KO_2 and other alkali hyperoxides were intensively studied in 1970s [114–119]. However, many details

[38] The O_2 molecule has two unpaired electrons in the doubly-degenerate π_g level, resulting in the spin-triplet ground state, as is required by the first Hund rule.

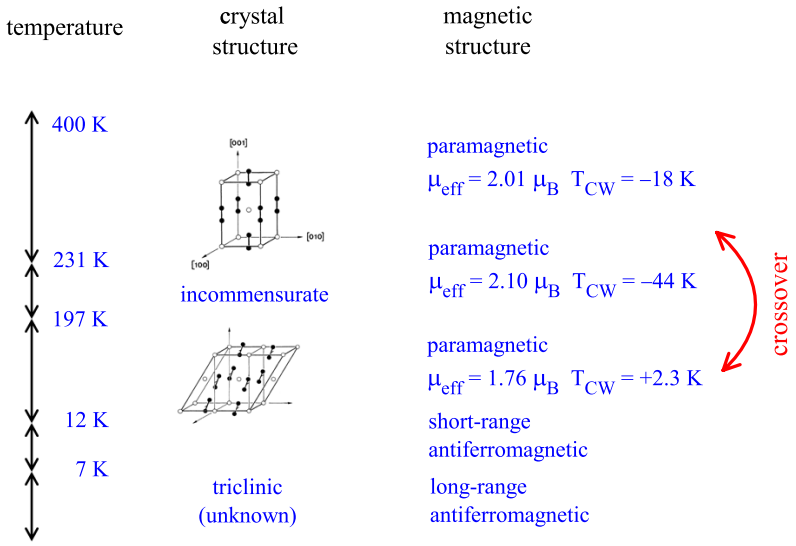

Figure 25. Brief summary of structural and magnetic properties of KO_2 [115, 116]. The oxygen molecules are shown as black dimers and potassium atoms are indicated by white symbols. $\mu_{\rm eff}$ is the effective magnetic moment and $T_{\rm CW}$ is the Curie–Weiss temperature. Both are derived from the analysis of magnetic susceptibility data in different temperature regimes. The arrow shows the region of 'ferromagnetic–antiferromagnetic crossover', where the Curie–Weiss temperature changes sign.

of their behavior remain largely unknown, even today[39]. KO_2 has six crystallographic modifications, apparently related to different orientations of the oxygen molecules (figure 25). However, the details are known only for the body-centered tetragonal (bct) phase stabilized between 231 and 400 K. Below 7 K, KO_2 develops a long-range antiferromagnetic order [115, 120]. However, its type is unknown. In the paramagnetic region, the Curie–Weiss temperature ($T_{\rm CW}$) changes sign at around 230 K, indicating some change of interatomic magnetic interactions. Formally, this change may be related with one of the structural phase transitions. However, no profound change of the magnetic susceptibility has been observed around this transition, indicating that there might be a more fundamental reason for the change of $T_{\rm CW}$. Finally, the effective magnetic moment in the paramagnetic region ($\mu_{\rm eff}$) is about 2 $\mu_{\rm B}$, meaning that the large orbital contribution (about 1 $\mu_{\rm B}$) is not quenched by the crystal distortion and persists down to 12 K. This suggests that the actual crystal distortion related to the reorientation of the oxygen molecules near the bct phase is quite weak, and the bct phase itself can be regarded as a good starting point for the analysis of the magnetic properties of KO_2 in the wide paramagnetic region [121].

The oxygen molecule appears to be the building block of not only the crystal, but also of the electronic structure of KO_2 in the local-density approximation. The strong hybridization within the molecule leads to the formation of the molecular levels. The interaction between the molecules is considerably weaker, so that the molecular orbitals form a group of narrow nonoverlapping bands (figure 26). Thus, there is a clear analogy with the atomic limit in the physics of strongly correlated systems [10, 82], except that now, the localized electrons (or holes) reside on the *molecular orbitals*, which are

[39] Evidently, the early progress was severely hampered by many objective difficulties related with the preparation of rigidly held samples and the separation of intrinsic properties of KO_2 from inhomogeneity effects.

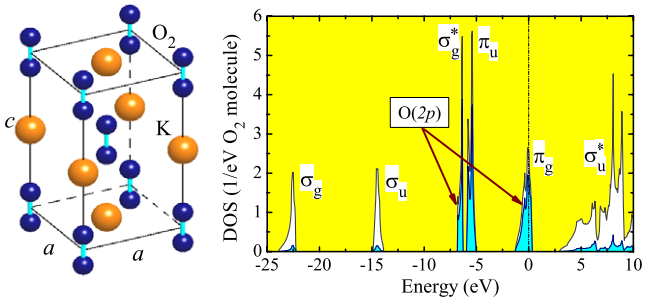

Figure 26. Crystal structure and LDA density of states of the bct phase of KO_2. The shaded area shows the contributions of the oxygen 2p states. Other symbols show the positions of the main bands. Fermi level is at zero energy.

distributed between two atomic sites. The doubly-degenerate $\pi_{\rm g}$ band located near the Fermi level is formed by antibonding molecular p_x and p_y orbitals. In comparison with the solid oxygen, the potassium atom donates an extra electron into the $\pi_{\rm g}$ band. Therefore, the band is $\frac{3}{4}$ filled. Due to the peculiar $\frac{3}{4}$ filling, not only spin but also orbital degrees of freedom appear to be active and contribute to spin and lattice dynamics of KO_2. In this sense, KO_2 can be regarded as a molecular analog of correlated electron systems, comprising of orbitally degenerate magnetic O_2^- ions [121].

6.4.1. Construction and parameters of model Hamiltonian. Obviously, the minimal model for KO_2 should be constructed in the basis of $\pi_{\rm g}$ bands and take into account the Coulomb correlations beyond conventional LDA. The basic idea of the construction of such a model is to relate each lattice point to the single oxygen molecule and formulate the problem in the Wannier basis corresponding to antibonding molecular p_x and p_y orbitals.

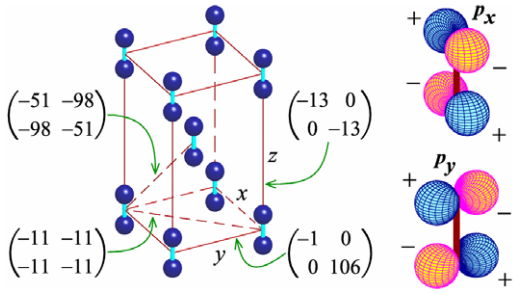

Figure 27. Transfer integrals (in meV) associated with different bonds in the bct phase of KO_2 [121]. The antibonding molecular orbitals are shown in the right part of the figure. The order of orbitals is p_x and p_y.

The transfer integrals operating between such *molecular Wannier orbitals* can be derived by using the formal downfolding procedure described in section 3.3. The behavior of these transfer integrals in the bct lattice is explained in figure 27. Basically, all interactions are restricted by four nearest neighbors. Other interactions are considerably smaller. The on-site part of the one-electron Hamiltonian $\|h^{\alpha\beta}_{\mathbf{RR}'}\|$ incorporates the relativistic spin–orbit interaction,

$$\hat{h}_{\mathbf{RR}} = \frac{\xi}{2}\begin{pmatrix} 0 & -\mathrm{i} & 0 & 0 \\ \mathrm{i} & 0 & 0 & 0 \\ 0 & 0 & 0 & i \\ 0 & 0 & -\mathrm{i} & 0 \end{pmatrix},$$

in the basis of $|p_x\uparrow\rangle$, $|p_y\uparrow\rangle$, $|p_x\downarrow\rangle$, and $|p_y\downarrow\rangle$ orbitals, where the arrows indicate the spin state. The parameter of spin–orbit interaction ξ is about 17 meV [121].

The screened Coulomb interactions in the π_g band are computed in two steps [22]. First, the interaction parameters between *atomic* 2p orbitals are derived by using the constrained DFT method. It yields the intra-atomic Coulomb interaction $u \approx 11.4$ eV, the inter-atomic intramolecular Coulomb interaction $v \approx 1.3$ eV, and the intra-atomic exchange interaction $j \approx 2.3$ eV.[40] After that, it is necessary to consider the additional screening of these interactions in the π_g band by other bands[41], and derive the full matrix $\hat{U} = \|U_{\alpha\beta\gamma\delta}\|$ of screened Coulomb interactions between *antibonding molecular orbitals* p_x and p_y, which is fully specified by the parameters of intraorbital Coulomb interaction $\mathcal{U} \approx 3.6$ eV and the exchange interaction $\mathcal{J} \approx 0.6$ eV. This part can be done in the random-phase approximation, by starting from the interaction parameters obtained in the constrained DFT. It is also important to remember that the interorbital Coulomb interaction $\mathcal{U}'$ is related to $\mathcal{U}$ and $\mathcal{J}$ by the identity $\mathcal{U}' = \mathcal{U} - 2\mathcal{J}$.

[40] For comparison, the parameters of bare interactions are $u \approx 27.8$, $v \approx 11.0$, and $j \approx 2.9$ eV. Thus, similar to the cubic perovskites considered in section 6.1.2 the inter-atomic Coulomb interactions v appears to be the most screened, while the intra-atomic exchange interaction j is the least screened.

[41] Namely, the π_u band, that is a bonding combination of the p_x and p_y orbitals, as well as the σ_g^* and σ_u^* bands, constructed from the p_z orbitals (figure 26).

6.4.2. Implications on the properties of KO_2. Since the Coulomb interactions $\mathcal{U}$ and $\mathcal{U}'$ are clearly the largest parameters in the problem, the Hubbard model (3) can be further converted into a spin–orbital superexchange model by starting from the limit of isolated oxygen molecules and treating all transfer integrals as a perturbation [10]. Due to the $\frac{3}{4}$ filling, it is convenient to use the hole representation and ascribe to each molecular site a single hole spin–orbital

$$|\alpha\rangle = a b_\uparrow |p_x\uparrow\rangle + a\tilde{b}_\uparrow |p_y\uparrow\rangle + \tilde{a} b_\downarrow |p_x\downarrow\rangle + \tilde{a}\tilde{b}_\downarrow |p_y\downarrow\rangle, \quad (34)$$

where $|a|^2+|\tilde{a}|^2 = |b_\uparrow|^2+|\tilde{b}_\uparrow|^2 = |b_\downarrow|^2+|\tilde{b}_\downarrow|^2 = 1$. Then, the energy gain $\mathcal{T}_{\mathbf{RR}'} \equiv \mathcal{T}(\alpha_{\mathbf{R}}, \alpha_{\mathbf{R}'})$ caused by the virtual hoppings in the bond $\langle\mathbf{RR}'\rangle$ can be computed using the formula (33). In this case, $G \equiv G(\alpha_{\mathbf{R}}, \alpha_{\mathbf{R}'})$ is the Slater determinant constructed from the hole orbitals at the molecular centers $\mathbf{R}$ and $\mathbf{R}'$, $E_{\mathbf{R}'M}$ and $|\mathbf{R}'M\rangle$ are the eigenvalues and eigenstates of the excited two-hole configurations at the molecular center $\mathbf{R}'$, and $\hat{\mathscr{P}}_{\mathbf{R}'}$ is a projector operator enforcing the Pauli principle and preventing any hoppings of holes into $\alpha_{\mathbf{R}'}$.

The problem can be further simplified by eliminating the orbital degrees of freedom, described by the b-variable in (34), and constructing an effective spin model separately for each temperature regime. This can be generally done by averaging (33) with some distribution function $\mathcal{D}(b_\uparrow, \tilde{b}_\uparrow, b_\downarrow, \tilde{b}_\downarrow, T)$ [10]. The formulation is especially simple for two limiting cases: $T \to 0$, corresponding to an orbitally ordered state, and $T \to \infty$, corresponding to complete orbital disorder.

In the *low-temperature* limit $k_B T \ll \xi$ (note that $\xi/k_B \approx 200$ K), $\mathcal{D}(b_\uparrow, \tilde{b}_\uparrow, b_\downarrow, \tilde{b}_\downarrow, T)$ is fully controlled by the relativistic spin–orbit interaction, which picks up a linear combination of two spin–orbitals, $|p_+\uparrow\rangle = -(|p_x\uparrow\rangle - \mathrm{i}|p_y\uparrow\rangle)/\sqrt{2}$ and $|p_-\uparrow\rangle = (|p_x\uparrow\rangle + \mathrm{i}|p_y\uparrow\rangle)/\sqrt{2}$, minimizing the spin–orbit interaction energy. Since each hole-orbital α is confined in the two-dimensional subspace spanned by $|p_+\uparrow\rangle$ and $|p_-\uparrow\rangle$, the energies (33) can be further mapped onto the anisotropic Heisenberg model with pseudospin 1/2 [121]:

$$\hat{H}_{\mathrm{Heis}} = -\tfrac{1}{2}\sum_{\mathbf{RR}'}\left\{\left(\hat{\tau}^x_{\mathbf{R}}\hat{\tau}^x_{\mathbf{R}'} + \hat{\tau}^y_{\mathbf{R}}\hat{\tau}^y_{\mathbf{R}'}\right) J^{\perp}_{\mathbf{RR}'} + \hat{\tau}^z_{\mathbf{R}}\hat{\tau}^z_{\mathbf{R}'} J^{\parallel}_{\mathbf{RR}'}\right\}, \quad (35)$$

where

$$\hat{\tau}_x = \begin{pmatrix} 0 & 1 \\ 1 & 0 \end{pmatrix}, \qquad \hat{\tau}_y = \begin{pmatrix} 0 & -\mathrm{i} \\ \mathrm{i} & 0 \end{pmatrix},$$

and

$$\hat{\tau}_z = \begin{pmatrix} 1 & 0 \\ 0 & -1 \end{pmatrix}$$

are the Pauli matrices in the basis of $|p_+\uparrow\rangle$ and $|p_-\downarrow\rangle$ orbitals. The parameters of superexchange interactions, $J^{\perp}_{\mathbf{RR}'}$ and $J^{\parallel}_{\mathbf{RR}'}$ can be expressed through the pair-interaction energies $\mathcal{T}_{\mathbf{RR}'} \equiv \mathcal{T}(\alpha_{\mathbf{R}}, \alpha_{\mathbf{R}'})$ by considering different combinations of $\alpha_{\mathbf{R}}$ and $\alpha_{\mathbf{R}'}$.[42] They are summarized in table 9. The second-neighbor

[42] Namely, by denoting as $|\tau^{\pm}_x\rangle = (|p_+\uparrow\rangle \pm |p_-\downarrow\rangle)/\sqrt{2}$, $|\tau^{\pm}_y\rangle = (|p_+\uparrow\rangle \pm \mathrm{i}|p_-\downarrow\rangle)/\sqrt{2}$, $|\tau^{+}_z\rangle = |p_+\uparrow\rangle$, and $|\tau^{-}_z\rangle = |p_-\downarrow\rangle$ the pseudospin states corresponding to the positive (+) and negative (−) directions parallel to the x-, y-, and z-axes, the parameters of superexchange interactions can be found as $2J^{\perp}_{\mathbf{RR}'} = \mathcal{T}(\tau^+_{\mathbf{R}x}, \tau^-_{\mathbf{R}'x}) - \mathcal{T}(\tau^+_{\mathbf{R}x}, \tau^+_{\mathbf{R}'x}) = \mathcal{T}(\tau^+_{\mathbf{R}y}, \tau^-_{\mathbf{R}'y}) - \mathcal{T}(\tau^+_{\mathbf{R}y}, \tau^+_{\mathbf{R}'y})$, and $2J^{\parallel}_{\mathbf{RR}'} = \mathcal{T}(\tau^+_{\mathbf{R}z}, \tau^-_{\mathbf{R}'z}) - \mathcal{T}(\tau^+_{\mathbf{R}z}, \tau^+_{\mathbf{R}'z})$.

Table 9. Parameters of Heisenberg model (in meV) for the bct phase of KO_2 in different temperature regimes [121]. $J^{\parallel}_{\mathbf{RR}'}$ and $J^{\perp}_{\mathbf{RR}'}$ correspond to the low-temperature limit, while $\bar{J}_{\mathbf{RR}'}$ corresponds to the high-temperature limit. The vectors separating two oxygen molecules, $\mathbf{b} = \mathbf{R}' - \mathbf{R}$, are denoted as $\mathbf{b}_1 = (0, a, 0)$, $\mathbf{b}_2 = (\frac{a}{2}, \frac{a}{2}, \frac{c}{2})$, $\mathbf{b}_3 = (a, a, 0)$, and $\mathbf{b}_4 = (0, 0, c)$ (see figure 26 for the notation).

Vector	$J^{\parallel}_{\mathbf{RR}'}$	$J^{\perp}_{\mathbf{RR}'}$	$\bar{J}_{\mathbf{RR}'}$
$\mathbf{b}_1$	−0.43	−1.15	−0.47
$\mathbf{b}_2$	1.31	−1.09	−1.01
$\mathbf{b}_3$	−0.02	−0.05	−0.02
$\mathbf{b}_4$	−0.07	−0.07	−0.01

coupling $J^{\parallel}_{\mathbf{R}\mathbf{R}+\mathbf{b}_2}$ stabilizes the easy-axis ferromagnetic state. Other interactions are antiferromagnetic and frustrated on the bct lattice. Then, the Curie temperature can be estimated using the renormalized spin-wave theory [122]. It yields $T_C \sim 70$ K, which does not seem to be fully consistent with the experimental data, because no long-range magnetic order has been observed down to a very low temperature [114, 115]. However, there is also a number of factors, which may further affect this theoretical picture [121]. One is the deformation of the relativistic spin–orbitals $|p_+\uparrow\rangle$ and $|p_-\downarrow\rangle$ caused by superexchange interactions. Another one is the reorientation of the oxygen molecules (which probably takes place but this is not precisely known from early experimental studies [115, 116]). For example, one can suggest that above 12 K, the reorientation of the oxygen molecules is not particularly large and leads only to some quantitative redefinition of parameters of the anisotropic Heisenberg model (35), which systematically decreases T_C [121]. However, it seems that below 12 K the situation changes dramatically. Apparently, the transition to the new crystallographic phase is accompanied by a large reorientation of the oxygen molecules, which not only quenches the orbital magnetic moment, but also plays a decisive role in the formation of the long-range antiferromagnetic order [121]. A complete quantitative theory describing these reorientation effects is missing at the present stage but would certainly be an interesting step to develop in the future.

Nevertheless, the mystery of KO_2 is that there is another region of antiferromagnetic interactions, which is realized in the high-temperature bct phase, as is clearly manifested in the behavior of the inverse magnetic susceptibility [114, 115]. The origin of this 'high-temperature antiferromagnetism' may be directly related to the orbital disorder. Indeed, in the *high-temperature limit* $k_BT \gg \xi$, the thermal fluctuations will eventually destroy the relativistic coupling between spin and orbital degrees of freedom. Therefore, it is reasonable to assume that all orbital configurations are realized with equal probability. In this case, the spin system becomes fully isotropic, and the parameters of the spin Hamiltonian, $2\bar{J}_{\mathbf{RR}'} = \bar{\mathcal{T}}^{\uparrow\downarrow}_{\mathbf{RR}'} - \bar{\mathcal{T}}^{\uparrow\uparrow}_{\mathbf{RR}'}$, can be derived by averaging the energies (33) for antiferromagnetic ($\uparrow\downarrow$) and ferromagnetic ($\uparrow\uparrow$) configurations of spins in each bond over all combinations of orbital variables [10, 121]. The orbital disorder gives rise to antiferromagnetic interactions $\bar{J}_{\mathbf{RR}'}$, which are also summarized in table 9. The corresponding Curie–Weiss temperature can be estimated using renormalized spin-wave theory. It yields $T_{CW} \sim -80$ K, which is comparable with the experimental data [114, 115].

In summary, the magnetic properties of KO_2 provide an example of spin–orbital superexchange physics realized in the molecular solid. The properties largely depend on the orbital state of the O_2^- ions. In the paramagnetic region, the character of intermolecular interactions gradually changes from mainly ferromagnetic, driven by the relativistic spin–orbit interaction, to antiferromagnetic, corresponding to the picture of an independent spin and orbital disorder. All these features seem to be consistent with the experimental behavior of KO_2. Finally, it is important to note that the geometry of molecular orbitals can be used as an additional degree of freedom, which controls the properties of superexchange interactions. Definitely, it adds many new functionalities into the classical problem of superexchange, which deserve further exploration.

7. Summary and concluding remarks

The goal of this review article was to outline the main ideas and scope of a newly developing direction for strongly correlated systems which can be called 'realistic modeling'. The primary purpose of this project is to make a bridge between methods of first-principles electronic structure calculations, based on the density-functional theory, and many-body models, describing properties of strongly correlated systems in terms of a limited number of the most relevant model parameters and including information about all remaining electronic structure implicitly, through the renormalization of these model parameters.

Realistic modeling has all the potential to become a useful tool of electronic structure calculations for strongly correlated systems. It is true that we still have to rely on a number of approximations, particularly in the process of calculation of screened Coulomb interactions, which are inevitable in any approach. However, it is very important that, apart from these approximations, the entire procedure is parameter-free. Namely, we no longer have to deal with adjustable parameters and we do not need to resolve numerous ambiguities with the choice of these parameters. Instead, realistic modeling brings the state of the discussion to a qualitatively new level: how to improve the approximations used for the definition and calculation of these model parameters.

One undeniable advantage of realistic modeling is that it allows us to combine the accuracy and predictable power of first-principles electronic structure calculations with the flexibility and insights of the model analysis. This idea was illustrated on a series of examples, for which we were able to consider the whole chain of actions starting from conventional electronic structure calculations in the local-density approximation, followed by the construction of an appropriate low-energy model, motivated by these calculations, and finally—by the solution of this model and by the analysis of properties of strongly correlated systems in terms of these model categories and trends. The first applications are indeed very encouraging and we would like

to hope that in the future the ideas of realistic modeling will continue to develop in order to become a powerful tool for theoretical analysis, design, and control of the properties of strongly correlated materials.

Acknowledgments

This work is partly supported by Grant-in-Aid for Scientific Research in Priority Area 'Anomalous Quantum Materials' and Grant-in-Aid for Scientific Research (C) No. 20540337 from the Ministry of Education, Culture, Sport, Science and Technology of Japan.

Appendix A. Properties of Coulomb interactions in the atomic limit

In the atomic limit, the $5 \times 5 \times 5 \times 5$ matrix $\hat{u}$ of interactions between d electrons is totally specified by three radial Slater's integrals F^0, F^2, and F^4, which are related to the parameters u and j, obtained in the constrained DFT, by the identities

$$u = F^0 \tag{A.1}$$

and

$$j = \tfrac{1}{14}\left(F^2 + F^4\right). \tag{A.2}$$

In order to derive all three Slater's integrals knowing only two parameters u and j, extracted from the constrained DFT, one can use the additional relation

$$F^4/F^2 \simeq 0.63, \tag{A.3}$$

which holds approximately in the atomic limit.

We would like to emphasize that the parameter j, defined as (A.2), is the measure of the exchange splitting corresponding to the spherically averaged electron densities for the majority- and minority-spin states. In the literature one can find other definitions of the exchange integrals, which sometimes cause certain confusion. For example, Mizokawa and Fujimori [76] defined the exchange integral as

$$j_{\mathrm{MF}} = \tfrac{5}{2}B + C, \tag{A.4}$$

in terms of the two Racah parameters: $B = (9F^2 - 5F^4)/441$ and $C = 5F^4/63$. Then, it is easy to verify the validity of the following relation between j and j_{MF}:

$$j_{\mathrm{MF}} = \tfrac{5}{7}j \approx 0.71\,j. \tag{A.5}$$

Thus, j_{MF} *is always smaller than* j.

Alternatively, one can define parameters of Coulomb interactions only for the t_{2g} manifold. There are three types of interactions, which are sometimes called as the Kanamori parameters [60]:

$$u_t = \int \mathrm{d}\mathbf{r} \int \mathrm{d}\mathbf{r}'\, \tilde{W}^{\dagger}_{xy}(\mathbf{r})\tilde{W}_{xy}(\mathbf{r})|\mathbf{r}-\mathbf{r}'|^{-1}\tilde{W}^{\dagger}_{xy}(\mathbf{r}')\tilde{W}_{xy}(\mathbf{r}'), \tag{A.6}$$

$$u'_t = \int \mathrm{d}\mathbf{r} \int \mathrm{d}\mathbf{r}'\, \tilde{W}^{\dagger}_{xy}(\mathbf{r})\tilde{W}_{xy}(\mathbf{r})|\mathbf{r}-\mathbf{r}'|^{-1}\tilde{W}^{\dagger}_{yz}(\mathbf{r}')\tilde{W}_{yz}(\mathbf{r}'), \tag{A.7}$$

and

$$j_t = \int \mathrm{d}\mathbf{r} \int \mathrm{d}\mathbf{r}'\, \tilde{W}^{\dagger}_{xy}(\mathbf{r})\tilde{W}_{yz}(\mathbf{r})|\mathbf{r}-\mathbf{r}'|^{-1}\tilde{W}^{\dagger}_{xy}(\mathbf{r}')\tilde{W}_{yz}(\mathbf{r}'). \tag{A.8}$$

In the atomic limit, they can be expressed in terms of radial Slater's integrals as

$$u_t = F^0 + \tfrac{4}{49}F^2 + \tfrac{4}{49}F^4, \tag{A.9}$$

$$u'_t = F^0 - \tfrac{2}{49}F^2 - \tfrac{4}{441}F^4, \tag{A.10}$$

and

$$j_t = \tfrac{3}{49}F^2 + \tfrac{20}{441}F^4. \tag{A.11}$$

Other types of interactions between t_{2g} electrons vanish. In fact, there are only two independent interactions because u_t, u'_t, and j_t are related by the identity:

$$u_t = u'_t + 2j_t. \tag{A.12}$$

It is also straightforward to show that

$$u_t = u + \tfrac{8}{7}j. \tag{A.13}$$

The parameter j_t can be expressed through j using the approximate relation between Slater's integrals (A.3), which yields

$$j_t \approx 0.77\,j. \tag{A.14}$$

Thus, generally we have the following inequality for the exchange integrals defined in three different ways:

$$j_{\mathrm{MF}} < j_t < j. \tag{A.15}$$

After taking into account the RPA screening, the parameters u_t, u'_t, and j_t correspond to the parameters $\mathcal{U}$, $\mathcal{U}'$, and $\mathcal{J}$ considered in sections 6.1.2 and 6.3.3.

For the f-shell, the $7 \times 7 \times 7 \times 7$ matrix $\hat{u}$ can be reconstructed from F^0, F^2, F^4, and F^6, by using the following identities in the atomic limit [71]:

$$u = F^0, \tag{A.16}$$

$$j = \tfrac{1}{3}\left(\tfrac{2}{15}F^2 + \tfrac{1}{11}F^4 + \tfrac{50}{429}F^4\right), \tag{A.17}$$

$F^4/F^2 \simeq 451/675$, and $F^6/F^2 \simeq 1001/2025$.

Appendix B. Correlations between 2p–3d hybridization and screening of Coulomb interactions in the t_{2g} band of transition-metal perovskite oxides

In this appendix we derive some approximate expression for the static RPA screening of Coulomb interactions in the t_{2g} band of transition-metal oxides by the oxygen 2p band.

First, we assume that the band dispersion is considerably smaller than the charge-transfer energy Δ_{CT}, which is the energy difference between the centers of gravity of the oxygen 2p band and the transition-metal t_{2g} and e_g bands (figure 1). Then, for the static ($\omega = 0$) screening caused by the oxygen 2p band, the denominator of the polarization function (24) can be replaced by Δ_{CT} and one can perform a separate summation over the occupied and empty states.

Table B1. Correlation between number of 3d electrons in the oxygen 2p band (N^{o}) and the value of screened Coulomb interaction ($\mathcal{U}$, in eV) in the transition-metal t_{2g} band. The symbols 'c', 'o', and 'm' stand for the cubic, orthorhombic, and monoclinic structure, respectively. The positions of the transition-metal sites are explained in figure 14. Generally, the site '1' is located in a less distorted environment while the site '3' is located in a more distorted environment.

Compound	Phase	Site	N^{o}	$\mathcal{U}$
$YTiO_3$	o	1	0.66	3.45
$LaTiO_3$	o	1	0.73	3.20
$SrVO_3$	c	1	1.19	2.53
YVO_3	o	1	0.74	3.27
YVO_3	m	1	0.76	3.19
		3	0.72	3.26
$LaVO_3$	m	1	0.81	3.11
		3	0.80	3.12

Then, we focus on the self-screening caused by the atomic 3d states, which contributes to the oxygen 2p band due to the hybridization effects and consider the matrix elements of (24) in the basis of atomic 3d orbitals. These matrix elements can be expressed through the density matrices of the 3d states calculated separately in the occupied oxygen 2p band and in the empty part of the spectrum (correspondingly $\hat{n}^{o}$ and $\hat{n}^{e}$). Finally, we assume that $n^{o(e)}_{\alpha\beta} \sim N^{o(e)}\delta_{\alpha\beta}$ (N^{o} and N^{e} being the total number of 3d electrons in the oxygen 2p band and in the empty part of the spectrum, respectively) and consider the diagonal matrix elements of (24), which mainly contribute to the screening of the intraorbital Coulomb interaction $\mathcal{U}$. In this case, one can derive the following (approximate) expression for the diagonal matrix elements of the polarization:

$$\mathcal{P} \sim \frac{N^{o}N^{e}}{\Delta_{CT}}.$$

Moreover, since the total number of 3d electrons is conserved, $N^{o}+N^{e}$ is a constant, which depends only on the number of 3d electrons in the occupied part of the t_{2g} band. Therefore, it is reasonable to expect the following rules for compounds having the same number of t_{2g} electrons:

(i) the larger the weight of the transition-metal 3d states in the oxygen 2p band, N^{o}, the stronger the screening of Coulomb interactions in the t_{2g} band;
(ii) N^{o} is controlled by the hybridization between oxygen 2p and transition-metal 3d states, which in turn depends on the crystal distortion (particularly, the buckling of the Ti–O–Ti and V–O–V bonds). Therefore, stronger distortion will tend to reduce the screening;
(iii) smaller Δ_{CT} in the case of $SrVO_3$ will additionally increase the screening of Coulomb interactions in the t_{2g} band.

All these trends are clearly seen in table A.1, which shows the correlation between N^{o} and $\mathcal{U}$ in different transition-metal perovskite oxides. For example, more distorted YBO_3 compounds are characterized by smaller N^{o} and, therefore, by somewhat larger $\mathcal{U}$ in comparison with the less distorted $LaBO_3$ compounds. The same tendency holds for different transition-metal sites in the monoclinic structure: the sites with a more distorted environment have large $\mathcal{U}$ and vice versa.

References

[1] Hohenberg P and Kohn W 1964 *Phys. Rev.* **136** B864
[2] Kohn W and Sham L J 1965 *Phys. Rev.* **140** A1133
[3] Parr R G and Yang W 1989 *Density-Functional Theory of Atoms and Molecules* (Oxford: Clarendon)
[4] Imada M, Fujimori A and Tokura Y 1998 *Rev. Mod. Phys.* **70** 1039
[5] Solovyev I V 2006 *Phys. Rev.* B **74** 054412
[6] Solovyev I V and Terakura K 1999 *Phys. Rev. Lett.* **82** 2959
[7] Solovyev I V and Terakura K 2003 *Orbital Degeneracy and Magnetism of Perovskite Manganese Oxides* (*Electronic Structure and Magnetism of Complex Materials*) ed D J Singh and D A Papaconstantopoulos (Berlin: Springer) p 253
[8] de Gennes P-G 1960 *Phys. Rev.* **118** 141
[9] Solovyev I V 2003 *Phys. Rev.* B **67** 174406
[10] Kugel K I and Khomskii D I 1982 *Sov. Phys.—Usp.* **25** 231
[11] Anderson P W 1959 *Phys. Rev.* **115** 2
[12] Wannier G H 1937 *Phys. Rev.* **52** 191
[13] Andersen O K 1975 *Phys. Rev.* B **12** 3060
[14] Gunnarsson O, Jepsen O and Andersen O K 1983 *Phys. Rev.* B **27** 7144
[15] Andersen O K and Jepsen O 1984 *Phys. Rev. Lett.* **53** 2571
[16] Marzari N and Vanderbilt D 1997 *Phys. Rev.* B **56** 12847
[17] Ku W, Rosner H, Pickett W E and Scalettar R T 2002 *Phys. Rev. Lett.* **89** 167204
[18] Anisimov V I, Kondakov D E, Kozhevnikov A V, Nekrasov I A, Pchelkina Z V, Allen J W, Mo S-K, Kim H-D, Metcalf P, Suga S, Sekiyama A, Keller G, Leonov I, Ren X and Vollhardt D 2005 *Phys. Rev.* B **71** 125119
[19] Streltsov S V, Mylnikova A S, Shorikov A O, Pchelkina Z V, Khomskii D I and Anisimov V I 2005 *Phys. Rev.* B **71** 245114
[20] Solovyev I V 2004 *Phys. Rev.* B **69** 134403
[21] Imai Y, Solovyev I and Imada M 2005 *Phys. Rev. Lett.* **95** 176405
[22] Solovyev I V 2006 *Phys. Rev.* B **73** 155117
[23] Solovyev I V, Pchelkina Z V and Anisimov V I 2007 *Phys. Rev.* B **75** 045110
[24] Andersen O K and Saha-Dasgupta T 2000 *Phys. Rev.* B **62** R16219
[25] Mochizuki M and Imada M 2003 *Phys. Rev. Lett.* **91** 167203
[26] Kanamori J 1957 *Prog. Theor. Phys.* **17** 177
[27] Herring C 1966 *Magnetism* vol 4, ed G T Rado and H Suhl (New York: Academic)
[28] Mazurenko V V, Skornyakov S L, Kozhevnikov A V, Mila F and Anisimov V I 2007 *Phys. Rev.* B **75** 224408
[29] Dederichs P H, Blügel S, Zeller R and Akai H 1984 *Phys. Rev. Lett.* **53** 2512
[30] Gunnarsson O, Andersen O K, Jepsen O and Zaanen J 1989 *Phys. Rev.* B **39** 1708
[31] Anisimov V I and Gunnarsson O 1991 *Phys. Rev.* B **43** 7570
[32] Solovyev I V and Dederichs P H 1994 *Phys. Rev.* B **49** 6736
[33] Janak J F 1978 *Phys. Rev.* B **18** 7165
[34] Hedin L 1965 *Phys. Rev.* **139** A796
[35] Aryasetiawan F and Gunnarsson O 1998 *Rep. Prog. Phys.* **61** 237
[36] Onida G, Reining L and Rubio A 2002 *Rev. Mod. Phys.* **74** 601
[37] Solovyev I V and Imada M 2005 *Phys. Rev.* B **71** 045103
[38] Runge E and Gross E K U 1984 *Phys. Rev. Lett.* **52** 997
[39] Aryasetiawan F, Imada M, Georges A, Kotliar G, Biermann S and Lichtenstein A I 2004 *Phys. Rev.* B **70** 195104
[40] Hybertsen M S and Louie S G 1987 *Phys. Rev.* B **35** 5585
[41] Solovyev I V 2005 *Phys. Rev. Lett.* **95** 267205
[42] Solovyev I, Hamada N and Terakura K 1996 *Phys. Rev.* B **53** 7158
[43] Georges A, Kotliar G, Krauth W and Rozenberg M J 1996 *Rev. Mod. Phys.* **68** 13

[44] Kotliar G and Vollhardt D 2004 *Phys. Today* **57(3)** 53
[45] Kotliar G, Savrasov S Y, Haule K, Oudovenko V S, Parcollet O and Marianetti C A 2006 *Rev. Mod. Phys.* **78** 865
[46] Held K 2007 *Adv. Phys.* **56** 829
[47] Maier T, Jarrel M, Pruschke T and Hettler M H 2005 *Rev. Mod. Phys.* **77** 1027
[48] Arita R, Held A, Lukoyanov A V and Anisimov V I 2007 *Phys. Rev. Lett.* **98** 166402
[49] Imada M and Kashima T 2000 *J. Phys. Soc. Japan* **69** 2723
[50] Kashima T and Imada M 2001 *J. Phys. Soc. Japan* **70** 2287
[51] Mizusaki T and Imada M 2004 *Phys. Rev.* B **69** 125110
[52] Otsuka Y and Imada M 2006 *J. Phys. Soc. Japan* **75** 124707
[53] Liechtenstein A I, Katsnelson M I, Antropov V P and Gubanov V A 1987 *J. Magn. Magn. Mater.* **67** 65
[54] Solovyev I V 2003 Magnetic interactions in transition-metal oxides *Recent Research Developments in Magnetism and Magnetic Materials* vol 1 (India: Transworld Research Network) p 253
[55] Solovyev I V 2003 *Phys. Rev. Lett.* **91** 177201
[56] Friedel J and Sayers C M 1977 *J. Physique* **38** 697
[57] Kajzar F and Friedel J 1978 *J. Physique* **39** 397
[58] Treglia G, Ducastelle F and Spanjaard D 1980 *J. Physique* **41** 281
[59] Veselov M G and Labzovskiy L N 1986 *Theory of Atom: Structure of Electronic Shells* (Moscow: Nauka)
[60] Kanamori J 1963 *Prog. Theor. Phys.* **30** 275
[61] Solovyev I V 2007 *J. Exp. Theor. Phys.* **105** 46
[62] Oleś A M, Khaliullin G, Horsch P and Feiner L F 2005 *Phys. Rev.* B **72** 214431
[63] Liebsch A 2003 *Phys. Rev. Lett.* **90** 096401
[64] Slater J C and Koster G F 1954 *Phys. Rev.* **94** 1498
[65] Bradley C J and Cracknell A P 1972 *The Mathematical Theoryof Symmetry in Solids* (Oxford: Clarendon)
[66] Lechermann F, Georges A, Poteryaev A, Biermann S, Posternak M, Yamasaki A and Andersen O K 2006 *Phys. Rev.* B **74** 125120
[67] Anisimov V I, Zaanen J and Andersen O K 1991 *Phys. Rev.* B **44** 943
[68] Norman M and Freeman A 1986 *Phys. Rev.* B **33** 8896
[69] McMahan A K, Martin R M and Satpathy S 1988 *Phys. Rev.* B **38** 6650
[70] Gunnarsson O, Postnikov A V and Andersen O K 1989 *Phys. Rev.* B **40** 10407
[71] Solovyev I V, Dederichs P H and Anisimov V I 1994 *Phys. Rev.* B **50** 16861
[72] van der Marel D and Sawatzky G A 1988 *Phys. Rev.* B **37** 10674
[73] Norman M 1995 *Phys. Rev.* B **52** 1421
[74] Brooks M S S 2001 *J. Phys.: Condens. Matter* **13** L469
[75] Zaanen J and Sawatzky G A 1990 *J. Solid State Chem.* **88** 8
[76] Mizokawa T and Fujimori A 1996 *Phys. Rev.* B **54** 5368
[77] Sekiyama A, Fujiwara H, Imada S, Suga S, Eisaki H, Uchida S I, Takegahara K, Harima H, Saitoh Y, Nekrasov I A, Keller G, Kondakov D E, Kozhevnikov A V, Pruschke Th, Held K, Vollhardt D and Anisimov V I 2004 *Phys. Rev. Lett.* **93** 156402
[78] Miyake T and Aryasetiawan F 2008 *Phys. Rev.* B **77** 085122
[79] Kolodiazhnyi T and Wimbush S C 2006 *Phys. Rev. Lett.* **96** 246404
[80] Dzyaloshinsky I 1958 *J. Chem. Phys. Solids* **4** 241
[81] Moriya T 1960 *Phys. Rev.* **120** 91
[82] Tokura Y and Nagaosa N 2000 *Science* **288** 462
[83] Tsvetkov A A, Mena F P, van Loosdrecht P H M, van der Marel D, Ren Y, Nugroho A A, Menovsky A A, Elfimov I S and Sawatzky G A 2004 *Phys. Rev.* B **69** 075110
[84] Cwik M, Lorenz T, Baier J, Müller R, André G, Bourée F, Lichtenberg F, Freimuth A, Schmitz R, Müller-Hartmann E and Braden M 2003 *Phys. Rev.* B **68** 060401(R)
[85] Maclean D A, Ng H-N and Greedan J E 1979 *J. Solid State Chem.* **30** 35
[86] Itoh M, Tsuchiya M, Tanaka H and Motoya K 1999 *J. Phys. Soc. Japan* **68** 2783
[87] Akimitsu J, Ichikawa H, Eguchi N, Miyano T, Nishi M and Kakurai K 2001 *J. Phys. Soc. Japan* **70** 3475
[88] Ulrich C, Khaliullin G, Okamoto S, Reehuis M, Ivanov A, He H, Taguchi Y, Tokura Y and Keimer B 2002 *Phys. Rev. Lett.* **89** 167202
[89] Keimer B, Casa D, Ivanov A, Lynn J W, Zimmermann M v, Hill J P, Gibbs D, Taguchi Y and Tokura Y 2000 *Phys. Rev. Lett.* **85** 3946
[90] Ren Y, Palstra T T M, Khomskii D I, Pellegrin E, Nugroho A A, Menovsky A A and Sawatzky G A 1998 *Nature* **396** 441
[91] Blake G R, Palstra T T, Ren Y, Nugroho A A and Menovsky A A 2002 *Phys. Rev.* B **65** 174112
[92] Ulrich C, Khaliullin G, Sirker J, Reehuis M, Ohl M, Miyasaka S, Tokura Y and Keimer B 2003 *Phys. Rev. Lett.* **91** 257202
[93] Zubkov V G, Bazuev G V, Perelyaev V A and Shveikin G P 1973 *Sov. Phys.—Solid State* **15** 1079
[94] Bordet P, Chaillout C, Marezio M, Huang Q, Santoro A, Cheong S-W, Takagi H, Oglesby C S and Batlogg B 1993 *J. Solid State Chem.* **106** 253
[95] Khaliullin G and Maekawa S 2000 *Phys. Rev. Lett.* **85** 3950
[96] Khaliullin G 2005 *Prog. Theor. Phys. Suppl.* **160** 155
[97] Mochizuki M and Imada M 2004 *New J. Phys.* **6** 154
[98] Schmitz R, Entin-Wohlman O, Aharony A, Harris A B and Müller-Hartmann E 2005 *Phys. Rev.* B **71** 144412
[99] Pavarini E, Yamasaki A, Nuss J and Andersen O K 2005 *New J. Phys.* **7** 188
[100] Pavarini E, Biermann S, Poteryaev A, Lichtenstein A I, Georges A and Andersen O K 2004 *Phys. Rev. Lett.* **92** 176403
[101] De Raychaudhury M, Pavarini E and Andersen O K 2007 *Phys. Rev. Lett.* **99** 126402
[102] Mizokawa T, Khomskii D I and Sawatzky G A 1999 *Phys. Rev.* B **60** 7309
[103] Sawada H and Terakura K 1998 *Phys. Rev.* B **58** 6831
[104] Fang Z and Nagaosa N 2004 *Phys. Rev. Lett.* **93** 176404
[105] Okatov S, Poteryaev A and Lichtenstein A 2005 *Europhys. Lett.* **70** 499
[106] Treves D 1962 *Phys. Rev.* **125** 1843
[107] Moskvin A S and Sinitsyn E V 1973 *Sov. Phys.—Solid State* **14** 2198
[108] Yamaguchi T 1974 *J. Chem. Phys. Solids* **35** 479
[109] Solovyev I, Hamada N and Terakura K 1996 *Phys. Rev. Lett.* **76** 4825
[110] Solovyev I V 1997 *Phys. Rev.* B **55** 8060
[111] Menyuk N, Dwight K and Wickham D G 1960 *Phys. Rev. Lett.* **4** 119
[112] Serra S, Chiarotti G, Scandolo S and Tosatti E 1998 *Phys. Rev. Lett.* **80** 5160
[113] Goncharenko I N, Makarova O L and Ulivi L 2004 *Phys. Rev. Lett.* **93** 055502
[114] Ziegler M, Rosenfeld M, Känzig W and Fischer P 1976 *Helv. Phys. Acta* **49** 57
[115] Känzig W and Labhart M 1976 *J. Physique Coll.* **37** C7 39
[116] Labhart M, Raoux D, Känzig W and Bösch M A 1979 *Phys. Rev.* B **20** 53
[117] Bösch M A, Lines M E and Labhart M 1980 *Phys. Rev. Lett.* **45** 140
[118] Lines M E 1981 *Phys. Rev.* B **24** 5248
[119] Zumsteg A, Ziegler M, Känzig W and Bösch M 1974 *Phys. Condens. Matter* **17** 267
[120] Smith H G, Nicklow R M, Raubenheimer L J and Wilkinson M K 1966 *J. Appl. Phys.* **37** 1047
[121] Solovyev I V 2008 *New J. Phys.* **10** 013035
[122] Tyablikov S V 1975 *Methods of Quantum Theory of Magnetism* (Moscow: Nauka)